

UNIVERSITY OF OKLAHOMA
GRADUATE COLLEGE

QUASI-OMNIDIRECTIONAL BROADBAND ANTI-REFLECTIVE
SURFACE OF MULTI-LEVEL SUB-WAVELENGTH STRUCTURES

A THESIS
SUBMITTED TO THE GRADUATE FACULTY
in partial fulfillment of the requirements for the
Degree of
MASTER OF SCIENCE

By
BARRY PAUL BOYDSTUN JR
Norman, Oklahoma
2020

QUASI-OMNIDIRECTIONAL BROADBAND ANTI-REFLECTIVE
SURFACE OF MULTI-LEVEL SUB-WAVELENGTH STRUCTURES

A THESIS APPROVED FOR THE
SCHOOL OF ELECTRICAL AND COMPUTER ENGINEERING

BY THE COMMITTEE CONSISTING OF

Dr. Hjalti Sigmarsson

Dr. Jay McDaniel

Dr. Berhanu Bulcha

*This thesis is dedicated to my family and to the people who helped me along my
journey leading me to this future that I had foreseen for myself
which has now become my present.*

Acknowledgments

First, I would like to sincerely thank my research adviser and chair, Dr. Hjalti H. Sigmarsson, for his guidance and support throughout the duration of my studies. I would not be here at this very moment in my life if Dr. Sigmarsson had not noticed the potential he saw in me. A small amount of time had passed when I became his research assistant and I quickly realized the passion he had for his career. His door was always open for me and others as well. I would also like to thank Dr. Shahrokh Saeedi for taking me under his wing and spending endless amounts of hours in the Radar Innovation Laboratory (RIL) at the Advanced Radar Research Center (ARRC). The wealth of knowledge that he bestowed upon me allowed me to fabricate Dr. Jay McDaniel's several complex multi-layer components for a multitude of projects in the ARRC. Dr. McDaniel also helped me in my academic studies and projects giving me advice anytime I was struggling. His manner of explaining complex theoretical concepts allows the subject to be understood easily.

I learned a plethora of information from Dr. Berhanu Bulcha at the Goddard Space Flight Center (GSFC) working for National Aeronautics and Space Administration (NASA) over my summer internship, which is where the conception for my thesis began. I am very grateful for him taking time out of his busy schedule to be a mentor to me. He allowed me to work on the delay lines of their micro-spectrometer and by the end of the summer I was

able to design a system without dispersion. This in turn helped me broaden my approach to the understanding of radio frequency (RF) concepts. I am extremely grateful for Manuel Quijada, who measured the filter at Goddard, and the fabrication of the filter by Dr. Shingho Ono with his student Xi Yu, at the Nagoya Institute of Technology.

My experience at OU was greatly improved by the friends I made while weathering through my academic studies. The late nights in the labs, working on projects together, and the long hours studying for exams. We have all become good friends and I hope overtime we still remain in contact with each other. I would like to extend my gratitude to all of my colleagues and friends that still remain at the ARRC. I hope your future careers are everything you are seeking for and more.

I would like to thank my father, Barry Boydston, and my brothers for their support over the years while I was pursuing an education. I am extremely grateful to my extended family, each of them were able to help me and my family in their own ways: my uncles and aunts, Frank and Betty Boydston; Julian and Lana Horner; Byron and Deborah Boydston; and Craig and Ladell Cochran. I would like to thank Julian and Nancy Legrand for allowing me to stay in their homes for extended periods of time. I would also like to thank my cousins for driving me to campus when I didn't have a car for many years; Rachel and Franklyn Boydston; Cheryl Cochran; and Victoria Horner. I would like to give a special thanks to Frank and Betty Boydston for teaching me to critically think in my early years as an undergraduate. I did not have this skill until my aunt Betty laid the foundation by teaching me the lower levels of math and my uncle Frankie teaching me physics. He is the one that encouraged me into electrical engineering. I feel very fortunate to have such a family

surrounding me and guiding me in life.

Table of Contents

Acknowledgments	vii
Abstract	xxiv
1 Introduction	1
1.1 Motivation	1
1.2 Outline of the Thesis	3
1.3 Background, Concepts, and Related Research	4
1.3.1 Explanation of Filters	5
1.3.2 Basic Concepts of Optics	6
1.3.3 Anti-Reflective Coatings from Past to Present	7
1.4 Research Objective	11
2 Anti-Reflective Surfaces Filtering Fundamentals	12
2.1 ARCs Using SWSs Filtering Fundamentals	12
2.1.1 Polarization Sensitivity of SWS's	13
2.1.2 Omni-Directionality of SWS's	16
2.2 ARCs Using Thin Films Filtering Fundamentals	22
2.3 Design Concerns for AR Surfaces using SWSs	38
2.3.1 Multi-Level and Inverse SWSs	39
2.3.2 Double-Sided AR Surfaces and Layout Design	40

2.3.3	Completely Omni-Directional Designs	42
2.3.4	Hybrid ARCs	48
2.4	Conclusion	52
3	Theory and Design Fundamentals for SWSs	53
3.1	Design Equations For Tapered Structures	55
3.2	Design Equations For Non-Tapered Structures	61
3.3	Conclusion	66
4	Bandpass Filters Using SWS Surfaces	67
4.1	Tapered SWSs for a Bandpass Filter	69
4.2	Measured Results for Tapered SWSs	75
4.3	Simulation Concerns for THz Filters	78
4.4	Non-Tapered SWSs for a Bandpass Filter	79
4.5	Conclusion	88
5	Fabricating SWS Surfaces by Femtosecond Laser	89
6	Measurement of SWS Surfaces	95
7	Conclusions and Future Work	100
7.1	Future Work	101
	References	102

List of Tables

4.1	AR Surface of Tapered SWS Filter Design Parameters for Quartz	71
4.2	AR Surface of Tapered SWS Filter Design Parameters for Silicon	73
4.3	AR Surface of Non-Tapered SWS Filter Design Parameters for Quartz	82
4.4	AR Surface of Non-Tapered SWS Filter Design Parameters for Silicon	85
6.1	Definitions for Compartments in the Spectrometer	96
6.2	Definitions for Components in the Spectrometer's Optical Path	98

List of Figures

1.1	(Left) How light interacts with a typical transparent surface. (Right) Example of an AR surface of SWSs etched onto the surface of the substrate which captures light at normal incidence through multiple internal reflections.	2
1.2	Various ARCs above the substrate and corresponding RI profiles. Homogeneous ARCs: (a) single-layer, (b) patterned and (c) multi-layer; and inhomogeneous ARCs: (d) single-layer, (e) patterned and (f) complex (from [4]).	9
1.3	(a) Notice the improved pellucidity on the left from an ARC. (b) (1) is normal glass and (2) are porous anti-reflective sections. (c) ARCs reducing the glare on both eyeglasses and automobile lenses (from [4]).	10
2.1	(a) Reflection occurs when light interacts with a macro-structure; (b) Rayleigh effect happens when the structures have comparable dimensions giving a GRIN surface; (c) In actuality, light experiences multiple internal reflections (from [4]).	13

2.2	(Left) SEM (Scanning Electron Microscope) image of periodic tapered structures with a depth = 90 and pitch = 51 μm which are one dimensional and fabricated by femtosecond laser processing. (Right) TE and TM polarizations are represented by the theoretical and measured power reflectance for structures with a depth = 50 and pitch = 25 μm . A Si exterior with no grating structures has a reflection coefficient of 0.3 which is what the reflectance is normalized by (from [5]).	14
2.3	(a) Example of a 2D MES (from [11]). (b) 2D sub-wavelength gratings with depth $d = 30$ and period $\Lambda = 15 \mu\text{m}$ with calculated reflectance at normal incidence for TM and TE polarizations with $n = 1.5$ (from [12]).	14
2.4	A log scale is provided to emphasize the variation of the reflectance characteristics of polarized light interacting with a parabolic SWS's surface which have a depth of $d = 550$ and pitch of $\Lambda = 100 \text{ nm}$ covering the lambda-theta space which ranges from 350 to 1200 nm and angles of incidence ranging from 0° to 90° . Surface reflectance for (a) TM polarized light and (b) TE polarized light (from [34]).	15
2.5	Nano-structured glass having dimensions of 100 nm with varying forms that are a function of wavelength with the calculated reflectance at normal incidence (from [29]).	16

2.6	(a) MgF ₂ ARC, a conventional thin film; profiles with dimensions of depth $d = 550$ and pitch $\Lambda = 100$ nm for defined structures of SWG AR surfaces of (b) conical, and (c) parabolic. Contour plots of the transmittance ratio between various AR methods and bare cover glass under the illumination of oblique angles of incidence and unpolarized radiation (from [34]).	17
2.7	How transmittance is affected by the dimensions of the cylindrical pillar. The pillar on top of the surface has a varying Height = 0 to 800 nm, fixed period $\Lambda = 200$ nm, and diameter $D = 40$ nm for (a) angles of incidence and (b) radiation in wavelengths at normal incidence. The structure layer is evaluated by varying the filling fraction which is done by the Diameter = 0 to 160 nm in (c) and (d) (from [38]).	18
2.8	The reflectance is calculated at (a) normal incidence and (b) a wavelength of 250 nm for different incidence angles. The height is varied for the moth-eye glass nano-structure with a period = 100 nm (from [29]).	19
2.9	The reflectance is calculated at (a) normal incidence and (b) a wavelength of 250 nm for different incidence angles. The period is varied for the moth-eye glass nano-structure with a height = 100 nm (from [29]).	20
2.10	Contour plot displaying the reflectance being a function of wavelength and height for hexagonal arrays which have a period of 300 nm for (a) nano-rod, (b) truncated cone, and (c) perfect cone (from [43]).	20

2.11	The inset is an illustrative graphic showing how the simulations were performed as a function of the top diameter (W). Simulated spectra of transmittance evaluating the impact of tapering a pillar type structure at incident wavelength $\lambda = 500$ nm, angle of incidence $\theta = 85^\circ$, periodicity $P = 200$ nm, diameter $D = 70$ nm, and height $H = 380$ nm under 45° polarization (from [26]).	21
2.12	Light refracting and reflecting off a GaAs substrate used for solar cells (from [42]).	23
2.13	Various incident angles with the amount of light reflecting off a GaAs flat-plane substrate (from [42]).	24
2.14	Different SWG shaped structures displaying the rectangular (left), trapezoidal (middle), and triangular (right). The shading color displays the effective refractive index corresponding to various nano-grating forms relating to the thin film ARCs (from [42]).	24
2.15	(a) A single layer film on a substrate depicting how rays of light propagate through the ARC and a (b) multi-layer film (from [4]).	25
2.16	Reflectance averaged with $[\bar{R} = 1/2 \cdot (R_s + R_p)]$ as a function of AOIs and wavelength for glass without a film and glass coated with the anti-reflection gradient-type film (from [30]).	26
2.17	Light's refractive angular variation using a GRIN ARC (from [35]).	28

2.18	(a)–(c) A 3–1 interface for a standard AR coating with 3 layers; (d)–(f) A 3–1 interface for an AR coating with 200 layers; (g)–(i) A 1.48–1 interface for an AR coating with 47 layers; (j)–(l) 3–1.48 interface for a single layer AR coating. AR coatings with varying interfaces, (Column 1) the substrate’s optical thickness and refractive index profile; (Column 2) Unpolarized light’s averaged reflectance with angular variation; (Column 3) Average reflectance with a spectral variation of 30°, 50°, 60°, 70°, 80°, and 85° (from [31]).	29
2.19	(a)–(c) A 3–1.48 interface for an AR coating with 6 layers; (d)–(f) A 3–1 interface for an AR coating with 53 layers; (g)–(i) A 3–1 interface for an AR coating with 7 layers; (j)–(l) 3–1 interface for a single layer AR coating. AR coatings with varying interfaces, (Column 1) the substrate’s optical thickness and refractive index profile; (Column 2) Unpolarized light’s averaged reflectance with angular variation; (Column 3) Average reflectance with a spectral variation of 30°, 50°, 60°, 70°, 80°, and 85° (from [31]).	31
2.20	The physical thickness of the gradient index (Quintic and Gaussian) coating is 1 μm . The angular reflectance is calculated for a wavelength selected at 1 μm (from [35]).	32
2.21	The varying reflectance, at an incident angle of 89°, is a function of the genuine and modified Quintic total thickness profiles which are normalized (divided) by the wavelength (from [32]).	33

2.22	(a) Profiles of the refractive index and (b) the spectral reflectance is averaged with the incidence angles from 0–80° and 89°. The performance is compared to a modified quintic profile that is an inhomogeneous AR coating devised for the interface between mediums with indices of refraction of 1 and 3; The other AR coating contains a portion of the identical quintic profile having a substrate with a 1.5 index of refraction (from [32]).	34
2.23	(a) Discretized Gaussian profile with five layers between AlN (RI = 2.06) and air. (b) Gaussian profiles with differing numbers of discrete layers with respect to angular reflectance (from [35]).	35
2.24	Different ARCs with their reflectance being a function of incidence angle and wavelength. (i) The single layer (SLAR) is CeO, $n = 1.953$, $d = 78$ nm. (ii) The double-layer (DLAR) is MgF ₂ , ZnS, $n_1 = 1.38$, $n_2 = 2.3$, $d_1 = 107$ nm, $d_2 = 56$ nm. (iii) + (iv) The moth-eye AR surface of SWS's have a diameter of 200 nm and a height of 250 and 500 nm respectively (from [39]). . . .	36
2.25	Conceptual illustrations of the reflection of light on (a) a smooth surface and (b) moth-eye structures; (c) SEM image of anti-reflection artificial structures that have the contour of a parabola; (d) A mere GaAs substrate and a GaAs substrate with an AR parabola surface results for measured reflectance; (e) The picture of the mere 4" silicon wafer (left) and a silicon substrate having the moth-eye structures (right) (from [37]).	38
2.26	(a) A depiction of an AR structure with three layers approximating the effective index of refraction for each layer a (b) multi-layer thin film structure would have (from [21]).	39

2.27	Devised to be anti-reflective inside the Ka-band (32–38 GHz), the Rexolite block is machined on both the top and bottom sides with inverse moth-eye shapes producing an AR surface (from [14]).	40
2.28	(Left) Hot-embossing and imprinting with needles produced the anti-reflection structure shown in the SEM image. (Right) The smooth high resistant silicon (HR-Si), hot-embossed samples of single-layer polystyrene (PS), double-sided PS, and calculated single PS layer with their transmittance spectra (from [15]).	41
2.29	Depicted are the configurations for a hexagonally aligned array (a) and for a rectangular aligned array (b). (c) The rectangular and hexagonal arrays are both AR surfaces under irradiation at normal incidence for the simulated results graphing the reflectance in dB while being a function of frequency. The substrate media has a dielectric constant of $\epsilon_r = 2.56$ for the AR inverse moth-eye models (from [14]).	42
2.30	The sub-wavelength gratings of protuberances composed on the corneal surface of several insects are thought to yield anti-reflective characteristics with a broad bandwidth across the optical spectrum (from [14]).	43
2.31	SEM images of (Left) a moth’s eye, a night-active insect. (Middle) With modest magnification, the compound’s eye hexagonal structure becomes plainly visible. (Right) With enhanced magnification, the corrugated surface of periodic sub-wavelength structures comes into view (from [19]).	43

2.32	The implanted graphics and photos, a scale bar of 1 cm, display the example of a compound eye absorber with the optical arrangement employed for absorbance measurements, respectively. The compound eye absorber is under differing incidence angles for the absorption spectra considering the incident light orientations from (a) the overhead and (b) the underneath (from [16]). . .	44
2.33	The simulated results of the Poynting vector in addition to the electric field intensity from TE polarization for the normal direction at positive and negative orientations, respectively. The white broken lines portray the contour of the Chrome (Cr) layer and the red arrows indicate the route of the Poynting vector (from [16]).	45
2.34	The hexagonal lattice structure's dielectric value is $\epsilon_r = 1.46$ and its simulated transmittance spectra: (a) Contour map of transmittance with $\lambda = 500$ nm, under 45° polarization with $\theta = 85^\circ$, and $H = 350$ nm; (b) Contour map of transmittance with $\lambda = 500$ nm, under 45° polarization with $\theta = 85^\circ$, and $P = 200$ nm; (c) Comparing the spectra of transmittance between a cylindrical pillar structure having $D = 70$ nm and a "moth eye" structure linearly tapered having D tapered from 0 to 70 nm, both under 45° polarization, $H = 350$ nm, and $P = 200$ nm (from [26]).	47

2.35	(a) The ARS has a period and height of 350 nm in the diagram showing the hybrid moth-eye model. (b) Height vs. the effective index of refraction for the entire anti-reflective structure. (Right) Each individual ARC is contrived to couple light into a multi-junction solar cell that has four junctions (4-J), the simulated and measured reflectance is displayed in the figure (from [20]).	49
2.36	A solar cell's hybrid AR coating with multiple sub-wavelength grating layers. (Left) Anti-reflective structure's front view. (Right) Anti-reflective structure's side view (from [41]).	50
2.37	The SiO ₂ anti-reflective coating layer, Silicon grating, and the new hybrid structure's calculated surface reflectivity vs omnidirectionality for (a) <i>TE</i> polarization in addition to (b) <i>TM</i> polarization (from [41]).	50
2.38	The SiO ₂ anti-reflective coating layer, Silicon grating, and the new hybrid structure's calculated surface reflectivity as a function of wavelength for (a) <i>TE</i> polarization in addition to (b) <i>TM</i> polarization (from [41]).	51
2.39	(Left) The four layer ARC's cross-sectional SEM picture, deposited on the substrate made of Si with: $n_4 = 1.11$, $n_3 = 1.32$, $n_2 = 1.79$, $n_1 = 2.38$, and $H_4 = 262$, $H_3 = 118$, $H_2 = 77$, $H_1 = 49$ nm. (Middle) The calculated and measured specular reflectance of the four layer ARC's R_{\perp} was attained by AlInP/GaInP (simplified design) of the inverted metamorphic (IMM) solar cell in addition to the IMM solar cell, respectively. (Right) The AlInP/GaInP design's calculated AOI vs wavelength with TE/TM averaged reflectance (from [18]).	51

3.1	(Left) The reflectance dependence for d/λ . The first minimum the reflectance decreases to is $d/\lambda = 0.4$. The reflectance is virtually zero for $d \gg \lambda$ (from [12]). (Right) SWG parameters (from [13]).	59
3.2	The diagram illustrating the filtering of light and the layout parameters; the cross-sectional perspective of the preferred moth-eye conical structures with parameters.	60
3.3	Graphic of a quartz substrate with a dielectric square lattice structure with simulation configurations including: pitch (Λ), interspace (I), and height (H).	65
4.1	HFSS model of a multi-level micro-cone AR surface having a height $H = 188 \mu\text{m}$ and pitch $\Lambda = 175 \mu\text{m}$ on a quartz substrate having a thickness of $800 \mu\text{m}$	72
4.2	The magnitude ² reflectance of the scattering parameters S_{11} for the quartz multi-level micro-cone AR surface at perpendicular incidence.	73
4.3	(Left) SEM image of the fabricated filter. (Right) HFSS model of the fabricated filter which is a multi-level micro-cone AR surface having a height $H = 188 \mu\text{m}$ and pitch $\Lambda = 175 \mu\text{m}$ on a silicon substrate having a thickness of $800 \mu\text{m}$	74
4.4	The magnitude ² reflectance of the scattering parameters S_{11} for the silicon multi-level micro-cone AR surface at perpendicular incidence.	75
4.5	(Left) Simulated results from HFSS for the bare SI substrate. (Right) Measured results from the bare Si substrate.	76

4.6	(Left) Measured and calculated transmittance of the bare Si substrate. (Right) Smoothing algorithm applied to the data in MATLAB. Z is the surface roughness, d_{air} is the depth of a substrate with the RI of air, dm is the depth of Si substrate, nm is the real RI value, and km is the imaginary RI value.	76
4.7	A graphic demonstrating incoherence. The substrate is not to scale.	77
4.8	Measured results from the multi-level tapered structure surface.	77
4.9	Simulated results from HFSS for the bare SI substrate.	78
4.10	HFSS model of a nano-pillar AR surface having a depth $d = 120.5$ nm, pitch $\Lambda = 48.2$ nm, and period $p = 53.02$ nm on a quartz substrate having a thickness of 800 nm.	83
4.11	The magnitude ² reflectance of the scattering parameters S_{11} for the quartz nano-pillar AR surface at perpendicular incidence. .	84
4.12	HFSS model of a nano-pillar AR surface having a depth $d = 120.5$ nm, pitch $\Lambda = 48.2$ nm, and period $p = 53.02$ nm on a silicon substrate having a thickness of 800 nm.	86
4.13	The magnitude ² reflectance of the scattering parameters S_{11} for the silicon nano-pillar AR surface at perpendicular incidence. .	87
5.1	Two different processing systems. (Top) A steady pace of 5 mm/s is the speed the 2-axis motorized stage is capable of moving. (Bottom) The laser beam from the $f\theta$ lens is concentrated on the plate even if the incident beam is oblique. A scan speed of 2825 mm/s is achieved by revolving the galvanometer mirrors (from [11]).	89

5.2	The one and two dimensional design process with a femtosecond laser, courtesy of NGIT.	90
5.3	(a) Scanned at at 5 mm/s and (b) was scanned at 2825 mm/s. Processed samples comparing differing scanning speeds (from [11]).	91
5.4	(Left) A relation between scanning number and depth as a function of scanning speed set at 2825 mm/s. (Right) A relation between scanning number and scanning speed as a function of Laser power set to 800 mW (from [11]).	92
5.5	(a) Has a pitch = 45 μm and (b) is a pitch = 40 μm . Tapers with different peaks from changing the pitch (from [11]).	92
5.6	(a) The Si and (b) GaAs media showing manufactured 2-dimensional structures (from [11]).	93
6.1	The compartments in the Bruker IFS 125HR (from [52]).	95
6.2	The Spectrometer's optical path (from [52]).	97

Abstract

The demand to remove reflections from surfaces has been a topic of interest for many decades. Accordingly, many methods and techniques have been exploited to achieve the optimum design, which is to impart no reflections at any angle of incidence. As of today, many of these optimized designs still succumb to losses from either polarization sensitivity, incident angles of dependence, narrow-banded, absorbance, and optical phenomena such as diffraction or scattering.

Moth-eye anti-reflection coatings (ARCs) of sub-wavelength structures (SWSs) have been investigated to a great extent to achieve anti-reflection characteristics. This technique is more omnidirectional, broadband, and less sensitive to the polarization of light than the older generation of ARCs using quarter-wave thin films.

This thesis introduces a new procedure for designing a two-dimensional anti-reflective (AR) surface of SWSs by a method, pertaining to a series of formulas, to predetermine the bandwidth of these filters by determining the dimensions of the structure itself or vice versa, the bandwidth of the spectrum selects the profile of the structure. These formulas automatically produce the optimized AR surface concerning the broadest bandwidth and minimum reflection loss. The distinction between tapered and non-tapered SWSs is also discussed, along with each SWS's purpose, including separate methods of

design for either profile. As a result, an AR surface of multi-level SWSs for a bandpass filter is calculated, simulated, fabricated, and measured. These two-dimensional structures in periodic arrays were fabricated by femtosecond laser processing in order to achieve a high aspect ratio and greater mechanical strength. The microstructure has a $175\ \mu\text{m}$ pitch and $188\ \mu\text{m}$ height giving an aspect ratio of 1.07. The design guideline's calculations agree well with the simulated results for tapered and non-tapered structures. The impact of this work is a simpler and quicker method for developing AR surfaces using subwavelength structures.

Chapter 1

Introduction

1.1 Motivation

The incentive for this work is to provide anti-reflective technology that is designed to bring forth optimized results decided by the method of filtering the spectrum. For instance, a bandpass filter with a narrow passband is accomplished with non-tapered sub-wavelength structures and a bandpass filter with a wide passband is achieved with tapered sub-wavelength structures. New guidelines are introduced to design these filters with a system comprised of formulae. Both filters can be designed based on a chosen bandwidth or by selecting the dimensions of the structure itself. Anti-reflective coatings are typically not referred to as filters since the main concern is to keep a surface from being reflective. When the surface is made not only to be anti-reflective for a certain wavelength spectrum, but also to transmit the selected wavelengths, then the coating can be considered as a filter.

Scientists at the National Aeronautics and Space Administration's (NASA's) Goddard Space Flight Center (GSFC) developed the High-Resolution Mid-Infrared Spectrometer (HIRMES)—a 2.5m-diameter telescope that can capture emissions from space. HIRMES is able to gain access to wavelengths that

are challenging to ground-based instruments, such as the infrared (IR) spectrum. NASA's Stratospheric Observatory for Infrared Astronomy (SOFIA) is a Boeing 747SP that is able to fly above $\sim 95\%$ of the water vapor in the Earth's atmosphere giving HIRMES access to this radiation from space enabling our further comprehension of the cosmos [1]. This gives the opportunity for anti-reflection coatings (ARCs) to be employed to increase the amount of information gathered for astronomers to further evaluate our universe. Future space systems will require ever more anti-reflective surfaces to capture a greater spectrum of radiation from space. Anti-reflective (AR) surfaces of sub-wavelength structures (SWSs) enable more of the radiation to be received instead of reflected. Therefore more information can be analyzed instead of being suppressed by the loss of optical components without this technology. Figure 1.1(a) demonstrates how light interacts with a typical surface and figure 1.1(b) shows how an ARC of SWSs interacts with wavelengths of light relative to its dimensions.

NASA needs a window on SOFIA that is highly efficient at capturing and

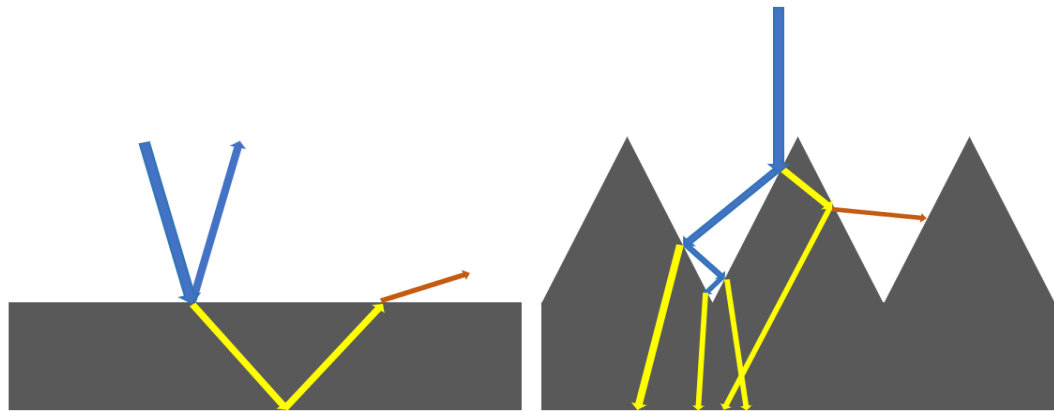


Figure 1.1: (Left) How light interacts with a typical transparent surface. (Right) Example of an AR surface of SWSs etched onto the surface of the substrate which captures light at normal incidence through multiple internal reflections.

transmitting the weak radiation from space. Since SOFIA is an observatory involved with spectroscopy, the window needs to contribute very little loss and operate over a wide bandwidth. The current state of the art literature has difficulty satisfying these conditions. In order to accomplish this, the window will have a SWS surface. This window, with multi-level SWSs, will produce a broadband filter by capturing the radiation from space with multiple internal reflections, which in turn will reduce the loss from reflectivity, which a typical surface has. With the window now capturing incoming wavelengths and guiding these weak signals, wavelengths may now be captured that otherwise would have been lost. In this thesis, a new design process is contrived that enables a more direct path for creating an AR surface that is a low loss broadband filter.

1.2 Outline of the Thesis

The principal focus of this thesis is the contrivance of filtering equations for the design and filtering theory of the anti-reflective technology with sub-wavelength structures. Chapter 1 gives the complete history of the various methods of anti-reflective technology for further understanding and the foundational concepts for complete comprehension. The fundamentals of optics are explained because of the many optical phenomena that occur with anti-reflective surfaces. The full history of the differing methods for obtaining anti-reflective surfaces is provided.

Chapter 2 discusses the filtering fundamentals of anti-reflective technology in order to provide insight into certain considerations and trade-offs. Design concerns are also discussed on the strategy and implementation of the anti-reflective sub-wavelength structures.

Chapter 3 introduces the theory in designing anti-reflective sub-wavelength

structures. The origins of the theory are explained so that the derived equations or guidelines are understood clearly. The process of developing equations for choosing a wavelength spectrum to filter is performed for both tapered and non-tapered structures.

Chapter 4 demonstrates the design and implementation of an anti-reflective sub-wavelength structure to filter a certain wavelength spectrum. The derived filtering equations are utilized for verification for tapered and non-tapered structures. The filters are modeled and simulated in ANSYS High-Frequency Structure Simulator (HFSS).

Chapter 5 covers the fabrication process for developing the multi-level microstructures using a femtosecond laser. The femtosecond laser equipment setup is explained. The advantages of using a femtosecond laser such as profile control mentioned and the disadvantages such as the thermal effect are discussed.

Chapter 6 gives a detailed analysis of the measurement system which is the Bruker IFS 125HR spectrometer. Every compartment within the system is examined and its purpose described. All of the components in the optical path of the Bruker IFS 125Hr are shown. Chapter 7 concludes the thesis with a summary and explores what future considerations should be taken.

1.3 Background, Concepts, and Related Research

The anti-reflective technology is complex enough that brief elucidations on various subjects are needed to provide a firm understanding of this topic. Background on the type of technology that this subject matter falls under, a filter, is given. The fundamentals of optics are described to comprehend how the device operates. The history of the technology is delivered to give

further clarification, since concepts from differing types of devices are constantly referred to.

1.3.1 Explanation of Filters

This technology is about filtering a certain bandwidth of wavelengths from the electromagnetic spectrum of radiation and the concept of what a filter is, first needs to be explained. The electric filter was invented by G. A. Campbell of the American Telephone and Telegraph Company for radio and wire long-distance communication. It consisted of condensers and coils that were joined in such a manner that only allowed alternating currents of selected frequencies to pass and attenuated other currents with undesired frequencies. The most prevalent filters are the low pass, high pass, bandstop, and bandpass filters. The low pass filter allows the lower frequencies and attenuates the higher frequencies after a selected cutoff frequency. The high pass filter passes the higher frequencies above the cutoff and attenuates the lower frequencies. The bandpass filter passes all the frequencies between the upper and lower cutoff frequencies and attenuates the frequencies beyond this bandwidth, lastly, a bandstop filter does the exact opposite of the bandpass filter. The electric filter is used to pass frequencies in a chosen frequency range in the electromagnetic spectrum and inhibit undesired currents from flowing into a circuit [2]. As the years progressed, filters started to have entirely different designs but had nearly the same results. Dr. G. A. Campbell discovered electric wave filters and the field has matured bringing forth many different physical configurations while still performing the filtering process. A theory connecting all these different configurations has not been developed [3]. For electrical engineers, filters either physical or digital became known to remove the undesired frequencies from the

signal and select the frequencies transmitted in the passband.

1.3.2 Basic Concepts of Optics

The fundamentals of optical phenomena should be explained next since this is how the ARC captures desired wavelengths. Reflection is an optical phenomenon that occurs when light is traveling in a medium and comes into contact with another that has a different refractive index. The refractive index (n) is defined by the speed of light in a medium with respect to light in a vacuum and the medium, such as air or glass, is represented optically by the refractive index. The fundamental numerical model of refraction, reflection, and the angle of incidence is described by the Fresnel equation. Reflectance (R) is the measurement of the fraction of incident light reflected at the interface and transmittance (T) measures the rest of the fraction of light that is refracted (transmitted), according to Augustin-Jean Fresnel [4].

Reflection occurs when the propagation direction of light changes within the same medium but refraction is light entering a medium with a different index of refraction and the phase will change if the medium has a higher or lower index of refraction. Interference is the light interacting with itself from reflection or refraction, and depending on their phases, it can be either constructive or destructive. Constructive interference can cause higher orders of diffraction, due to the phases being aligned, increasing the amplitude of the signal and destructive interference can even cancel reflections, from the phases being completely out of phase, reducing the amplitude. Dispersion is the wavelengths of light traveling through the same medium at different speeds.

When light refracts into a medium, and the wavelengths are smaller than the structure, then light can reflect in such a manner causing constructive

interference, this is known as resonance. Diffraction is usually referring to how light behaves (travels) around a structure when the structure's dimensions are equivalent to the wavelength of light, causing the light to interfere with itself. A coherent beam of light travels in a single propagation direction. Scattering is the coherent beam of light splitting into many different propagation paths from interacting with an object.

The polarization of light is referring to the electric and magnetic waves of the beam of radiation, which are perpendicular to each other. Transverse Electric (TE) waves, also known as s-polarization, is when the electric field is normal to the propagation direction while the magnetic field follows the propagation direction. Transverse Magnetic (TM) is the dual of TE , meaning the magnetic field is transverse to the propagation direction and is commonly referred to as p-polarization.

The angle at which light propagates in a certain direction is known as the angle of incidence. When a light source is directly perpendicular to the surface, this is known as normal or perpendicular incidence (0°). When the light source is parallel with the surface, this is an oblique angle of incidence at 90° . The Brewster angle is the angle of incidence in which the TM polarization of light will be completely refracted into a medium. The critical angle is the angle of incidence in which all light is reflected.

1.3.3 Anti-Reflective Coatings from Past to Present

The concept of anti-reflective coatings was fortuitously discovered in the 19th century by John Strutt (Lord Rayleigh) while analyzing the tarnishing on glass and realizing the increased transmittance of light instead of it being diminished. The method of acquiring anti-reflectivity by gradually changing

the refractive index was found by this observation [4]. Structures that have a graded refractive index (GRIN) is a medium where its refractive index (RI) gradually transitions from unity ($n_{air} = 1$) to the substrate (n_s). Naturally transpiring gradient-index lenses that develop in nature include an immense spatial resolution for the eyes of an eagle, antelope have a wide field of vision, and human's minimize aberration [4]. The effectiveness of GRIN structures comes from the fact that the gradual change in density of the medium causes less reflection from the smooth transition of the RI which causes the ray of light to bend progressively (Rayleigh effect). Matching the refractive index at the air-substrate interface is unattainable when acquiring unity. This is technically labeled optical impedance matching, a critical task, when equalizing the index at the interface, and is very challenging to gradually lower the refractive index from the air to the substrate [4]. This technique is most commonly achieved by making the medium porous. This then raises concern for the mechanical strength of the substrate.

Over the years, ARCs using thin films with a quarter-wave thickness became the next method to anti-reflection based on interference. The thickness of the film is determined by the wavelength of interest to be filtered. These filters can also be stacked to form multi-layer quarter-wave ARCs with the layers generally increasing to the substrate's RI. These ARCs are more broadband and the effectiveness is increased with more layers.

The final method of achieving anti-reflection on a surface is the use of ARCs with SWSs. The ARCs with patterned or textured mediums were influenced by a moth's eye. Imitating the best designs from nature has been a global research priority recently and this has brought about a new development in science - a branch called biomimetics [4]. SWSs have dimensions that are smaller than

the wavelength of interest to be filtered. These structures are usually tapered to guide the light into the substrate at incident angles.

As seen in figure 1.2, all ARC's can be grouped into two different classifications: ARC's consisting of homogeneous layers and inhomogeneous layers. Homogeneous layers are layers with a RI that is constant within that layer. Inhomogeneous layers consist of a RI that usually varies toward the substrate. Figure 1.2(a) is an example of a quarter-wave thin film ARC and figure 1.2(c) is an example of a multi-layer thin film ARC. Figure 1.2(b) can be considered a porous thin film or an ARC with SWSs. If the wavelength being filtered is not relative to the SWS's dimensions then it might be considered a porous thin film acting as a homogeneous layer. This film has an effective RI, due to the fact that the film has been partially etched away, allowing more of the light to pass into the substrate, since the film is less dense, which causes light to see an effectively lower index, even though the index of the film remains the same.

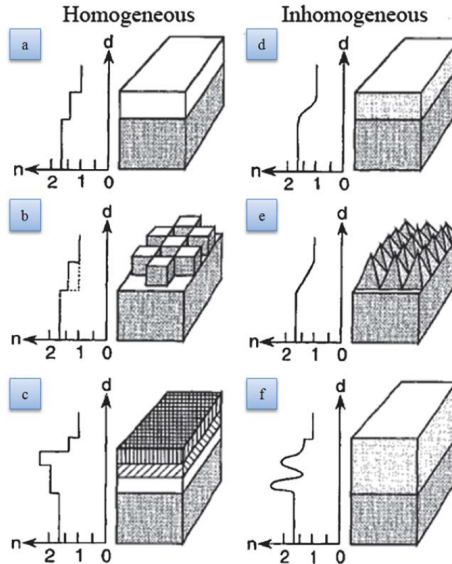


Figure 1.2: Various ARCs above the substrate and corresponding RI profiles. Homogeneous ARCs: (a) single-layer, (b) patterned and (c) multi-layer; and inhomogeneous ARCs: (d) single-layer, (e) patterned and (f) complex (from [4]).

Reflection increases with a greater gap between the RI of one medium to the next. This is why the method shown in figure **1.2(d)** is so effective because the abrupt interface is removed. This can be accomplished by a chemical etching process making the film's porosity gradually lessen to the substrate. This has also been accomplished by using the method of multi-layer ARCs. Figure **1.2(e)** guides the light to the substrate with tapered structures that have sub-wavelength dimensions. Even though the structure's RI is homogeneous, the gradual etching of the structure gives it an effective RI seen by light.

Figure **1.3** depicts the areas and effects that anti-reflective coatings have, which may be implemented in a variety of optical contrivances such as lenses, eye-glasses, military equipment, lasers, mirrors, solar cells, diodes, multipurpose narrow and broad bandpass filters, cathode ray tubes, television screens, sensors for aeronautical applications, cameras, window glasses and anti-glare glasses for automotive applications, a never-ending list [4].

Electrical engineers have benefited from anechoic chambers for decades by being able to test equipment such as antennas and even entire radar systems. Anechoic chambers typically minimize microwave (wavelengths ranging from centimeters to millimeters) reflections using arrays of moth-eye structures (MESs). These chambers allow numerous objects to be submitted under radiation, since the interference from the radiation ricocheting off the walls is

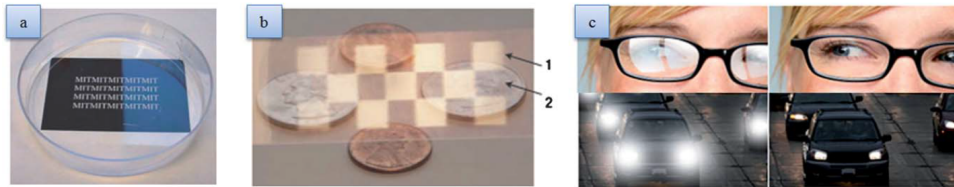


Figure 1.3: (a) Notice the improved pellucidity on the left from an ARC. (b) (1) is normal glass and (2) are porous anti-reflective sections. (c) ARCs reducing the glare on both eyeglasses and automobile lenses (from [4]).

diminished, their radar reflections can be recorded. Silicon (Si) based ARCs have been reported even in space exploration and the aerospace industry which demonstrates the importance and how diverse this technology can be [4].

1.4 Research Objective

In this thesis, a practically omni-directional broadband anti-reflective multi-level sub-wavelength structure is designed. The tapered structures guide the light up to oblique angles of incidence giving its quasi-omnidirectionality. Since the SWS is two-dimensional, it has polarization insensitivity. The spectrum of wavelengths that are anti-reflective depends upon the aspect ratio, which is the height divided by the pitch of the SWS. Since the aspect ratio is approximately 1, this gives a broadband bandpass filter. Several design guidelines are provided to expedite the design process with minimal tuning and dimension scaling. In this thesis, a 0.35 to 0.5 Terahertz (THz) bandpass filter is designed, fabricated, and measured to verify the technology.

Chapter 2

Anti-Reflective Surfaces Filtering Fundamentals

2.1 ARCs Using SWSs Filtering Fundamentals

There are many different methods and techniques for fabricating the MESs, some are more flexible than others. Many of the following techniques were studied to simply gain knowledge on the subject, AR surfaces that were fabricated by femtosecond laser [5]–[11]; milling [12]–[14]; imprinting [15], [16]; deposition [17], [18]; different methods of chemical etching [19]–[30]; theory and simulation [31]–[43]. The femtosecond laser is a simpler fabrication process because it requires fewer manufacturing steps, such as in chemical etching, which requires laying a mask, applying radiation, and the chemical for instance. The femtosecond laser can also reach greater depths faster than some of the chemical methods.

The discovery of moth-eye structures from a nocturnal moth has been studied immensely since 1967 [28]. Figure 2.1 indicates that the dimensions of the SWSs are critical to the selection of wavelengths desired to be filtered. Once the SWS's dimensions become larger than the wavelength of light incident upon it, optical phenomena such as reflection, scattering, diffraction, and resonance occur after being absorbed partially by the structure, an example

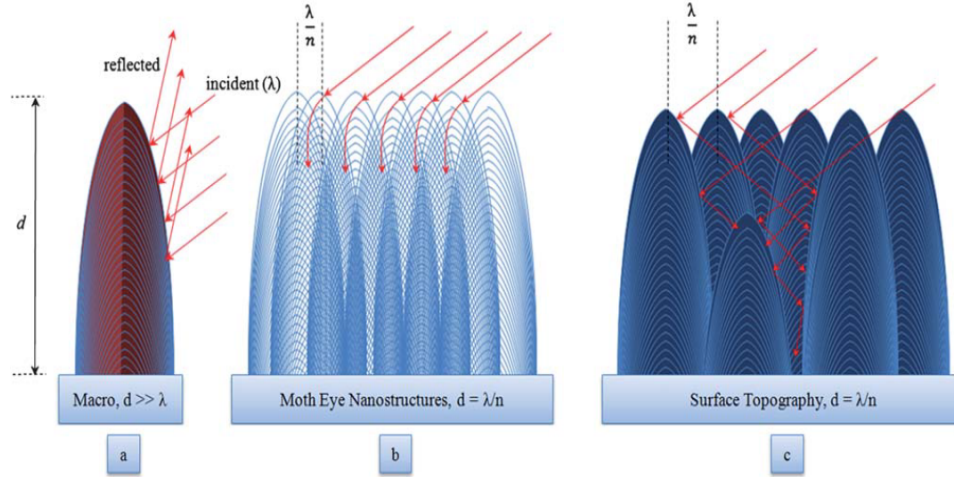


Figure 2.1: (a) Reflection occurs when light interacts with a macro-structure; (b) Rayleigh effect happens when the structures have comparable dimensions giving a GRIN surface; (c) In actuality, light experiences multiple internal reflections (from [4]).

of reflection is shown in figure **2.1(a)**. The reason MESs are so effective is from the structures being tapered guiding the light with multiple internal reflections toward the substrate as demonstrated in figure **2.1(c)**. As light with dimensions greater than the structures comes into contact with the surface, figure **2.1(b)**, the tapered structures gives the surface a gradient RI profile invoking the radiation to have a Rayleigh effect [4]. The following sections will discuss how AR surfaces using SWSs are able to be polarization-insensitive, quasi-omnidirectional, and broadband.

2.1.1 Polarization Sensitivity of SWS's

The polarization sensitivity for anti-reflective structures (ARSs) largely depends on the dimensions of the MES. The transmittance and reflectance are the same for *TM* and *TE* polarizations at normal incidence because the structures have equal periods in both x and y directions [12]. Figure **2.2** shows a 1-dimensional

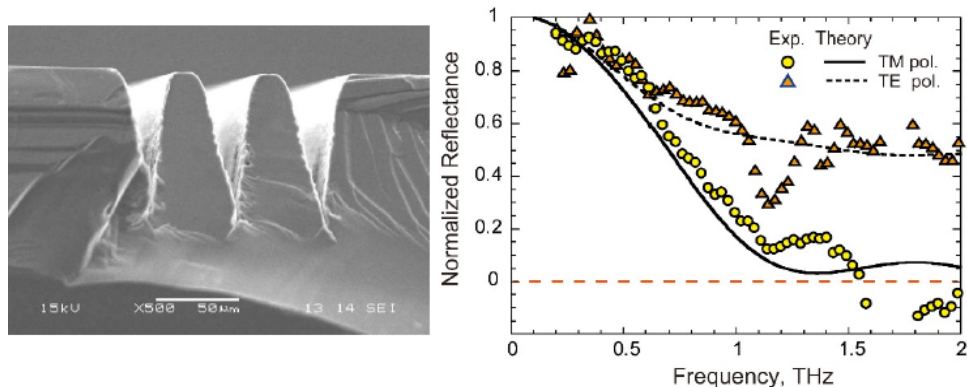


Figure 2.2: (Left) SEM (Scanning Electron Microscope) image of periodic tapered structures with a depth = 90 and pitch = 51 μm which are one dimensional and fabricated by femtosecond laser processing. (Right) TE and TM polarizations are represented by the theoretical and measured power reflectance for structures with a depth = 50 and pitch = 25 μm . A Si exterior with no grating structures has a reflection coefficient of 0.3 which is what the reflectance is normalized by (from [5]).

(1D) MES that is able to filter the TM polarization of light and to some extent TE polarization since the surface may be considered porous. This is due to the dimensions of the MES. This phenomenon regarding the results shown here is inherent to nature when light interacts with a surface. Figure 2.3 depicts the results for a 2-dimensional (2D) structure and its polarization insensitivity.

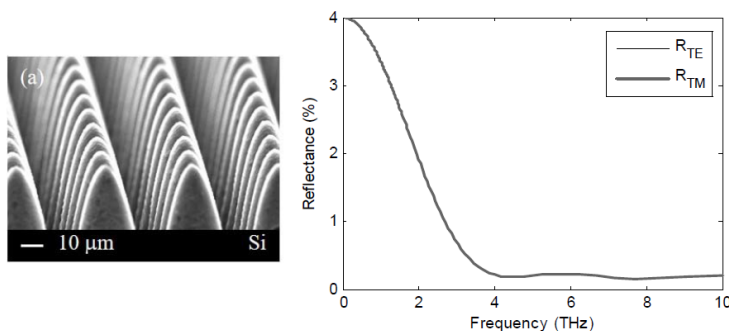


Figure 2.3: (a) Example of a 2D MES (from [11]). (b) 2D sub-wavelength gratings with depth $d = 30$ and period $\Lambda = 15 \mu\text{m}$ with calculated reflectance at normal incidence for TM and TE polarizations with $n = 1.5$ (from [12]).

At greater angles of incidence, even the 2D ARSs start to show some dependence. This may be due to the grazing and Brewster angles which also affect omnidirectionality. Figure 2.4 shows a contour plot of both TE and TM polarizations on an AR surface of SWSs. The exceptional transmittance in figure 2.4(a) may come from the Brewster angle known for TM polarized light. Notice the wavelength dependence for both polarizations. This might be due to the ARSs being wavelength-dependent, therefore, the results also will be. As the angle of incidence increases to more oblique angles, the wavelength dependence starts to disappear which might be due to the grazing angles. At these angles, typically greater than 60° , the reflectance value starts to quickly increase. Even though the Brewster angle affects the TM polarization so greatly, this may be negligible by observing figure 2.4(b), at 60° the reflectance is about 1%. It can be seen at oblique angles of incidence there is polarization splitting.

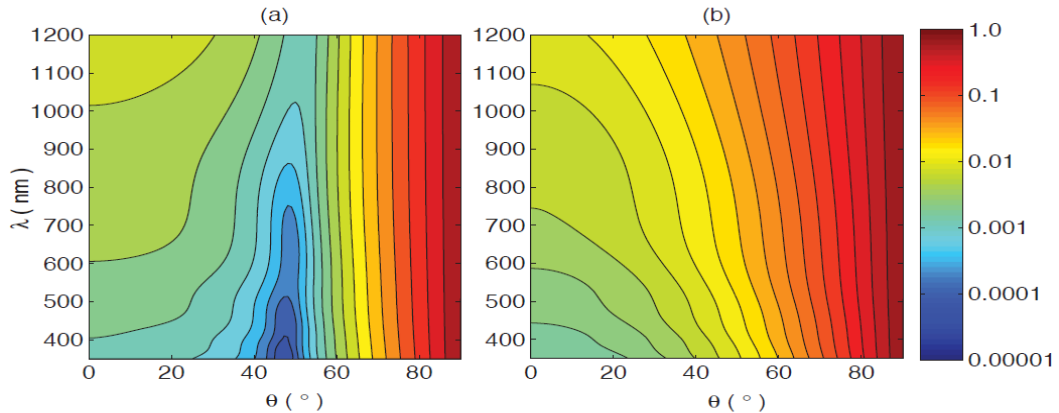


Figure 2.4: A log scale is provided to emphasize the variation of the reflectance characteristics of polarized light interacting with a parabolic SWS's surface which have a depth of $d = 550$ and pitch of $\Lambda = 100$ nm covering the lambda-theta space which ranges from 350 to 1200 nm and angles of incidence ranging from 0° to 90° . Surface reflectance for (a) TM polarized light and (b) TE polarized light (from [34]).

2.1.2 Omni-Directionality of SWS's

The research into the MES's shape has revealed that the dimensions of the structure will determine whether the filter will be relatively omnidirectional. Figure 2.5 demonstrates the more tapered the structure is the more AR the surface will be at normal incidence. If tapered structures have this effect at normal incidence then at oblique angles the tapered structures should be less omnidirectional. Judging the trend of the tapered shapes and their anti-reflectivity, conical structures such as a pyramid should be more effective at incident angles than the moth-eye structure. The paraboloid is the easiest profile to fabricate in addition to being the most mechanically robust but yields worse ideal AR characteristics than the cone, it will therefore be more likely to be a more acceptable AR surface using a paraboloid SWG (sub-wavelength grating) for space operations [34]. Pyramid type structures are also mentioned in [4] which enable numerous internal reflections since the planes of the structure keep the greatest proportion of light in optical captivity by ensuring the incident angle is at a grazing angle.

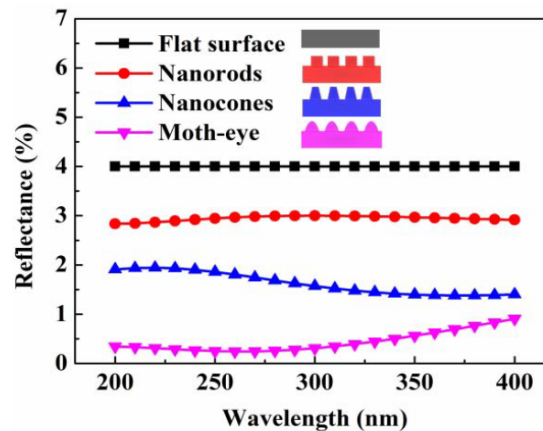


Figure 2.5: Nano-structured glass having dimensions of 100 nm with varying forms that are a function of wavelength with the calculated reflectance at normal incidence (from [29]).

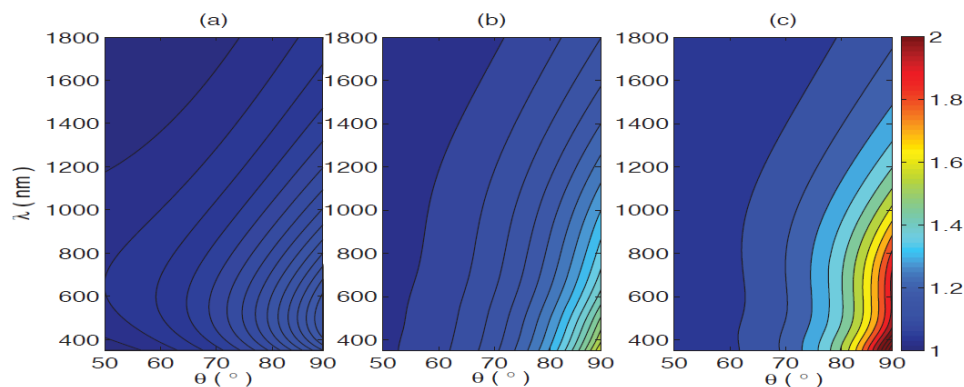


Figure 2.6: (a) MgF₂ ARC, a conventional thin film; profiles with dimensions of depth $d = 550$ and pitch $\Lambda = 100$ nm for defined structures of SWG AR surfaces of (b) conical, and (c) parabolic. Contour plots of the transmittance ratio between various AR methods and bare cover glass under the illumination of oblique angles of incidence and unpolarized radiation (from [34]).

Figure 2.6 shows the transmittance of wavelengths for solar cells mounted to nano-satellites. These plots show that SWS's are more omnidirectional than conventional thin-film ARCs and the moth-eye parabolic structure increased the transmittance at more oblique angles than the conical pyramid structure. Notice the wavelength dependence again, the high transmittance at those wavelengths are close to the dimensions of the ARS. This leads to non-tapered structures and their omnidirectionality.

The cylindrical pillars' performance is greater than multi-layer thin film conventional methods, and to moth-eye structures, which are known to need enormously great heights to deliver low reflectance at wide angles of incidence; cylindrical pillars are capable to produce high optical transmittance for both *TM* and *TE* polarizations [26]. The shortcoming of these structures is the efficiency of filtering at incident angles. These structures may be more effective at oblique angles of incidence.

As seen in figure 2.7, non-tapered structures filter entirely differently than

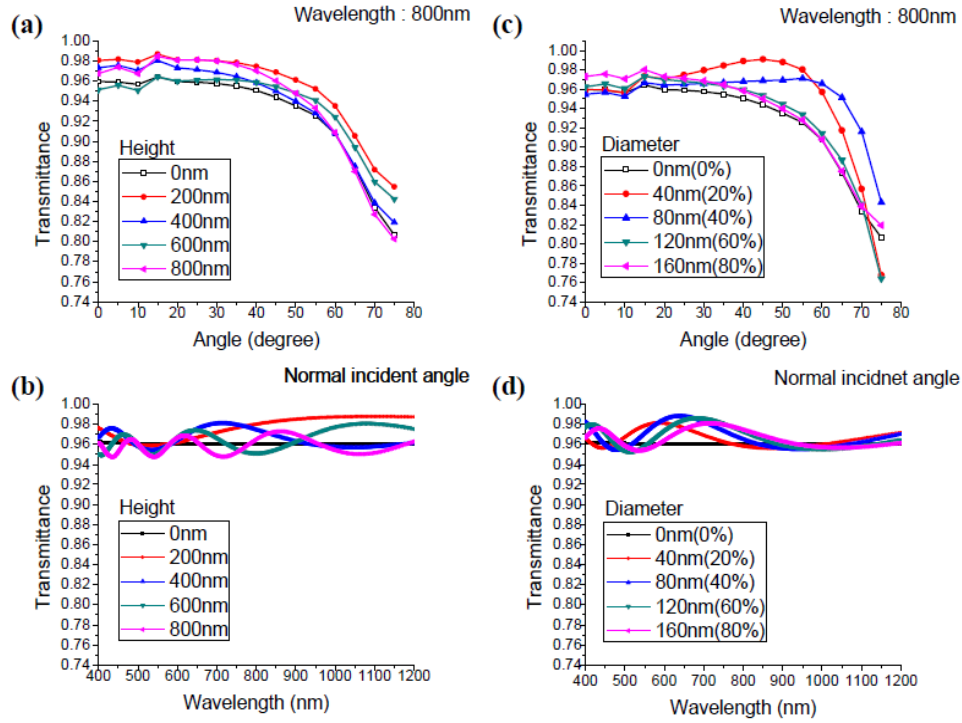


Figure 2.7: How transmittance is affected by the dimensions of the cylindrical pillar. The pillar on top of the surface has a varying Height = 0 to 800 nm, fixed period $\Lambda = 200$ nm, and diameter $D = 40$ nm for (a) angles of incidence and (b) radiation in wavelengths at normal incidence. The structure layer is evaluated by varying the filling fraction which is done by the Diameter = 0 to 160 nm in (c) and (d) (from [38]).

tapered structures. With tapered anti-reflective gratings (ARGs), the more depth the structure has the more AR the filter becomes. Clearly, by observing figure 2.7(a),(b), the height of the structure affects omnidirectionality and causes wavelength dependence across the spectrum. Unlike tapered structures, the shorter the pillar is the more omnidirectional and greater transmittance. At incident angles, these structures are seen by light as simply a porous layer effectively lowering the RI as seen in figure 2.5. How effective the filter behaves also depends on the filling factor, the diameter/period, which figure 2.7(c),(d) indicates.

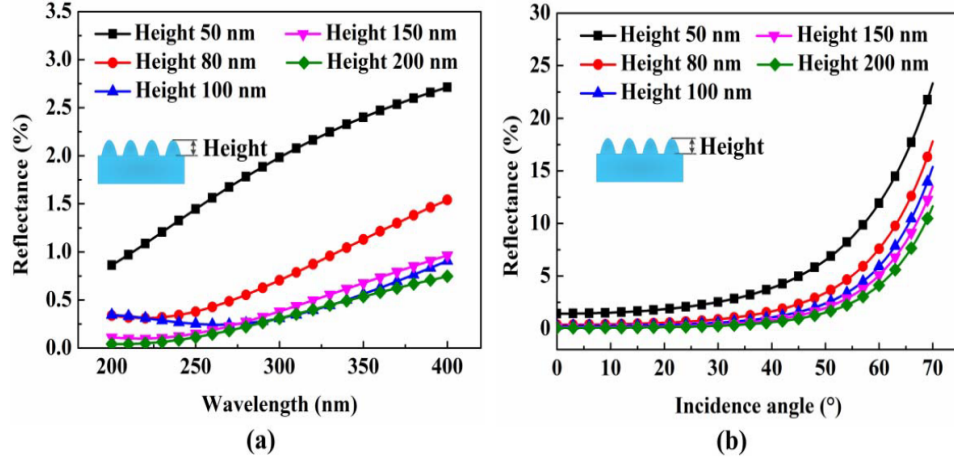


Figure 2.8: The reflectance is calculated at (a) normal incidence and (b) a wavelength of 250 nm for different incidence angles. The height is varied for the moth-eye glass nano-structure with a period = 100 nm (from [29]).

As seen in figure 2.8, with tapered SWGs the more height the structure has, the more omnidirectional and broadband the surface becomes due to the aspect ratio (height \div diameter). Unlike non-tapered structures, these SWG's don't have a fill factor. Their pitch/diameter is the same as the period which is elucidated in figure 2.9, the base of these structures are typically connected to their neighbors for optimal filtering. Higher orders of diffraction can be explained by Bragg's Law which is constructive interference leading to maximal reflections; the periods greater than 100 nm reveal the rise in the likelihood to reflect at certain occurrences in the spectrum indicating Bragg's Law [29]. Even though the grating is a SWG, the transmitted and reflected waves are not distorted due to only the zeroth-order diffraction rays are induced [23]. Non-tapered structures are able to propagate higher orders of diffraction which may be due to the fill factor.

A contour map showing the reflectance of various ARGs in figure 2.10 as a function of structure height and wavelengths across a chosen spectrum. The length between the individual pillars are 10% of 300 nm which is the period and

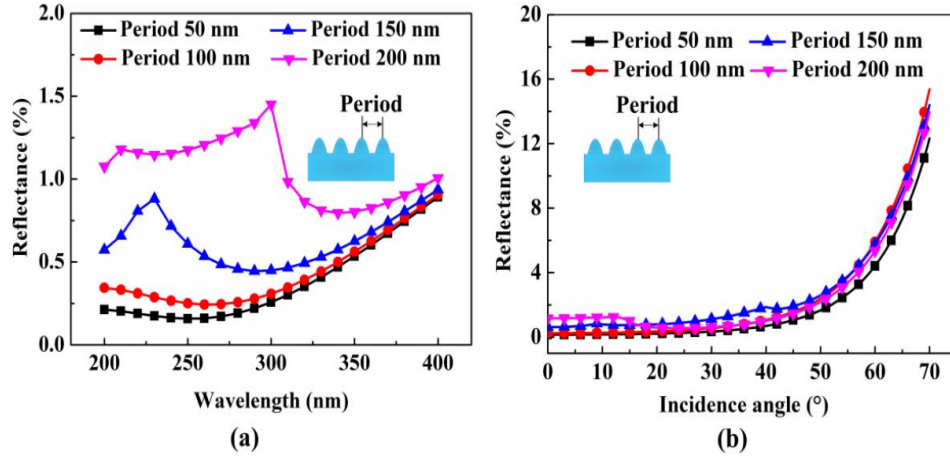


Figure 2.9: The reflectance is calculated at (a) normal incidence and (b) a wavelength of 250 nm for different incidence angles. The period is varied for the moth-eye glass nano-structure with a height = 100 nm (from [29]).

the truncated cone has an apex diameter that is 50% of the base diameter [43]. Tapered and non-tapered structures have to be optimized separately as seen in the previous figures causing the structures to have different dimensions. Here the tapered structures were optimized and compared to a non-tapered structure with the aim of comparable dimensions leading to the non-tapered results to deteriorate. With only a 10% fill factor, light basically sees this as an abrupt surface causing reflections. Figure 2.5 seems to also simulate the ARGs with the same dimensions causing the results of the tapered structures to suffer which is made evident in figure 2.8 and figure 2.9. At perpendicular

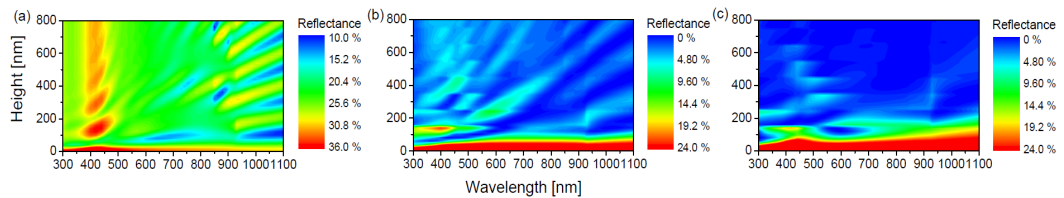


Figure 2.10: Contour plot displaying the reflectance being a function of wavelength and height for hexagonal arrays which have a period of 300 nm for (a) nano-rod, (b) truncated cone, and (c) perfect cone (from [43]).

incidence, the conical shapes should give the optimal AR surface; the parabolic profile should yield lower reflection than the non-tapered structures but higher than conical structures [42]. Figure 2.11 displays how fast the transmittance depreciates when the non-tapered structure, evaluated at an oblique angle, is tapered gradually. Non-tapered structures may operate more efficiently at an oblique angle of incidence compared to tapered structures, which are very sufficient at normal incidence.

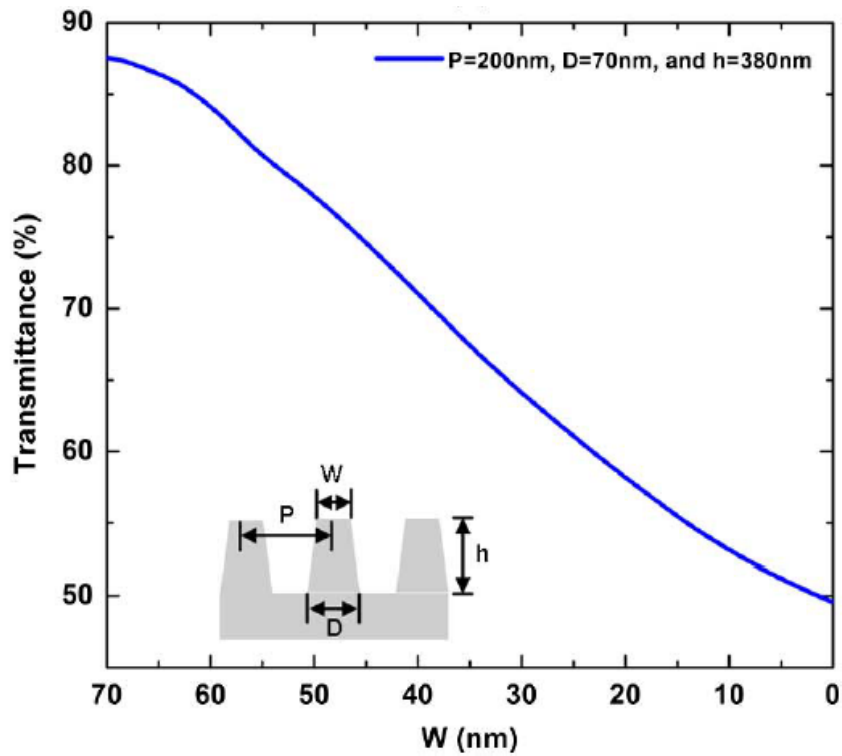


Figure 2.11: The inset is an illustrative graphic showing how the simulations were performed as a function of the top diameter (W). Simulated spectra of transmittance evaluating the impact of tapering a pillar type structure at incident wavelength $\lambda = 500$ nm, angle of incidence $\theta = 85^\circ$, periodicity $P = 200$ nm, diameter $D = 70$ nm, and height $H = 380$ nm under 45° polarization (from [26]).

2.2 ARCs Using Thin Films Filtering Fundamentals

Conventional deposition methods are not able to deposit, at this current time, robust films that would provide adequately small refractive indexes with traditional coating materials for the substrate-air interface that would bring forth wide-angle broadband designs [31]. Acquiring polarization-insensitivity, omnidirectionality, and a broadband spectrum using a thin film ARC as a filter is challenging due to the materials available in nature with a low RI. To acquire admittance or impedance equalization in both phase and magnitude, optical thin films using quarter-wave stacks are customarily used as homogeneous anti-reflection coatings; applications of these coatings are typically restricted by the material accessible in nature with a low RI [26], there are not sufficient materials having a refractive index under 1.3 in the Terahertz (THz), solar, and visual spectral region [12]. With ARGs: the refractive index, shape, pitch/diameter, and height/depth all affect how the filter will behave pertaining to the three main characteristics of a filter listed above. Conversely, thin film ARC's only parameter that affects how the filter will behave is the RI.

More than 30% of incident light is lost due to reflection off the surface of the solar cell (photovoltaic) if it is made of silicon. In 2004, silicon photovoltaic panels constituted for 36% of manufactured solar panels; a solar cell (photovoltaic) ideally would absorb all photons and convert them into electrical charges [22]. Figure 2.12 depicts the optical phenomenons of reflection and refraction, it demonstrates why the need for AR surfaces is desired. Notice the reflected angle is the same as the incident angle and the refracted angle is not. Here, the refracted index n_1 is in air and n_2 is in GaAs. Abrupt surfaces are materials with refractive indexes that are much higher than the preceding RI in which the light is traveling from, causing these phenomenons. At more

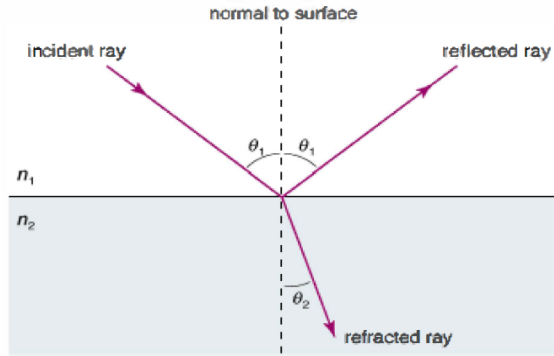


Figure 2.12: Light refracting and reflecting off a GaAs substrate used for solar cells (from [42]).

oblique angles, eventually the grazing angles will be reached and much less light will begin to refract into the substrate. Polarized light characteristics need to be assessed when the angle of incidence is not zero [42].

The polarizations, TM and TE , are averaged when considering the reflectance of sunlight since it is presumed to be randomly polarized [39], which is shown in figure 2.13. From observing the plot, at normal incidence (0°) where the sun would be at noon (zenith) if the solar panel is on a flat rooftop, the TE polarized (green), TM polarized (blue), and unpolarized (red) reflected light has the same magnitude of reflection. As the sun progresses to sunset, a lower azimuth angle where the angles of incidence (AOIs) are larger, the TE polarized light only increases in reflectance and the TM polarized light decreases to zero reflection around 75° which is the Brewster angle for this substrate. The unpolarized light is constant up to 60° and starts to exponentially increase afterward as does the TM polarized light after 75° towards the critical angle. For any surface, at 90° , the reflectance is unity (1) [31]. Notice at normal incidence that all polarizations of light begin a little above 30% reflectance which is due to the RI and is why ARSs are so effective because an effective RI can be reached using ARGs which can be seen in figure 2.14.

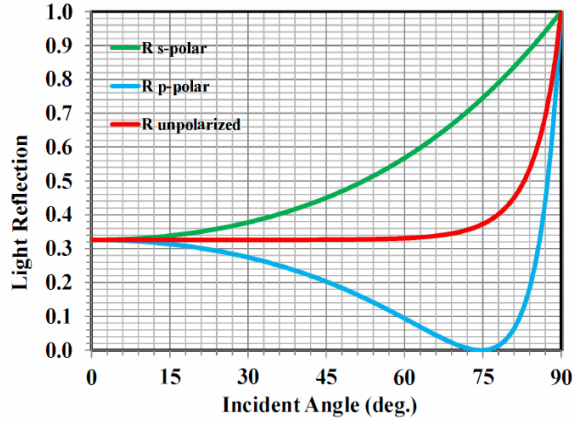


Figure 2.13: Various incident angles with the amount of light reflecting off a GaAs flat-plane substrate (from [42]).

A material's refractive index is divided, at wide AOIs, into two individual effective refractive indices [32], for TE and TM polarizations which is why at grazing angles omnidirectionality is so complicated.

Regarding the subject of anti-reflectivity, effective medium theory (EMT) is a crucial concept that is the foundation of numerous numerical works and modern models [4]. The effective refractive index can be determined using EMT which is calculated by the volume of the material etched out of the substrate and is demonstrated in figure 2.14 and figure 1.2. This explains why non-tapered structures act as a single layer and tapered structures having the effect of a multi-layer ARC. A wider bandwidth may be acquired by setting layers with different refractive indexes, creating a multi-layer coating [21]. Multi-layer



Figure 2.14: Different SWG shaped structures displaying the rectangular (left), trapezoidal (middle), and triangular (right). The shading color displays the effective refractive index corresponding to various nano-grating forms relating to the thin film ARCs (from [42]).

ARCs achieve lower reflection loss across a wide spectrum of wavelengths and wider AOIs from the gradual change in the effective refractive index with values that are unobtainable for single layer quarter-wavelength ARCs.

Half a century of inspecting homogeneous multi-layer thin films considerably has delivered an abundant diversity of multi-layer thin film strategies as a consequence and design techniques [35]. An example of a homogeneous thin film quarter-wavelength ARC is illustrated in figure 2.15(a). The orange arrow is the incident light and the red arrow R_1 is the reflection. The beam of light incident upon the thin film has a wavelength (λ) that determines the thickness (d) and this length is one-quarter of the light's wavelength giving $d = \frac{\lambda}{4n}$ [4]. This allows destructive interference to occur which causes the surface to be AR. The yellow arrow entering the thin film medium n is the refracted light which then proceeds to reflect causing the refracted light R_2 . By this time, R_2 is a 180° out of phase or π radians from R_1 causing the magnitudes of R_1 and R_2 to cancel each other. For a single-layer thin-film on a substrate surrounded by air, zero reflectance can be obtained with the refractive index having a value $n = \sqrt{n_{air}n_s}$, the n will entirely depend on n_s since n_{air} is unity [4].

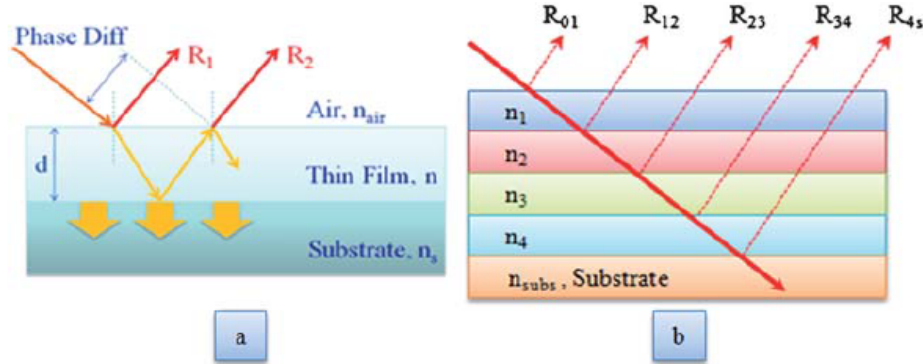


Figure 2.15: (a) A single layer film on a substrate depicting how rays of light propagate through the ARC and a (b) multi-layer film (from [4]).

Thin films decrease reflection to exceptionally low values for the designed wavelength, ideally to zero; reflection approaches asymptotically towards the reference value (no anti-reflection used) for the other wavelengths, but will never surpass it [12]. As previously mentioned, the RI of thin films can be lowered by making them porous. Multi-layer structures containing air gaps entirely are devoid of structural solidity even though they have been accredited, causing them to be inapt for many implementations [17]. If the RI of the layers rises linearly from the air to the material of the substrate, a broadband anti-reflection effect may be acquired with laterally homogeneous layers [13].

Lord Rayleigh quoted in 1880, “No one would expect a ray of light to undergo reflection in passing through the earth’s atmosphere as a consequence of the gradual change of density with elevation.” Light and sound reflections were diminished by equipment that applied this very idea several decades later [32]. This gradual RI effect was replicated through a chemical etching process and

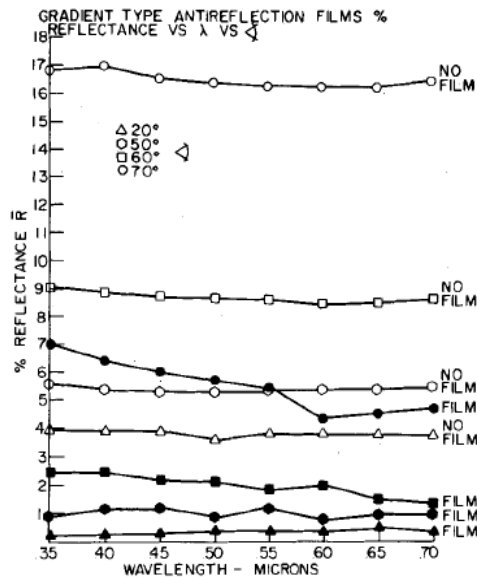


Figure 2.16: Reflectance averaged with $[\bar{R} = 1/2 \cdot (R_s + R_p)]$ as a function of AOIs and wavelength for glass without a film and glass coated with the anti-reflection gradient-type film (from [30]).

the results are shown in figure **2.16**. The film's characteristics signify a gradient refractive index due to the film containing a porous narrow layer mostly made of silica from the etch leach process administered to the glass sensitized from a heat treatment inducing phase separation [30]. There were unforeseen results of wavelength dependence having periodic oscillations when the films were tested. The periodic oscillations are similar to the periodic maximum and minimum discerned for homogeneous discrete single-layer thin films; as the wavelength shrinks with respect to the film's thickness, the amplitude of the oscillations reduces, yet intensifies as the AOI ascends [30]. The wavelength dependence may be caused by the optical thickness of the film and the explanation of this is forthcoming. The λ scattering phenomena or the particular features of the refractive index profile may explain the decline in reflectance detected at longer wavelengths and wider angles [30].

Current normal-incidence AR coating methods normally perform with spectral ranges determined by largest wavelength λ_L and shortest wavelength λ_S giving $0.85 < \frac{\lambda_L}{\lambda_S} < 5$ [31]. The multi-layer quarter-wavelength thin films are more broadband with the addition of more layers, but in order to have a GRIN effect, more layers need to be added that are closer in RI to remove the abrupt surfaces and not be as sensitive to more oblique AOIs. An inhomogeneous ARC's optical thickness has to be greater than $1 \cdot \lambda_H$ or even $2 \cdot \lambda_H$, based on the premise of previous computations, this has been established [31]. This allows light to pass through the substrate as depicted in figure **2.17**. It has also been recognized that if λ_L is markedly longer than the wavelength for which the independent layers have an optical thickness that is half a wave, then spectral features similar to an inhomogeneous ARC can be estimated with many thin layers of identical optical thicknesses [31]. Figure **2.18** and figure **2.19** show the

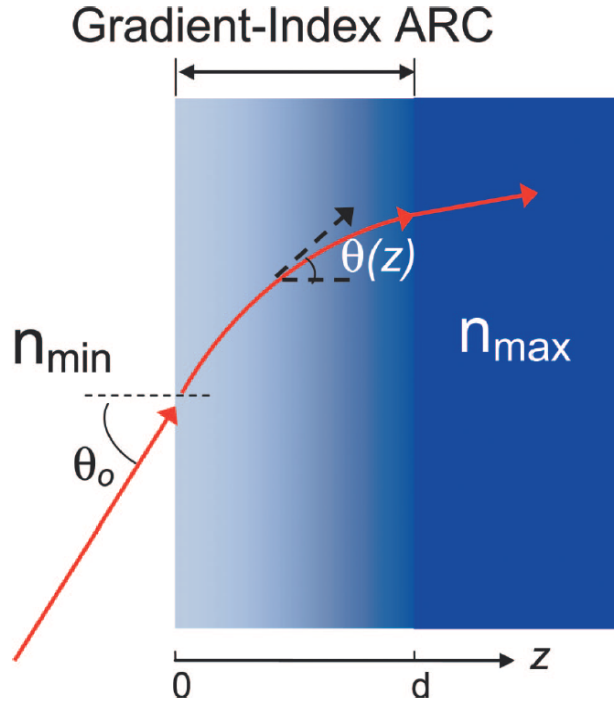


Figure 2.17: Light's refractive angular variation using a GRIN ARC (from [35]).

data of ARCs of multi-layer thin films numerically designed for unpolarized light at all AOIs with arbitrarily chosen RI values for the substrate and wavelength region. The optical thickness is considered the imaginary thickness perceived by the electromagnetic wave whereas the coating thickness is the physical thickness [35]. Typical quarter-wavelength ARCs have an optical thickness of $nd = \frac{\lambda}{4}$, at normal incidence this is a quarter of the wavelength but at other angles of incidence, light effectively sees a different thickness known as the optical thickness. A different effective optical thickness is discerned from the light beam invading at an angle of incidence being oblique causing a new material admittance and effective film thickness [32]. Multi-layer thin films should be based on the refractive and critical angles for improved filtering, otherwise, at oblique angles, the light could reflect in the middle of the inhomogeneous ARC at a critical angle. Allow $n \cdot d_{\theta_2}$ (angle of refraction θ_2) to be the effective

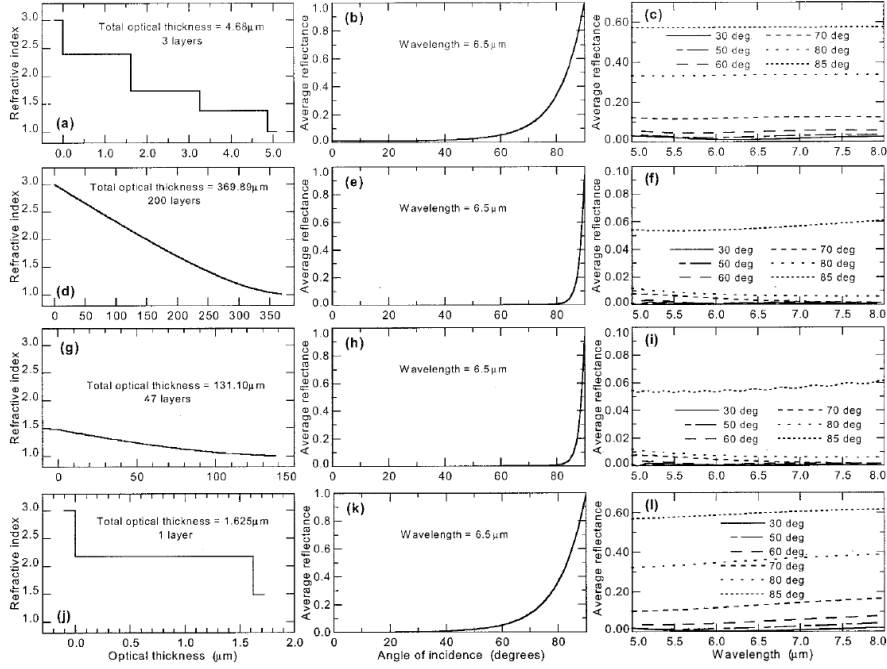


Figure 2.18: (a)–(c) A 3–1 interface for a standard AR coating with 3 layers; (d)–(f) A 3–1 interface for an AR coating with 200 layers; (g)–(i) A 1.48–1 interface for an AR coating with 47 layers; (j)–(l) 3–1.48 interface for a single layer AR coating. AR coatings with varying interfaces, (Column 1) the substrate’s optical thickness and refractive index profile; (Column 2) Unpolarized light’s averaged reflectance with angular variation; (Column 3) Average reflectance with a spectral variation of 30°, 50°, 60°, 70°, 80°, and 85° (from [31]).

optical thickness at an AOI for the sub-layer having an index n and $n \cdot d_0$ to be the optical thickness at normal incidence for the N sub-layers giving the expression $n \cdot d_{\theta_2} = n \cdot d_0 \cdot \cos(\theta_2)$ [31]. For greater AOIs, the greater the thickness of the films needs to be for optimal filtering. The greatest impact affecting the optical thickness is small refractive index materials and grazing angles; the refractive index profile becomes seriously distorted from observing the $\cos(\theta_2)$ (as it progresses towards 0 or $\theta_2 = 90^\circ$) [32].

Figures 2.18(j to l) are of a typical quarter-wave ARC. This filter is not omnidirectional and at oblique AOIs, the ARC starts to suffer even up to 60% reflectance. These results would be more degraded if the filter was surrounded

by air instead of another material. Figures **2.18(a to c)** is a GRIN ARC with only a few layers making the interfaces to be too abrupt causing polarization separation but has similar results to the quarter-wave thin film. By examining figure **2.13**, the multi-layers need to be also designed to keep the refraction angle from varying to largely or this will also cause polarization splitting. Figures **2.18(d to f)** is a GRIN ARC with enough layers that the radiation is guided to the substrate with less than 7% reflectance even at 85° . This filter may even be considered omnidirectional but at the cost of the thickness of the substrate needs to be to have this efficiency. Notice if the RI of the initial substrate can be lowered, then the thickness of the film can be lowered greatly by observing figures **2.18(g to i)**. These multi-layered GRIN ARCs would deteriorate if the individual thickness of the layers approached a half-wave and would essentially become absentee layers. If the layers are too thin then the overall thickness needs to be increased in order to keep the inhomogeneous profile. The reason the ARCs in figures **2.18(d and g)** may not be solutions implemented at this time is because of the total thickness of the multi-layered ARC and again the materials close to unity do not exist. These multi-layered GRIN ARCs would be more acceptable for a small spectral region giving a smaller total thickness of the filter. By observing figure **2.18(a and j)**, if a medium other than air is present on the ARC, a much more omnidirectional and broadband ARC is realizable.

The GRIN multi-layer ARCs could still be further improved, instead of having a linear RI profile, a more exponential increase in RI to the substrate has an extraordinary effect on performance for omnidirectionality, polarization sensitivity, and the filter being broadband. Figures **2.19(g to i)** shows enhanced performance with a total thickness of the substrate being substantially thinner

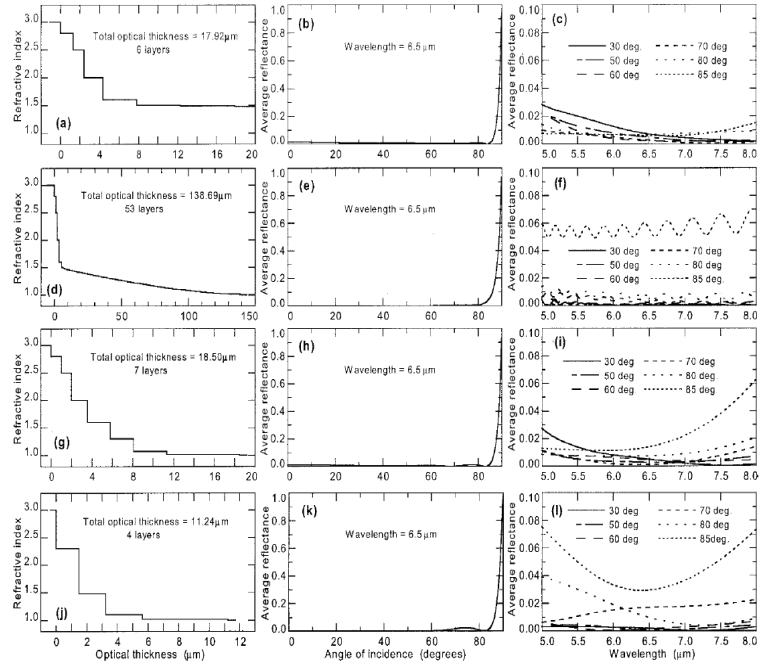


Figure 2.19: (a)–(c) A 3–1.48 interface for an AR coating with 6 layers; (d)–(f) A 3–1 interface for an AR coating with 53 layers; (g)–(i) A 3–1 interface for an AR coating with 7 layers; (j)–(l) 3–1 interface for a single layer AR coating. AR coatings with varying interfaces, (Column 1) the substrate’s optical thickness and refractive index profile; (Column 2) Unpolarized light’s averaged reflectance with angular variation; (Column 3) Average reflectance with a spectral variation of 30°, 50°, 60°, 70°, 80°, and 85° (from [31]).

compared to figures 2.18(d to f). By reducing the total thickness even further, the omnidirectionality suffers some and the reflectance remains less than 10% at oblique AOIs in figures 2.19(j to l). By observing column 3 in figure 2.19, the averaged reflectance is no longer constant across the spectrum contrary to figure 2.18. The periodic oscillations reappeared in figures 2.19(d to f), this may be due to the thickness of the multi-layer section not being wide enough between the transition from air to the substrate. This could explain why this wavelength dependency occurred earlier with the GRIN glass film. Figure 2.19(a) is possible to manufacture because the required materials needed exist.

The RI profile of gradient RI coatings may follow various curves that abide with the Rayleigh effect, such as: linear, cubic, parabolic, exponential, and quintic [4]. Quintic RI profiles seem to be regarded as an effective ARC. The minimum thickness of an inhomogeneous ARC is dependent upon the RI profile but a general minimum has been found. The reflection of a substrate may be repressed in the reflection spectrum when the optical thickness is greater than a half of the longest wavelength, this is a known empiric principle when assessing the imaginary thickness [33]. If the overall thickness of the ARC is too thin and the layers are also thin (or larger wavelengths $d \ll \lambda$) the electromagnetic field (EMF) perceives an abrupt interface because the radiation does not vary considerably inside the ARC. Conversely, $d \gg \lambda$, the RI profile appears to vary slowly with the ARC relative to the wavelength of the EMF.

Even with these smooth RI profiles, there is still polarization dissociation as depicted in figure 2.20. These “exponential” RI profiles are usually modified based off the refractive angles inside the ARC to further improve the abrupt interfaces seen by light in the inhomogeneous ARC which would enhance

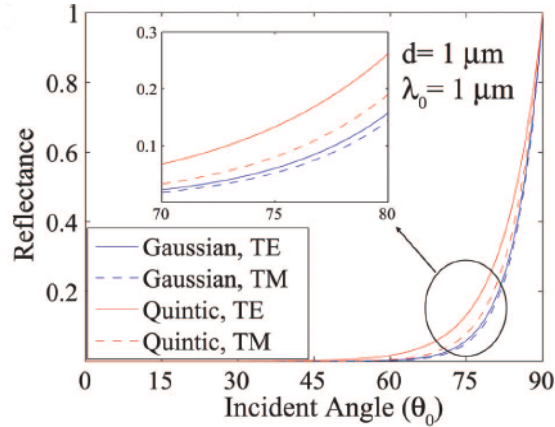


Figure 2.20: The physical thickness of the gradient index (Quintic and Gaussian) coating is $1 \mu\text{m}$. The angular reflectance is calculated for a wavelength selected at $1 \mu\text{m}$ (from [35]).

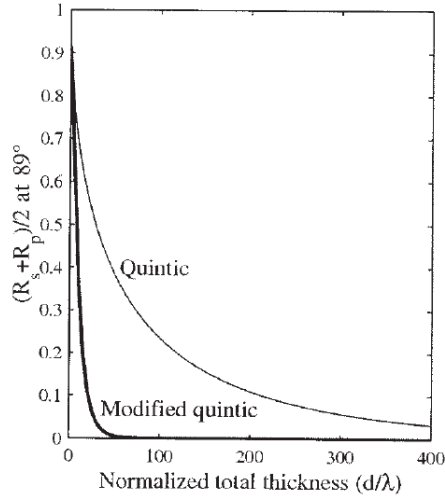


Figure 2.21: The varying reflectance, at an incident angle of 89° , is a function of the genuine and modified Quintic total thickness profiles which are normalized (divided) by the wavelength (from [32]).

the omnidirectionality and to help with the polarization sensitivity which is illustrated in figure 2.21. A minimal thickness is estimated to be $50 \cdot \lambda_0$, in many circumstances for thin-film intentions is problematic, to attain an acceptable angular performance at the wavelength λ_0 [32]. This modified RI profile is so sharp in the middle of the film shown in figure 2.22 that the shorter wavelengths see a more abrupt surface because that portion of the film has a thinner thickness to transition from a high to low RI which leads to a narrower spectrum that can be filtered. The reflectance at near-normal incidence will also be higher than the original quintic curve due to that same portion of the film being thinner. At very wide oblique AOIs, the thickness at the ambient-ARC interface portion of the ARC needs to be wide enough that the RI profile approximates the preceding RI which is why this modified quintic profile is so effective because the physical thickness at the ARC interface portion is very wide. This modified quintic profile has exceptional polarization sensitivity and consistently low reflectance across almost all AOIs. This improvement inflicts

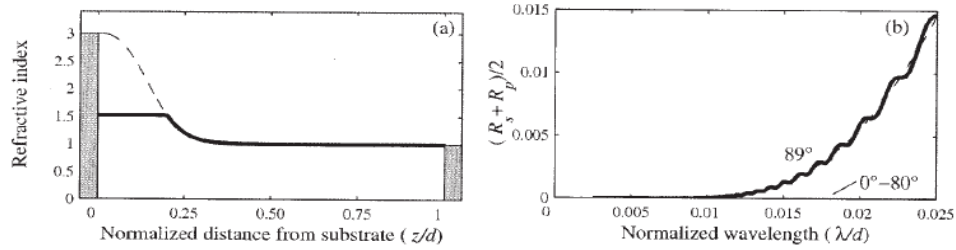


Figure 2.22: (a) Profiles of the refractive index and (b) the spectral reflectance is averaged with the incidence angles from $0\text{--}80^\circ$ and 89° . The performance is compared to a modified quintic profile that is an inhomogeneous AR coating devised for the interface between mediums with indices of refraction of 1 and 3; The other AR coating contains a portion of the identical quintic profile having a substrate with a 1.5 index of refraction (from [32]).

modest performance deterioration at nearly normal incidence of the film and imposes an enlarged physical thickness [35].

An unexpected phenomenon is seen in figure 2.22, an entirely new material is implemented for the substrate to agree with the improved truncated profile extracting a sizeable section of the modified quintic profile from the substrate region of the coating [32]. The reason this is possible is due to the RI because it is still gradually changing from air to the substrate. The reflectance did not significantly vary which is shown in figure 2.22(b). It can be seen that it is still omnidirectional and polarization separation did not occur.

By taking into account the critical and refractive angles, which improved the exponential RI profiles greatly, this lead to a new principle of GRIN ARCs. By solely focusing on making the propagation path (refractive angle) in the inhomogeneous ARC a gradual angular transition to the substrate at wide AOIs instead of the RI profile, the GRIN ARCs could still be further improved without the additional thickness of the ambient-ARC interface which is illustrated in figure 2.17. It was noted earlier that wide angles directly lead to an increase in reflection by observing figure 2.13, therefore instead

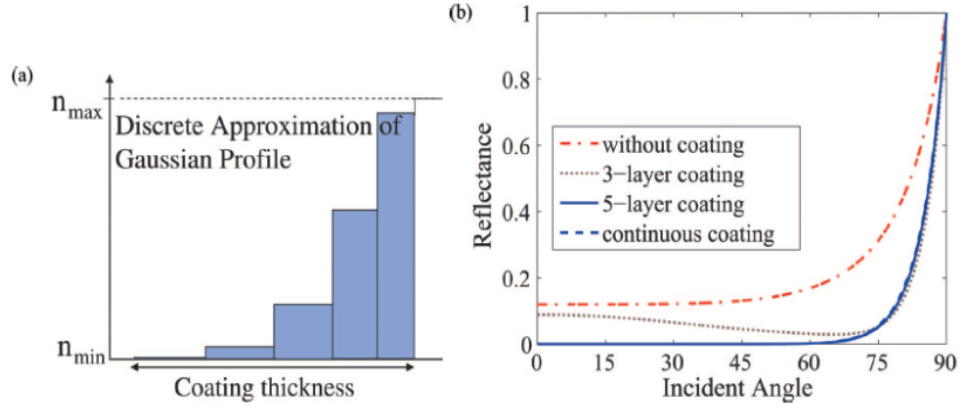


Figure 2.23: (a) Discretized Gaussian profile with five layers between AIN (RI = 2.06) and air. (b) Gaussian profiles with differing numbers of discrete layers with respect to angular reflectance (from [35]).

of improving polarization sensitivity by a smooth RI profile, the RI profile will be designed to give a smooth transition in the refractive angle which is more direct and effective. The angle of refraction inside the coating, θ_2 (or θ_z in figure 2.17), decides the optical approach that light will propagate within the coating which may be attained from Snell's law [35], Snell's law is (2.1) which is from [31] and is demonstrated visually in figure 2.12. By applying discretization to the continuous RI profiles which can be seen in figure 2.23, the polarization sensitivity and omnidirectionality are not significantly affected. This method is considered to be superior to the multi-layer quarter-wavelength ARCs and the GRIN ARCs based on the RI profile. The thin film close to air is included because there is technology such as oblique-angle deposition that can produce porous thin-films. The nano-rod SiO_2 layer has an effective index of refraction of $n = 1.08$, which may be the lowest for thin film mediums to be announced at this time [17].

$$n_1 \cdot \sin(\theta_1) = n_2 \cdot \sin(\theta_2) \quad (2.1)$$

Solar cells acquire anti-reflection typically by the use of thin-film ARCs [39]. Solar cells have advanced so far that wavelengths as small as 300 nm can be harvested, this requires the quarter-wave thin films thickness to be extremely accurate. Some of the more popular ARCs for tandem solar cells are interference-based step-down coatings. For this situation, the electric current mismatch may intensify regarding the coating if any departure from optimal occurs with the instrument [24]. Since the refractive index is based on the material, there is another concern for the process of assembling the different materials together. Thin films with multiple layers primarily have increasing debonding complications caused by thermal coefficient variations between the adjacent layers or the adjoining layer and the substrate constantly revealing to have

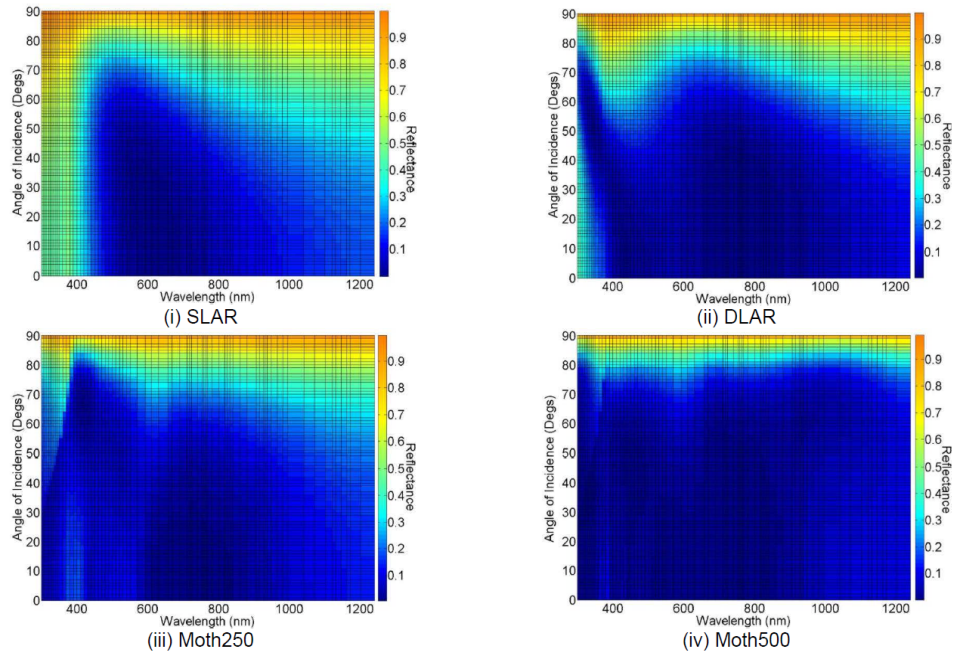


Figure 2.24: Different ARCs with their reflectance being a function of incidence angle and wavelength. (i) The single layer (SLAR) is CeO , $n = 1.953$, $d = 78$ nm. (ii) The double-layer (DLAR) is MgF_2 , ZnS , $n_1 = 1.38$, $n_2 = 2.3$, $d_1 = 107$ nm, $d_2 = 56$ nm. (iii) + (iv) The moth-eye AR surface of SWS's have a diameter of 200 nm and a height of 250 and 500 nm respectively (from [39]).

adhesion difficulties [4].

A comparison between thin films and ARSs is shown in figure **2.24**. It can be seen that the ARGs filter across the entire spectrum of wavelengths and angles efficiently. The SWG in figure **2.24(iv)** is constantly filtering across the entire spectrum up to about the incident angle of 80° and at less than 30% reflectance. This aspect is especially coveted for certain equipment, light-emitting diodes (LEDs) and solar cells need productive ARCs across a large range of angles of incidence [35].

The materials in nature used in thin-film ARCs are an extensive hindrance for devices that need robust filters, unable to be made porous which can be seen in the figure above. By simply etching onto the surface of the device, light can be captured and the surface can become an AR surface which is demonstrated in figure **2.25(a and b)**. When the MESs is smaller than the smallest wavelength of interest in the spectrum, a wide bandwidth can be filtered which is portrayed in figure **2.25(c and d)**. The silicon wafer is black owing to the surface being AR illustrated in figure **2.25(e)**.

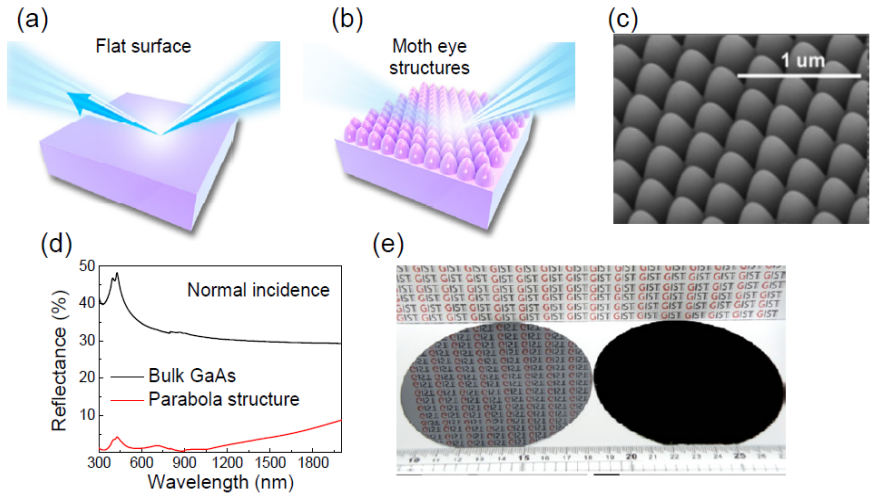


Figure 2.25: Conceptual illustrations of the reflection of light on (a) a smooth surface and (b) moth-eye structures; (c) SEM image of anti-reflection artificial structures that have the contour of a parabola; (d) A mere GaAs substrate and a GaAs substrate with an AR parabola surface results for measured reflectance; (e) The picture of the mere 4” silicon wafer (left) and a silicon substrate having the moth-eye structures (right) (from [37]).

2.3 Design Concerns for AR Surfaces using SWSs

There are many different design methods that affect how well the filter will behave. A LED projects from the inside out, therefore a double-sided AR surface can be used to help propagate the light through the screen and to help keep glares from appearing on the screen itself. The layout of these ARSs is usually in a square or hexagonal array. Hybrid ARCs may be able to achieve complete omnidirectionality by combining thin film coatings and ARGs. This may also be acquired by etching the SWGs onto a rounded surface. There are also different perspectives of how to improve the filtering ability such as inverse MESs and multi-level SWGs.

2.3.1 Multi-Level and Inverse SWSs

Multi-level and inverse MESs are based on the concept of EMT which is depicted in figure 2.14 and figure 1.2. An example of both these concepts is illustrated in figure 2.26. Inverse ARSs can be recognized if the surface is flat and seems to be made porous but a cross-sectional view would reveal the inverted ARG, even though it would also show upright SWG, which is evident in the figure below. ARSs (not inverted) are protrusions on the surface since the material has been etched away to produce these structures. The figure 2.28 can be considered an inverted ARG even though it was never referred to as so in the literature. Multi-level structures have the goal in mind to replace quarter-wave thin films by simply removing material from the substrate to create porous layers. The multi-level inverse SWGs were found to be less effective at normal incidence but more effective than the multi-layer step-down interference-based ARCs at wide AOIs according to [14]. This method may be more suitable for lasers and milling machines to produce these types of filters.

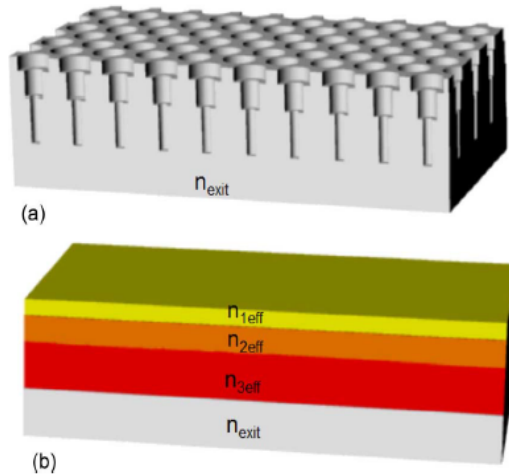


Figure 2.26: (a) A depiction of an AR structure with three layers approximating the effective index of refraction for each layer (b) multi-layer thin film structure would have (from [21]).

2.3.2 Double-Sided AR Surfaces and Layout Design

As mentioned earlier, some devices require double-sided AR surfaces. Figure 2.27 illustrates a double-sided AR surface with the same dimensions on both sides of the filter. These double-sided AR surface's not only aids in making the surface AR but also assists in transmitting the electromagnetic waves through the filter which is evident in figure 2.28. All double-sided AR surfaces significantly increased the transmittance of the filters in the references that even considered measuring this type of design [14], [15], [21], [25], and [29]. For some contrivances that produce light from within to the exterior such as a display panel, the internal reflection needs to be contemplated due to the refractive index of the incident material being greater than the transmitting media [43]. The LED's transmittance of light is considerably insufficient, ascribable to the internal reflection at the border between the medium of the LED and its encompassing material, inducing the LED's external quantum efficiency to be nearly deficient [23]. Therefore, the internal ARGs need to have much smaller dimensions than the external ARSs.

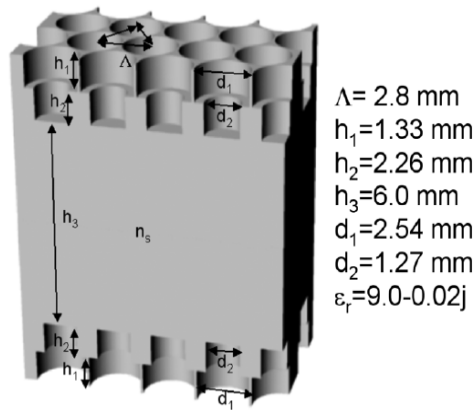


Figure 2.27: Devised to be anti-reflective inside the Ka-band (32–38 GHz), the Rexolite block is machined on both the top and bottom sides with inverse moth-eye shapes producing an AR surface (from [14]).

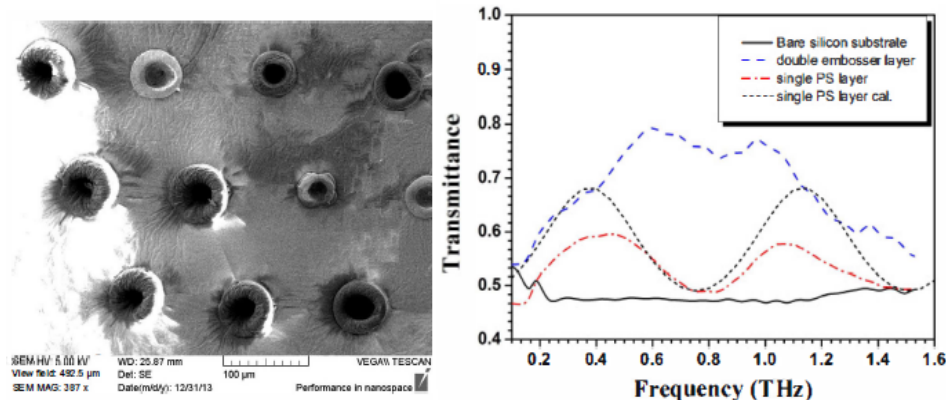


Figure 2.28: (Left) Hot-embossing and imprinting with needles produced the anti-reflection structure shown in the SEM image. (Right) The smooth high resistant silicon (HR-Si), hot-embossed samples of single-layer polystyrene (PS), double-sided PS, and calculated single PS layer with their transmittance spectra (from [15]).

Figure 2.29 illustrates the arrangement of the ARSs that are usually laid in this fashion for filtering the desired wavelengths. By observing these patterns, the hexagonally patterned filter’s results are not surprising. From an EMT point of view, more of the substrate’s volume is removed since the SWGs can be more closely packed together. This allows the substrate to act more like a GRIN filter. Hexagonally constructed filters are also more effective for regular ARGs. By observing the rectangular array, conceptually the ARSs (not inverted) might permit light to reflect down the “hallways” allowing the light to escape. Statistically, the probability that light is escaping in this manner might be due to the SWGs laid in vertical and horizontal lines is very likely which would explain why its results are so much worse than the hexagonal architecture. With hexagonally designed filters, the neighboring ARGs fully capture the light with multiple internal reflections being entirely surrounded.

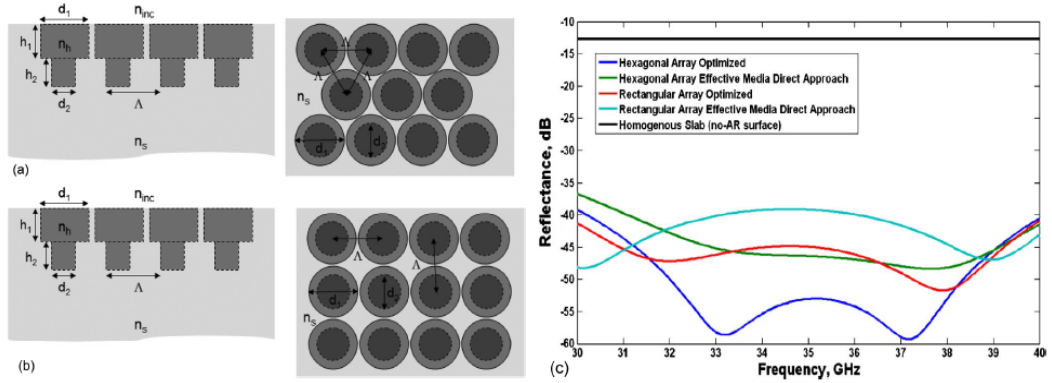


Figure 2.29: Depicted are the configurations for a hexagonally aligned array (a) and for a rectangular aligned array (b). (c) The rectangular and hexagonal arrays are both AR surfaces under irradiation at normal incidence for the simulated results graphing the reflectance in dB while being a function of frequency. The substrate media has a dielectric constant of $\epsilon_r = 2.56$ for the AR inverse moth-eye models (from [14]).

2.3.3 Completely Omni-Directional Designs

By observing figure 2.30, with the eye having a spherical shape, this causes light to always be incident on the MESs no matter how wide the AOI is. This could still capture light effectively even up to an AOI of 90° . What is also interesting to see in figure 2.31 is the hexagonal structures containing the MESs. By examining this figure, it seems that these hexagonal structures have depth and if this is true then this leads me to believe that two wavelength spectrums being filtered which may overlap causing an ultra-broadband filter. The hexagonal structures look to be about $20 \mu\text{m}$ which would filter the larger wavelengths. The MESs would then filter the smaller wavelengths. The spatial interval between each prominence is estimated to be 170 nm and the diameter of every protrusion is around 100 nm which is fairly beneath the visible spectrum's wavelength [19].

Figure 2.32 depicts the replication of the moth-eye by producing a sphere

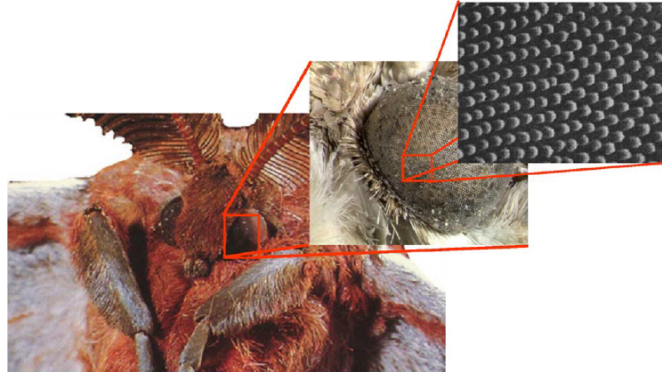


Figure 2.30: The sub-wavelength gratings of protuberances composed on the corneal surface of several insects are thought to yield anti-reflective characteristics with a broad bandwidth across the optical spectrum (from [14]).

with ARSs protruding on top of the sphere. The ARGs on top of the sphere has a height of 500 nm, a period of 400 nm, and a diameter of 200 nm; the spheres have an 8 μm height, a 25 μm period, and a 20 μm diameter [16]. From evaluating the figure, the filter is efficient across the entire spectrum with less than 10% reflectance. This is an absorbing filter that is not designed to transmit but only to keep the surface from reflecting by coating the filter with a metallic layer since metals are highly conductive. It can be seen in the figure that the sample is black which implies that light is not being reflected. Light

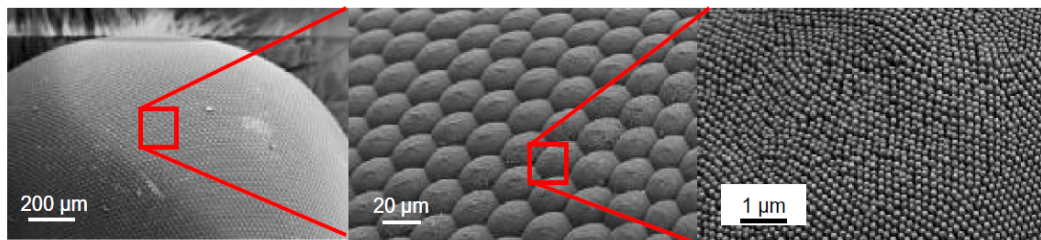


Figure 2.31: SEM images of (Left) a moth's eye, a night-active insect. (Middle) With modest magnification, the compound's eye hexagonal structure becomes plainly visible. (Right) With enhanced magnification, the corrugated surface of periodic sub-wavelength structures comes into view (from [19]).

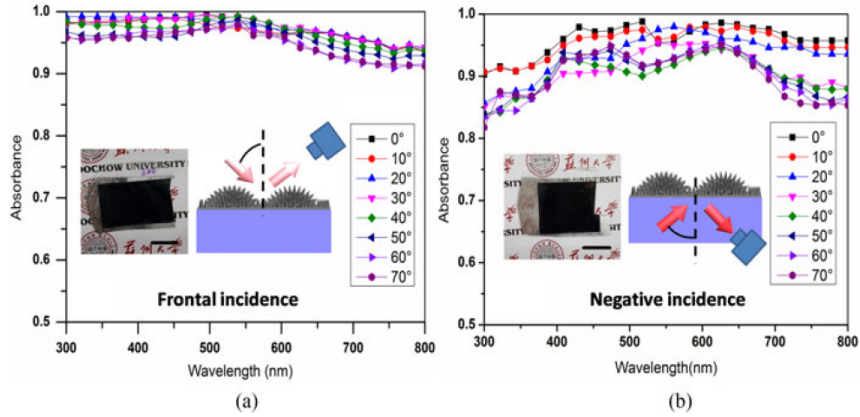


Figure 2.32: The implanted graphics and photos, a scale bar of 1 cm, display the example of a compound eye absorber with the optical arrangement employed for absorbance measurements, respectively. The compound eye absorber is under differing incidence angles for the absorption spectra considering the incident light orientations from (a) the overhead and (b) the underneath (from [16]).

typically sums up to be 100% of reflectance, absorbance, and transmittance, which produces $1 = T + A + R$ [27]. Unfortunately, the results for this design are not really telling of how well the structure itself is omnidirectional because the wavelengths are being absorbed, but absorbing filters are more likely to be omnidirectional. These filters produce remarkable AR surfaces and their results can be seen in [16], [27], and [40]. On a metal surface, the resonant oscillation of free electrons is known as surface plasmon and between the interface of the dielectric medium and a metal, this surface plasmon resonance phenomenon happens in reaction to an incident wave at a certain frequency of the electromagnetic wave; Amplified light absorbance suggests local surface plasmon resonance that is caused by the electric field in its chosen spectral region and the coupling of plasmon which is perceived on the surface of the noble metal [27].

Figure 2.33 illustrates absorption for the moth-eye replicated filter by the electric field intensity distribution and the Poynting vector (red arrows) giving

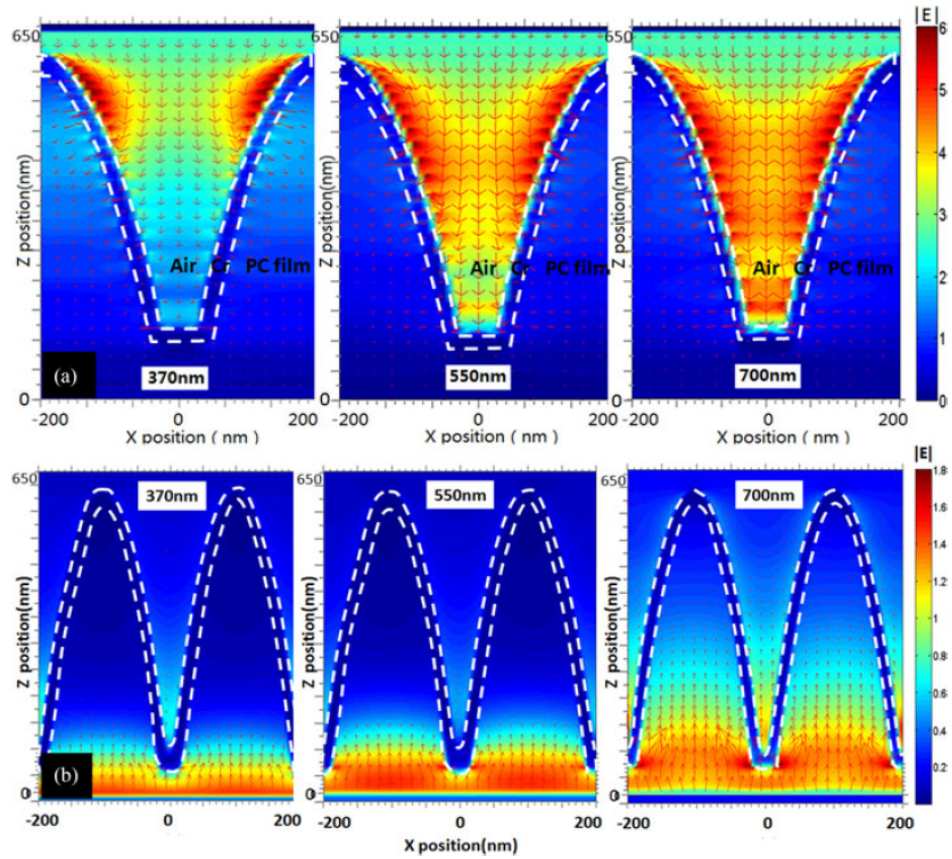


Figure 2.33: The simulated results of the Poynting vector in addition to the electric field intensity from TE polarization for the normal direction at positive and negative orientations, respectively. The white broken lines portray the contour of the Chrome (Cr) layer and the red arrows indicate the route of the Poynting vector (from [16]).

the direction in which the energy is propagating as well as the strength of the EMF. By examining figure 2.33(a), the normal incidence illumination at the positive direction for the wavelength of 370 nm displays the collection of the electromagnetic wave (EMW) at the peaks of the ARG producing plasmonic resonance causing the wavelength to be absorbed. A few Poynting vectors propagate through the metallic layer and into the absorber but unable to get to the bottom of the structure. The EMWs of 550 and 700 nm demonstrate increased plasmonic resonance between the ARSs and the confined electro-

magnetic radiation (EMR) gathers at the valley of the filter. The incident light's energy is confined between nano-structures since Poynting vectors are severing to manifest into vortices close to resonance locations and are ultimately absorbed [16]. Figure 2.33(b) depicts the electric field intensity distribution concentrating at the bottom of the structure due to the normal incidence radiation in the negative direction. Even as the wavelength increases, the electric field intensity increases, but the energy gradually decreases as it travels to the peak of the structure but seems to be incapable of doing so. The light at the wavelength of 700 nm can easily be seen escaping between the two neighboring MESs but appears to be minimal. The stronger the plasmonic resonance, the less energy will leak from the structure which is evident in figure 2.33(a) for the wavelength of 370 nm and figure 2.33(b) for the wavelength of 700 nm.

Figure 2.34 shows the results of numerical simulations of cylindrical pillars up to 85° . *TE* and *TM* polarizations have equal strength and are both incorporated in 45° polarization. Figure 2.34(a) shows the importance of choosing the correct dimensions for the fill factor for non-tapered SWGs. With the correct dimensions, these nano-pillars can still transmit up to 85% of the signal even at 85° . These non-tapered MESs are interference-based filters and this figure shows that these ARGs can transmit higher orders of diffraction with non-subwavelength dimensions. Light's transmittance direction will vary from the incident direction when $P \geq \lambda$, partly due to higher-order diffraction zeniths which consequently produces great transmittance [26]. Figure 2.34(b) illustrates how resonance affects the transmittance of the filter when the dimensions of the aspect ratio are being considered. Apart from the area of maximal transmittance ($\sim 87.7\%$ with $D = 70$ nm and $H = 350$ nm), a ripple pattern covering various values of the aspect ratio is discerned which is related

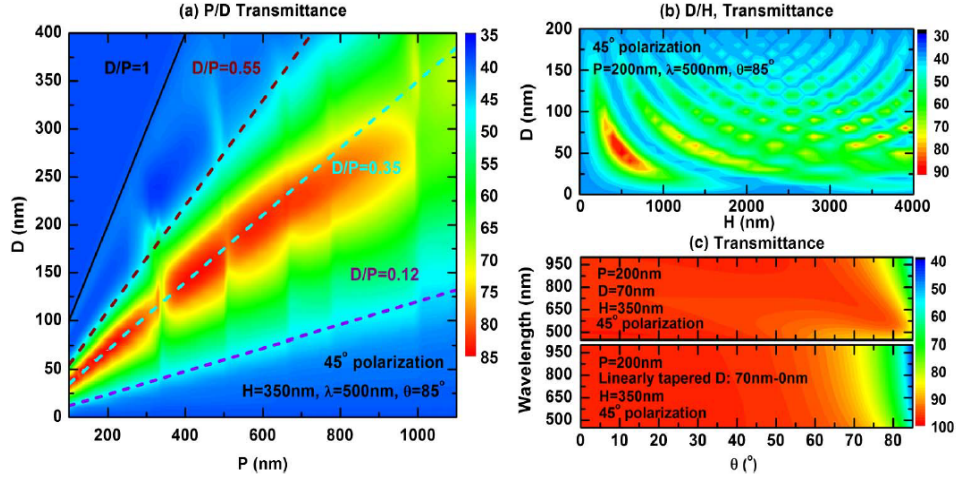


Figure 2.34: The hexagonal lattice structure’s dielectric value is $\epsilon_r = 1.46$ and its simulated transmittance spectra: (a) Contour map of transmittance with $\lambda = 500$ nm, under 45° polarization with $\theta = 85^\circ$, and $H = 350$ nm; (b) Contour map of transmittance with $\lambda = 500$ nm, under 45° polarization with $\theta = 85^\circ$, and $P = 200$ nm; (c) Comparing the spectra of transmittance between a cylindrical pillar structure having $D = 70$ nm and a “moth eye” structure linearly tapered having D tapered from 0 to 70 nm, both under 45° polarization, $H = 350$ nm, and $P = 200$ nm (from [26]).

to the Fabry–Perot interferences [26]. As the diameter and height increases, the number of resonance modes increases. Each of these modes has its own diminished local optimum transmittance region but the threshold to the variety of dimensions for the aspect ratio is a much more severe tolerance in comparison to the global optimum. The transmittance declines as the diameter increases regardless of the height since the porous surface is approaching to more of a flat surface seen by light. Figure 2.34(c) depicts the results from comparing the nano-pillars to a tapered MES. The omnidirectionality of tapered structures seems to be constantly compared to non-tapered structures with both filters having the same dimensions. Theoretically, non-tapered ARGs should be able to filter light effectively up to 89° but ineffectively at the incident angles close to the normal and inversely for tapered ARSs. The results for the tapered

ARSs could be further improved since the dimensions for this simulation were optimized for non-tapered ARGs, the tapered SWGs should not have a period. The nano-pillar and the nano-cone both filter above 90% up to the AOI of 60°. The nano-cone then starts to quickly abate after 60° while the nano-pillar is efficient up to about 75° and is even able to have transmittances above 80% for wavelengths of 500-575 nm. The wavelength dependency may be due to the fill factor, but as seen in figures **2.34(a and b)**, increasing the period will remove the dimensions of the filter from the global optimums that have the best performance. The cone decreases so drastically due to the tapered surface of the structure causing the light to glance off the cone instead of guiding the light towards the substrate.

2.3.4 Hybrid ARCs

Hybrid ARCs are referring to a filter that has both quarter-wave thin films and ARSs which can be seen in figure **2.35**. Due to the nano-structures being positioned in a low-loss layer, notable absorption will not occur in this layout [20]. The reason these hybrid ARCs are so effective might be due to the omnidirectionality the ARGs give to the filter since interference-based ARCs are less sufficient at oblique angles and the SWGs essentially guide the light to be always at normal incidence between the neighboring structures which quarter-wave thin films are most effective at perpendicular incidence. Less reflection may also have occurred if the thin film's had their RI raise towards the substrates in order to guide the propagating signal instead of alternating between higher and lower thin films. With the MESs having the effect of a gradient RI, non-porous thin films can be used allowing the filter to be more stable. The DLAR and multi-layer (4-layer) ARCs shown in the results of

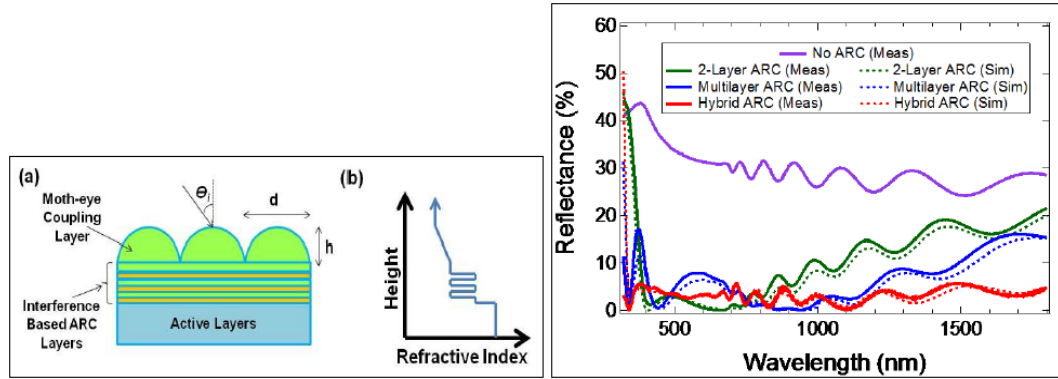


Figure 2.35: (a) The ARS has a period and height of 350 nm in the diagram showing the hybrid moth-eye model. (b) Height vs. the effective index of refraction for the entire anti-reflective structure. (Right) Each individual ARC is contrived to couple light into a multi-junction solar cell that has four junctions (4-J), the simulated and measured reflectance is displayed in the figure (from [20]).

figure **2.35** proves that hybrid ARCs are extremely effective over a spectrum with broad bandwidth and very low reflection. The interface between GaAs and InGaP is accountable for the interference fringes that start near 675 nm which the simulations considered, the InGaP layer thickness is connected to the period of these fringes, correlating to the band-gap of InGaP [20].

Figure **2.36** illustrates another hybrid ARC with ARGs on the first layer and last layer. Unfortunately, the SWGs are 1D so the filter will be sensitive to the polarization of the EMR which is displayed in figure **2.37** and figure **2.38**. The results could possibly be improved if the SWS in the bottom layer was a tapered structure that modeled the shape of a triangle. The EMWs would already have been captured and propagating towards this layer at a radiance being nearly at normal incidence, therefore an ARS with a conical shape would direct light more sufficiently towards the solar cell. Inserting SWGs within the filter would replace multi-layer thin films with a single layer if the device has a substrate with a very large RI. By observing the results shown in figure **2.37**

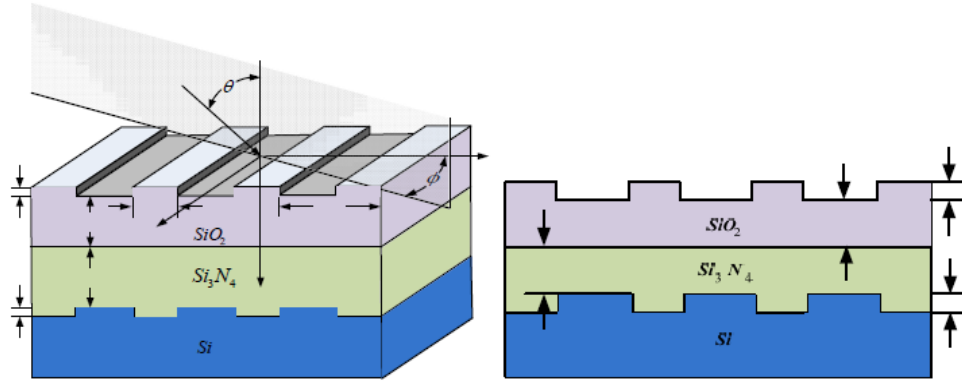


Figure 2.36: A solar cell's hybrid AR coating with multiple sub-wavelength grating layers. (Left) Anti-reflective structure's front view. (Right) Anti-reflective structure's side view (from [41]).

and figure 2.38, adding the second SWG layer within the filter evidently will solve the polarization sensitivity for 1D ARG layers. The figures show results for the silicon substrate with MESs etched on the surface and the silicon substrate with a SiO₂ layer also with SWSs etched on its surface with both filters having polarization sensitivities.

Figure 2.39 depicts what may be considered another hybrid ARC even though it was not referenced as so. This filter is considered to be a multiple-

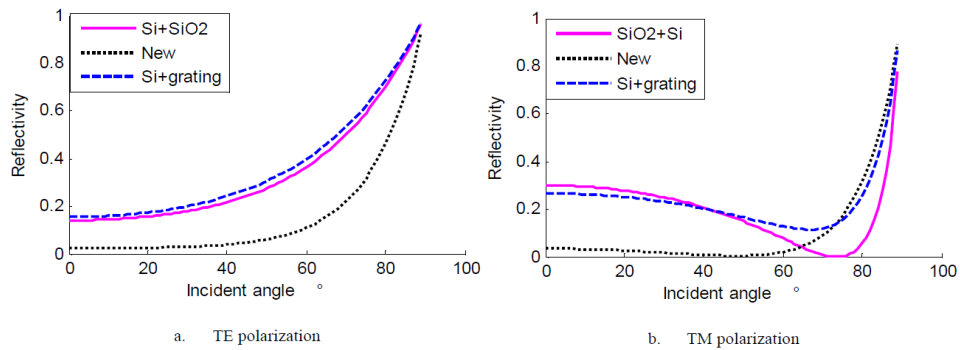


Figure 2.37: The SiO₂ anti-reflective coating layer, Silicon grating, and the new hybrid structure's calculated surface reflectivity vs omnidirectionality for (a) *TE* polarization in addition to (b) *TM* polarization (from [41]).

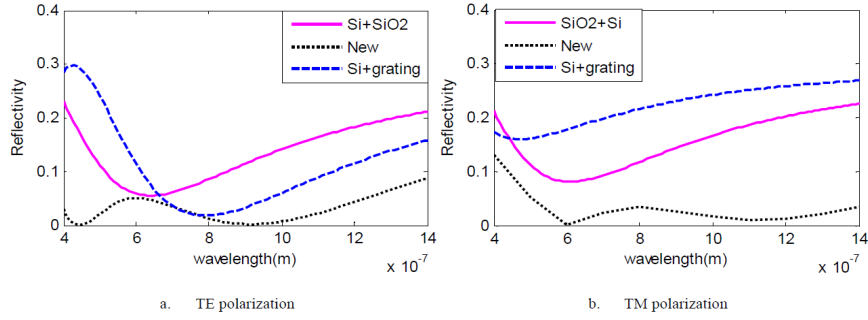


Figure 2.38: The SiO_2 anti-reflective coating layer, Silicon grating, and the new hybrid structure's calculated surface reflectivity as a function of wavelength for (a) TE polarization in addition to (b) TM polarization (from [41]).

discrete-layer thin-film design (4-Layers) using the methodology of oblique-angle e-beam deposition and physical vapor deposition (sputtering) to create porous thin films. The smallest wavelength being filtered is 350 nm and the height of the ambient layer is 262 nm. This ambient layer may be large enough to be considered an ARC of MESs which is why in figure 2.39, the results display the filter to be almost omnidirectional and filter such a wide spectrum of wavelengths due to the effective RI being so close to unity.

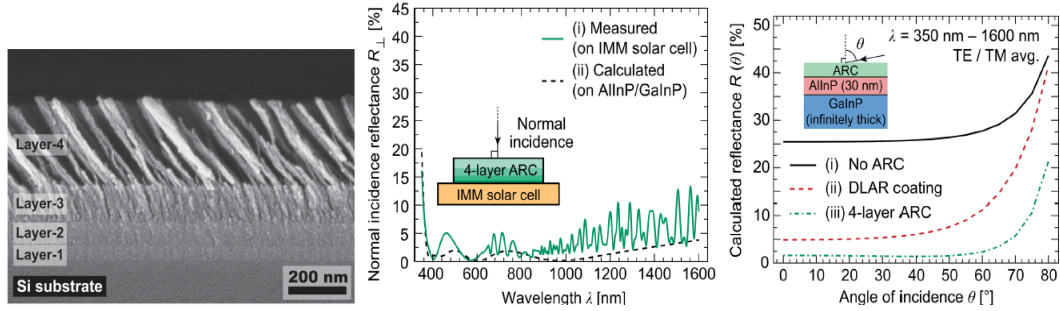


Figure 2.39: (Left) The four layer ARC's cross-sectional SEM picture, deposited on the substrate made of Si with: $n_4 = 1.11$, $n_3 = 1.32$, $n_2 = 1.79$, $n_1 = 2.38$, and $H_4 = 262$, $H_3 = 118$, $H_2 = 77$, $H_1 = 49$ nm. (Middle) The calculated and measured specular reflectance of the four layer ARC's R_{\perp} was attained by AlInP/GaInP (simplified design) of the inverted metamorphic (IMM) solar cell in addition to the IMM solar cell, respectively. (Right) The AlInP/GaInP design's calculated AOI vs wavelength with TE/TM averaged reflectance (from [18]).

2.4 Conclusion

Time was invested in the understanding of how quarter-wave thin films operate in order to further understand how sub-wavelength structured surfaces function. Destructive interference being the foundation of thin-film ARCs has been explained, revealing the importance of the angles of reflection and refraction. It has been shown that these two factors are still the basis of operation for anti-reflective surfaces using sub-wavelength structures. Effective Medium Theory should not be the cornerstone of modern models when designing sub-wavelength structured surfaces. Multiple internal reflections from neighboring structures with comparable dimensions to the wavelength spectrum of interest determines how to design the filter, which will be explained in the following chapter.

Chapter 3

Theory and Design Fundamentals for SWSs

Computer-aided design (CAD) tools analyze the electromagnetic behavior with numerical methods for computer simulations, today these tools are heavily relied upon to design and model selectively surface based filters (microwave filters). A considerable amount of the literature shows that the dimensions of these structures need to be below the desired wavelength spectrum being filtered due to the discovery from observing a moth's eye. With these CAD tools, it seems these filters are being designed by trial and error instead of rigorous mathematical and physics-based engineering principles. In [24], 289 full simulations were computed, the height and diameter were varied to optimize their filter. Other authors also allude to their plots for choosing the optimal dimensions of MESs in their simulated wavelength spectrums from most likely running hundreds of simulations. The aim of some of the previous research seemed to reveal the technology capable of fabricating nanostructures with the smallest dimensions possible with certain fabrication methods and equipment, very few of the papers instructed how to design these filters but they all mentioned that the height and period of the ARGs greatly affected the results. The iterative designed algorithm in [14], genetic algorithm [18], and a particle swarm algorithm in [40] were used in designing the SWGs. They also agreed

that those dimensions are key to reduce reflections from a surface.

In this chapter, the equations needed for designing an AR surface with ARSs and the theory behind them for tapered and non-tapered structures will be discussed. Much discussion has taken place in the literature on the topic of which structures are more omnidirectional, tapered or non-tapered. The conclusions to this topic and more should have already been known in advance. EMT is correct, but this theory does not entirely describe how this type of device is filtering a desired wavelength spectrum. EMT was explained earlier and demonstrated in figure **2.14**. The conclusion here is the same as the conclusion found in section **2.2** (thin film filtering fundamentals), the refractive angle determined by Snell's Law (**2.1**) also applies to this type of filter. The refractive angle θ_2 depicted in figure **2.12** can be found if the RI of n_1 and n_2 are known along with the incident angle θ_1 .

Considering EMT is based on the filling factor volume, the dimensions of the ARG can be difficult to accurately determine. A paraboloidal-shaped ARS that is tapered with the base of the structure attached to its neighbors, Snell's Law can be applied here to reveal the path the light will follow when its illumination falls upon these SWGs which was displayed in figure **2.1(c)**. Since the rays are not refracting inside the structures, the angle of the illumination is at a grazing angle leading to internal reflections guiding the light towards the substrate. This is why at normal incidence, the tapered structures act like GRIN thin films and non-tapered structures act as a single layer thin film ARC. With the understanding of optical phenomena (brief explanations of the basics of optics are in section **1.3.2**), these filter's behavior can be explained. This also explains why the conical structures are more effective at perpendicular incidence and pillars are less adequate. Inversely, pillars are effective at oblique angles and

conical structures are not adequate. This is why parabolical structures are in between these two ranges concerning omnidirectionality. Snell's Law also explains why tapered and non-tapered structures can not be compared directly with the same dimensions. Tapered structures with a larger period are much less effective at normal incidence. The shape of the structure should only be chosen with the interest of choosing a section of the sector to filter pertaining to the AOIs.

3.1 Design Equations For Tapered Structures

SWSs are hardly referred to as bandpass filters in any of the literature but this is how they behave. A bandpass filter has two cutoff frequencies which denote the beginning and end of the wavelength spectrum being filtered which is known as the bandwidth. The height of the periodic array structure determines the first cutoff frequency at the lower frequency f_1 and the pitch dictates the end of the spectrum at the higher frequency f_2 . Explanations of the forthcoming equations will guide how to construct an AR surface using MESs.

More optical phenomenons revolve around the period, the explanation regarding the cutoff frequency f_2 will be explained first due to its complexity. With tapered structures, the period is the pitch/diameter with these filters, the base being connected to its neighbors induces optimal filtering. Tapered SWSs prevent higher orders of diffraction from occurring during the filtering process. ARGs are not as productive, in this circumstance, since gratings don't accommodate to higher diffraction orders which evidently provide to the overall energy harvest in the solar cell, and gratings principally assist in directly reflecting and transmitting light (propagating the zeroth diffraction order) [4]. Another factor that helps is the wide known fact about the dimensions

of MESs. For zero-order diffraction [29], the structure’s period is normally substantially shorter than the wavelength of light to avert scattering [36]. Scattering has the potential to cause constructive and destructive interference from the many wavelengths of light landing on the surface of the SWG with each wavelength splitting into many individual wavelengths all heading into different directions leading to higher orders of diffraction. This was explained graphically in figure 2.9 and the results from [12], [13], [20]. The scattering that does occur with ARSs, having dimensions smaller than the wavelength of interest, has been considered negligible according to [4], [14], [18], [20], but absolute zero reflectance will not likely be obtained because of scattering [14].

$$\Lambda \leq \frac{\lambda_S}{n_i + n_s} \quad (3.1a)$$

$$\Lambda \leq \frac{\lambda_S}{n_s} \quad (3.1b)$$

In this thesis, the only concern is how the filter operates under perpendicular incidence, but the period can be found with exact oblique AOIs in [12]–[14]. For any arbitrary angle of incidence, the constraint for the period is given by (3.1a) from [12], [13] and a more stringent condition is $\Lambda \leq \lambda_S/2n_s$ [27], [34], assuming the incident medium is not greater than the substrate. The condition for the period under normal incidence is (3.1b) from [4], [12], [13], [25]. Λ – period and pitch for tapered structures to achieve optimal filtering, λ_S – shortest wavelength of the spectrum being filtered in a vacuum, n_i – refractive index of the incident medium, and n_s – refractive index of the substrate.

When gratings have dimensions smaller than the wavelength of light ($\Lambda < \lambda$), this is sometimes referred to as an unresolvable structure as far as the light is

concerned. Repressing all diffraction orders exceeding the zero-th order is the efficacy of an unresolvable grating which decreases the elements of reflection and transmission of the light to solely specular properties; permitting light to propagate as throughout a continuous media with a graded refractive index as throughout the SWG determined by the proximate structure profiles [34]. EMT is commonly applied to these SWSs because the RI can be expressed as a function of the width and height, in other words, how much of the material remains which determines the volume. Since the ARG is tapered, the RI can be considered a graded function from the change in the RI starting at the incident media to the substrate material dependent upon the profile of the MESs which is also shown in figure 1.2.

The reason the pitch/diameter determines the second cutoff frequency is due to the phenomenon known as resonance. Fabry-Perot interference arises out of multiple reflections within the structure [44] and is referred to as resonance that is constructive interference in [45]. When wavelengths that are smaller than the length of the pitch interact with the ARS, this leads to multiple internal reflections inside the SWS which causes resonance which then leads to reflection making the surface no longer AR.

$$c = \lambda \cdot f \tag{3.2a}$$

$$n = \frac{c}{v} \tag{3.2b}$$

$$v = \lambda \cdot f \tag{3.2c}$$

$$n = \frac{c}{\lambda \cdot f} \tag{3.2d}$$

$$f = \frac{c}{\lambda \cdot n} \quad (3.2e)$$

The cutoff frequency can be found from the following equations above. Equation **(3.2a)** is from [46] and is the speed of light in free space which has the value of 2.998×10^8 m/ s in a vacuum. The index of refraction, from [47], is how fast light travels in a medium described by **(3.2b)** and was discussed earlier in the basics of optics section **1.3.2**. The velocity of light in a medium is defined by **(3.2c)** and is from [46]. By substituting **(3.2c)** into **(3.2b)**, equation **(3.2d)** is formed. By manipulating **(3.2d)** to solve for f , the cutoff frequency at perpendicular incidence is defined in **(3.2e)**. f - the number of cycles in a periodic wave measured in a single second, λ - the length of a single period in a periodic wave. A similar approach was found in [4].

$$f_1 \sim \frac{c}{H \cdot n_s} \quad (3.3a)$$

$$f_2 \sim \frac{c}{\Lambda \cdot n_s} \quad (3.3b)$$

The equations for the cutoff frequencies were derived from **(3.2e)** and are listed above. For tapered structures, the period is the pitch. Therefore $\lambda = \lambda_S = \Lambda$ which is due to resonance causing the end of the spectrum giving **(3.3b)**. It was mentioned earlier that the height/depth of the structure determined the first cutoff frequency, when the height of the MES is the length of the wavelength or greater, the wavelength can be effectively guided towards the substrate $\lambda = \lambda_L = H$ providing **(3.3a)**. λ_L - longest wavelength of the spectrum being filtered in a vacuum, H - the height of the structure, and $c \sim v$ for air since its value is so close to the speed of light in a vacuum.

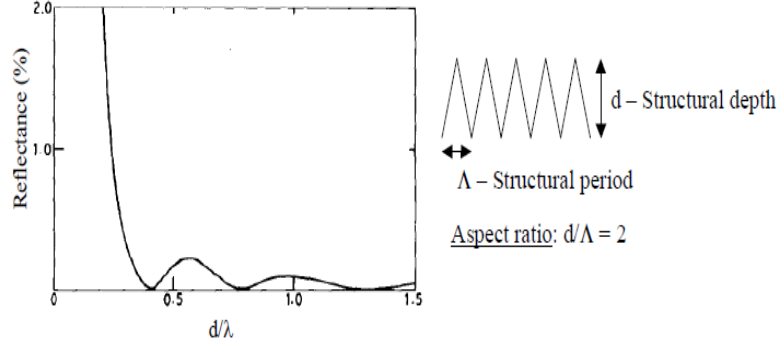


Figure 3.1: (Left) The reflectance dependence for d/λ . The first minimum the reflectance decreases to is $d/\lambda = 0.4$. The reflectance is virtually zero for $d \gg \lambda$ (from [12]). (Right) SWG parameters (from [13]).

The height of the structure is typically limited by the fabrication method used to create these filters. Generally, an aspect ratio of 2 was considered to be producible and mechanically stable by most methods. Fabrication methods that were able to obtain enormous depths for the ARG were mentioned in [27], which is a perfect absorber with an aspect ratio of 14 and in [28], the aspect ratio was 8 on a silicon wafer. If the technology available does not produce a great enough depth to filter a chosen broad range of wavelengths in the electromagnetic spectrum, then it has been found in [13], [29], [34] that the height of the structure can be $H = 0.4 \times \lambda_L$. The dependence of the reflectance from the aspect ratio is illustrated in figure 3.1.

$$AR = \frac{H}{\Lambda} > 0.4 \quad (3.4a)$$

$$O = \frac{f_2}{f_1} > 1 \quad (3.4b)$$

The greater the aspect ratio, (3.4a) from [4], [5], [11], [13], [34], the

more broadband the filter becomes. The ARSs will start to efficiently filter when the height of the structure is 0.4 times greater than the length of the pitch, which is demonstrated in figure 3.1. Any filter, in this instance an AR surface of MESs, is considered broadband when it filters more than one octave; (3.4b) from [12], [13], is a ratio of the highest frequency to the lowest frequency, determining the number of octaves, as long as the results of reflection are lower than the reference value.

It should be noted that (3.3a) is not accurate for less “dense” or more transparent materials. This may be a result of the light falling upon the ARGs at normal incidence and depending on how tapered the SWG is, as far as light is concerned, the ARS is not transparent due to the grazing angles. Equation (3.3a) is accurate for silicon because its RI value is very high and (3.3b) is valid for all materials because grazing angles are not involved. For more transparent materials, (3.3a) can be used with a high RI value such as silicon to accurately capture the cutoff frequency, and then (3.3b) can be calculated with the actual transparent RI value to find the correct bandwidth. An example of a filter using an AR surface of SWSs is displayed in figure 3.2.

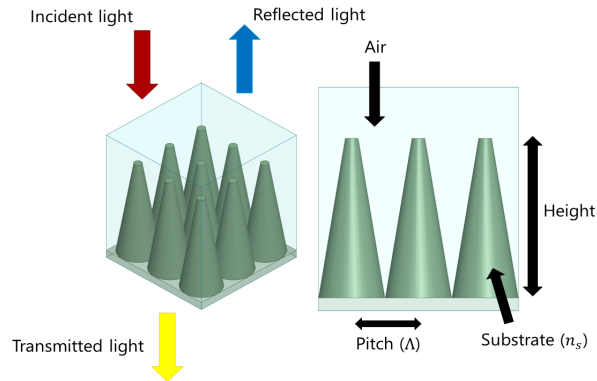


Figure 3.2: The diagram illustrating the filtering of light and the layout parameters; the cross-sectional perspective of the preferred moth-eye conical structures with parameters.

3.2 Design Equations For Non-Tapered Structures

Non-tapered MESs are interference-based structures which can be seen in figure **2.34**. The same design concepts that formed the formulas for the cutoff frequencies in the previous section may be applied in this section also. The question that needs to be answered is how can the interference that occurs with these ARGs be predicted and taken advantage of to filter a selected wavelength spectrum. By investigating figure **2.34** and figure **2.7**, the answer can be found.

Figure **2.7** is optimized at normal incidence and the dimensions chosen include the results at oblique angles. Notice in figure **2.7(b)** that at a height a quarter of the wavelength at normal incidence, the highest transmittance is achieved. When the height is increased to the wavelength being evaluated, the oscillations increase. Figure **2.7(a)** confirms the height is effective at various angles. The diameter is $1/10$ of the wavelength at normal incidence which gives the highest transmittance in figure **2.7(d)** and is more omnidirectional in figure **2.7(c)**.

Figure **2.34** is optimized for oblique incidence and the dimensions are chosen specifically for this region since normal incidence only causes $\sim 4\%$ reflection loss with a substrate that has a value of $n = 1.46$. Figure **2.34(a)** shows that non-tapered SWGs can transmit higher orders of diffraction. When the period is $\gtrsim \lambda$, the pathway of the transmitted light will consequently diverge from the incident route, and the appreciable transmittance will arise partly from higher-order diffraction optimums [26]. Just like with tapered ARS, figure **2.34(b)** shows that the height of the structure needs to be at the wavelength being evaluated and also that the diameter is $1/10$ the wavelength again. This leads me to believe that if figure **2.34(a)** was evaluated with the

dimensions mentioned in the previous sentence, the SWS would be in the high transmittance region.

For both these simulations, the period was chosen to be 200 nm but for two different wavelengths. In [26], the period was chosen to be smaller than the wavelength being evaluated in order to keep higher orders of diffraction from occurring and to transmit the most amount of light. For [38], the period was chosen strictly at normal incidence but also is smaller than the wavelength being evaluated. Both of these research papers included that the period was determined by EMT. The period should be decided by the refractive angle, the following formulas for the cutoff frequencies were developed with simulations to discover the optimal period.

Since these structures are interference-based, the quarter-wave thin-film architecture may be able to be applied in this circumstance. Evidence with the height being a quarter of the wavelength has already been seen at normal incidence and since both research papers found the pitch to be 1/10 of the wavelength to be optimal, my simulations began with these parameters. The pitch determined the range of the filtering spectrum just as with tapered structures and the height of the structure decided the number of oscillations that occurred within the filtering range.

The period filters the wavelengths just as much as the non-tapered structure itself. With the period being so large in all of the literature that demonstrated non-tapered ARGs, this shortened the optimal filtering bandwidth due to resonances occurring between the neighboring SWGs. In order to take advantage of the entire available filtering range, the period needs to be relatively short. It was found that having the period shorter also forced the minima that occurs from destructive interference to be more effective. The optimal period was

found to be 1/10 the pitch. A similar rule is suggested in [48] and a comparable design scheme for non-tapered structures in [25]. The interval between the neighboring structures is the interspace (I) and the period can be found with the pitch, $p = I + \Lambda$, this adjusts the interspace which filters the light.

$$\Lambda = \frac{1}{10} \cdot \lambda \quad (3.5a)$$

$$I = \frac{1}{10} \cdot \Lambda \quad (3.5b)$$

$$H = \frac{1}{4} \cdot \lambda \quad (3.5c)$$

$$\Lambda_{eff} = \frac{\lambda}{n_i + n_s} \quad (3.5d)$$

In the previous section, the pitch and the period were the same. Here the pitch will be **(3.5a)**, the interspace will be **(3.5b)**, and the height will be **(3.5c)**. The first cutoff frequency begins with **(3.5d)** and is derived from **(3.1a)**. For non-tapered structures, due to interference from reflections and refractions, the option of **(3.1b)** for perpendicular incidence is removed. Since these filters are interference-based, this means there is a minima and the results asymptotically approach the reference value (no filter used on wavelength spectrum) but should never exceed it just as a quarter-wave film's response would behave. Since the period and the pitch determines the passband, the interspace between the structures causes interference. It must be this interference provoking an effective period seen by light for the need of Λ_{eff} for determining f_1 .

$$f_n \sim \frac{c}{\Lambda \cdot n_s} \quad (3.6)$$

Since the depth primarily controls destructive interference, the pitch and period basically decides both cutoff frequencies. Equation (3.6) is derived from (3.3b) and was explained in the previous section.

$$f_1 \sim \frac{c}{(2 \cdot \Lambda_{eff} + 3 \cdot I) \cdot n_s} \quad (3.7a)$$

$$f_{min} \sim f_1 \cdot (2 \cdot m + 1) \text{ for } m = 0, 1, 2, \dots \quad (3.7b)$$

$$f_{max} \sim f_1 \cdot (2 \cdot m) \text{ for } m = 0, 1, 2, \dots \quad (3.7c)$$

$$f_2 \sim \frac{c}{(\Lambda + 2 \cdot I) \cdot n_s} \quad (3.7d)$$

Just as in the previous section, the pitch determines the second cutoff frequency f_2 . For non-tapered structures, there is a period giving the value of the distance each neighboring structure must distance itself from the rest of the structures. Therefore, the interspace helps filter the light along with the structure and must be included in the equation. The second cutoff frequency is obtained with (3.7d), the single unit filtering the light is the pitch, and both interspaces next to the structure. The first minimum in the passband within the bandwidth is found with (3.7a), which describes the larger unit for filtering, cutoff frequency f_1 . To effectively capture the light, two ARSs and the interspaces beside the structures, as well as between them are needed. The first minimum is acquired with (3.7b) and the first maximum can be located with (3.7c). The other bandpass filters in the passband up to f_2 may be found with (3.7b). The many maximums in the bandwidth may be located with (3.7c).

It should be noted that (3.7b) and (3.7c) are less accurate for substrates with a higher RI. More severe interference and resonance occur for these substrates, causing the formulas to be less precise. Even for non-tapered structures, using (3.4b) is still accurate for this type of filter. Lastly, if the refractive index of a material is unknown, then the index of refraction can be found with the dielectric constant or relative permittivity ϵ_r by using (3.8a) [47]. A more common parameter for determining broadbandness is finding the bandwidth B by implementing (3.8b) [47]. An example of a filter using an AR surface of non-tapered MESs is shown in figure 3.3.

$$n = \sqrt{\epsilon_r} \quad (3.8a)$$

$$B = f_2 - f_1 \quad (3.8b)$$

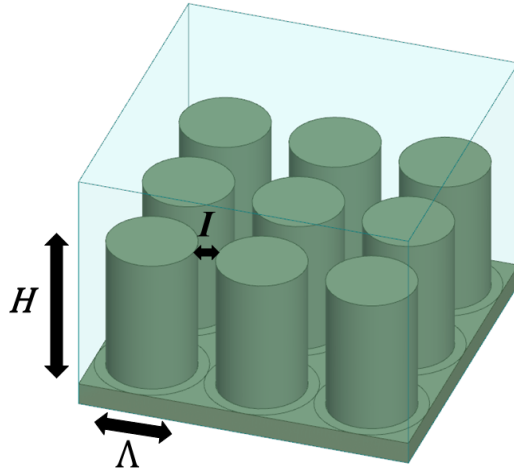


Figure 3.3: Graphic of a quartz substrate with a dielectric square lattice structure with simulation configurations including: pitch (Λ), interspace (I), and height (H).

3.3 Conclusion

Since the angles of reflection and refraction are the basis of operation for a surface that filters a wavelength spectrum, this leads to two categories for anti-reflective surfaces using sub-wavelength structures: tapered and non-tapered sub-wavelength structures. The theory for designing filters for both of these methods and their derivations of the equations with fundamentally known formulas is explained. Guidelines are also introduced to help meet certain specifications if needed. In the following chapter, examples of filters implementing my methodology of design for anti-reflective surfaces employing sub-wavelength structures.

Chapter 4

Bandpass Filters Using SWS Surfaces

High-frequency structure simulator (HFSS) is a full-wave electromagnetic field simulator for modeling any random volumetric 3D geometry. Ansoft HFSS utilizes the finite element method (FEM) to solve Maxwell's equations and adaptive tetrahedron meshing to compute parameters. These parameters include resonant frequency, fields, and S-parameters [49].

EMT produces closed-form approximations to provide effective dielectric constants in response to the AR structure's profile. EMT is effective when the period of the structure is much smaller than the wavelength of the radiation; as the period approaches the resonance regime, EMT becomes invalid for periods that are only slightly smaller than the specified wavelength [14]. It is noted that EMT may not be able to be described with an analytical closed-form when evaluating EMWs in every direction [26]. EMT is not as advantageous as the rigorous coupled-wave analysis (RCWA) method since the dimensions of the structure are foreseen more accurately which yields better results for optimization [4], this also happens to be true for the finite-difference time-domain (FDTD) method as well.

The RCWA method is able to deliver precise results for any AR structure's profile and period length, this is possible from taking advantage of Maxwell's

equations in addition to the transfer matrix method (TMM) typically [14]. The TMM requires matching the tangential elements of both magnetic and electric fields forming a characteristic matrix [39]. The transmission and reflectance can then be determined with this strategy with varying incident angles [34] but the AR structures need to have periodicity with the RCWA method unlike with the FDTD method [36]. The FDTD method also employs time-dependent Maxwell equations [16] for the calculation of reflection losses from AR structures in differing incident angles [42].

These types of CAD software are sought after due to the moth's eye to simulate these structures which are a type of bio-mimicry. Mammals have lensed eyes instead of compound eyes which are comprised of numerous optical components known as ommatidia; these eyes are especially remarkable at a practically unlimited depth of field, large field of view, and great perception of motion [37]. These structures can be designed to be absorbers for radar stealth [16], surface engineering from the superhydrophobic lotus leaf, and swimwear that reduces drag from shark's riblet structures [27].

The following designs are considered filters since their purpose is selecting a bandwidth from the wavelength spectrum and transmitting these selected wavelengths. There are numerous operations with the primary concern of having the zeroth diffraction order transmit, the data is lost otherwise if higher orders of diffraction occur [13]. For example, the transference of data is directly linked to THz spectroscopy and imaging [12]. Sometimes ARC's are not designed with the concern of transmitting the wavelengths but to merely keep the surface from being reflective.

4.1 Tapered SWSs for a Bandpass Filter

The following filter has been fabricated on silicon but not on quartz yet. For this reason, the discussion will begin with the substrate simulated with quartz and finish with the fabricated results compared to the simulated for the silicon filter. An AR surface designed to filter a frequency spectrum from $f_1 \sim 0.400$ THz to $f_2 \sim 1.140$ THz is desired.

The frequency spectrum from 3 mm to 30 μm or 0.1 to 10 THz (1 THz = 10^{12} Hz) is commonly known as the THz spectral range [13] which is an incredibly extensive bandwidth [12] that has similar characteristics to microwave and infrared radiation since it is located in between them in the electromagnetic spectrum [15]. This EMR can transfer a substantial amount of data comparably to infrared radiation while also being able to effortlessly pierce ceramics, wood, and plastics; this indicates the capability for utilizing this technology in areas such as pharmaceutical drug characterization, safety inspection, and spectroscopic imaging [15].

The wavelength that determines the dimensions is the same as the cutoff wavelengths. Since the cutoff frequencies are known, (3.3a) and (3.3b) will need to be modified to find the dimensions of the ARS:

$$f_1 \sim \frac{c}{H \cdot n_s} \implies$$

$$H \sim \frac{c}{f_1 \cdot n_s} \quad (4.1a)$$

$$f_2 \sim \frac{c}{\Lambda \cdot n_s} \implies$$

$$\Lambda \sim \frac{c}{f_2 \cdot n_s} \quad (4.1b)$$

Unfortunately, f_1 would not be accurate if the pitch was given instead of the cutoff frequencies for low RI materials, which was explained at the end of section **3.1**. Due to this, a reference value needs to be chosen to receive consistent calculations. The materials with some of the highest naturally occurring refractive indices are germanium ($n = 4$) and titanium dioxide ($n = 10$) and these values were specified in [47]. Germanium was chosen as the reference value because the calculations were closer to the minimums within the bandwidth of the spectrum. Therefore, **(3.3a)** needs to be modified to find the desired cutoff frequency for a filter:

$$f_{1_{eff}} \sim \frac{c}{H \cdot 4} \quad (4.2a)$$

$$H \sim \frac{c}{f_{1_{eff}} \cdot 4} \quad (4.2b)$$

The effective cutoff frequency **(4.2a)** will now be used as a standard for consistency, even for bandpass filters with a high RI, unless the RI is above 4. Every RI value above germanium's might be accurate enough to no longer need a standard, **(3.3a)** and **(4.1a)** may then be implemented. Now **(4.1b)** and **(4.2b)** can be calculated.

$$H \sim \frac{c}{f_{1_{eff}} \cdot 4} \implies H \sim \frac{3 \times 10^8}{400 \times 10^9 \cdot 4} \implies H \sim 188 \mu\text{m}$$

$$\Lambda \sim \frac{c}{f_2 \cdot n_s} \implies \Lambda \sim \frac{3 \times 10^8}{1.140 \times 10^{12} \cdot 1.5} \implies \Lambda \sim 175 \mu\text{m}$$

The guideline thresholds to check the dimensions of the SWG are calculated with **(3.1b)** and **(3.4a)**. Then the broadbandedness can be computed with **(3.4b)** and **(3.8b)**. Convert frequency to wavelength with **(3.2a)**.

$$c = \lambda \cdot f \implies \lambda = \frac{c}{f} \implies \lambda = \Lambda_S \text{ (which is } f_2) \implies$$

$$\Lambda_S = \frac{3 \times 10^8}{1.14 \times 10^{12}} \implies \Lambda_S = 263.16 \mu\text{m}$$

$$\Lambda \leq \frac{\Lambda_S}{n_s} \implies \Lambda \leq \frac{263.16 \times 10^{-6}}{1.5} \implies \Lambda \text{ (175 } \mu\text{m)} \leq 175.44 \mu\text{m}$$

$$AR = \frac{H}{\Lambda} > 0.4 \implies AR = \frac{188 \mu\text{m}}{175 \mu\text{m}} \implies AR = 1.07 > 0.4$$

$$O = \frac{f_2}{f_1} > 1 \implies O = \frac{1.140 \text{ THz}}{0.400 \text{ THz}} \implies O = 2.85$$

$$B = f_2 - f_1 \implies B = 1.140 \text{ THz} - 0.400 \text{ THz} \implies B = 740 \text{ GHz}$$

The parameters including informative data and important for modeling a tapered ARG on quartz are listed in table 4.1. Figure 4.1 illustrates the AR surface of the designed profile for the MES. The simulated results of this coating are displayed in figure 4.2. By observing the results, the calculations are close to the simulated data points. The simulated cutoff frequency marker's values

Table 4.1:
AR Surface of Tapered SWS Filter Design Parameters for Quartz

Property		Value
Substrate's RI	n_s	1.5
Cutoff frequency	f_1	0.400 THz
Cutoff frequency	f_2	1.140 THz
Pitch	Λ	175 μm
Height	H	188 μm
Aspect Ratio	AR	1.07
Octaves	O	2.85
Bandwidth	B	740 GHz

are determined by the minima and maxima within the bandwidth. Notice that the reference value is at 4% reflectance at normal incidence. Materials that have a RI near $n = 1.5$ reflects entirely (100%) at grazing angles, but for perpendicular incidence, approximately 4% reflectance [4]. Since the pitch is so close to the outcome from the guideline inequality, f_2 is very close to the resonance regime. The spikes in reflectance after f_2 are caused by wavelengths that are shorter than the pitch. These wavelengths interfere with each other producing constructive interference, this was discussed in section 3.1.

The following filter was fabricated in silicon. Since the dimensions are known, the process mentioned in section 3.1 can be employed. The initial step is to begin with (3.3b), the refractive index of silicon is $n_s \sim 3.45$. Since the substrate is still less than $n = 4$, (4.2a) will be used instead of (3.3a).

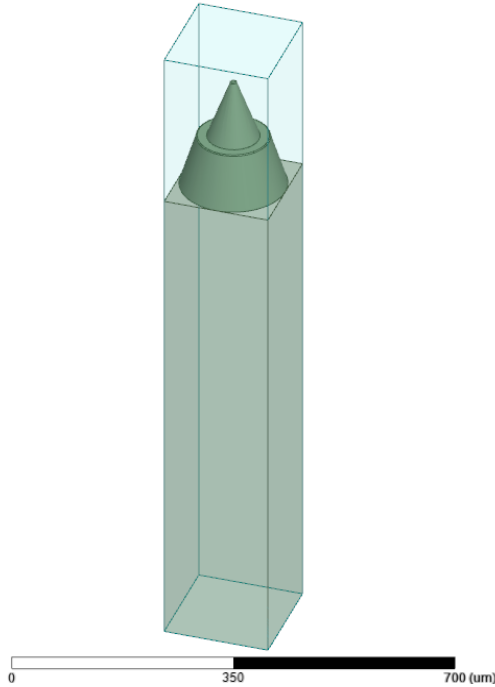


Figure 4.1: HFSS model of a multi-level micro-cone AR surface having a height $H = 188 \mu\text{m}$ and pitch $\Lambda = 175 \mu\text{m}$ on a quartz substrate having a thickness of $800 \mu\text{m}$.

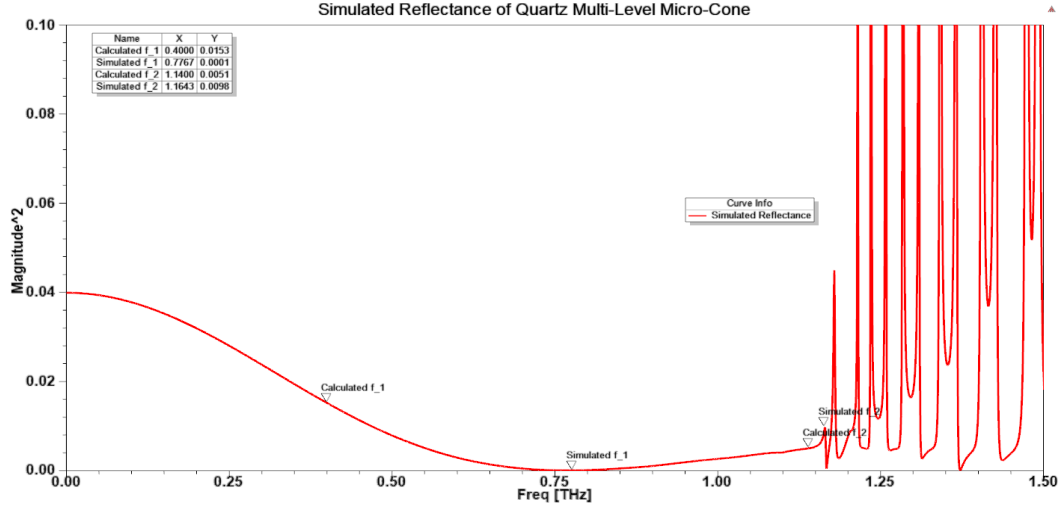


Figure 4.2: The magnitude² reflectance of the scattering parameters S_{11} for the quartz multi-level micro-cone AR surface at perpendicular incidence.

$$f_{1_{eff}} \sim \frac{c}{H \cdot 4} \implies f_{1_{eff}} \sim \frac{3 \times 10^8}{188 \times 10^{-6} \cdot 4} \implies f_{1_{eff}} \sim 400 \text{ GHz}$$

$$f_2 \sim \frac{c}{\Lambda \cdot n_s} \implies f_2 \sim \frac{3 \times 10^8}{175 \times 10^{-6} \cdot 3.45} \implies f_2 \sim 497 \text{ GHz}$$

$$O = \frac{f_2}{f_1} > 1 \implies O = \frac{497 \text{ GHz}}{400 \text{ GHz}} \implies O = 1.2425$$

$$B = f_2 - f_1 \implies B = 497 \text{ GHz} - 400 \text{ GHz} \implies B = 97 \text{ GHz}$$

Table 4.2:
AR Surface of Tapered SWS Filter Design Parameters for Silicon

Property		Value
Substrate's RI	n_s	3.45
Cutoff frequency	f_1	400 GHz
Cutoff frequency	f_2	497 GHz
Pitch	Λ	175 μm
Height	H	188 μm
Aspect Ratio	AR	1.07
Octaves	O	1.2425
Bandwidth	B	97 GHz

The parameters encompassing valued data and significant for modeling a tapered ARS on silicon are listed in table 4.2. Figure 4.3 illustrates the AR surface of the designed profile for the SWG. The simulated results of this coating are displayed in figure 4.4. Comparing table 4.1 and table 4.2, just by changing the RI, the broadbandness of the silicon filter is a little less than half as broadband as the glass filter which is noticeable in (3.3b).

The calculations are fairly close to the simulated values by observing figure 4.3. With higher RI values, the calculations are expected to farther from the simulated, most likely caused by severe interference. Notice that the reference value is close to 30% reflectance at normal incidence. At perpendicular incidence, 30% of the EMR is reflected owing to the high RI of silicon having

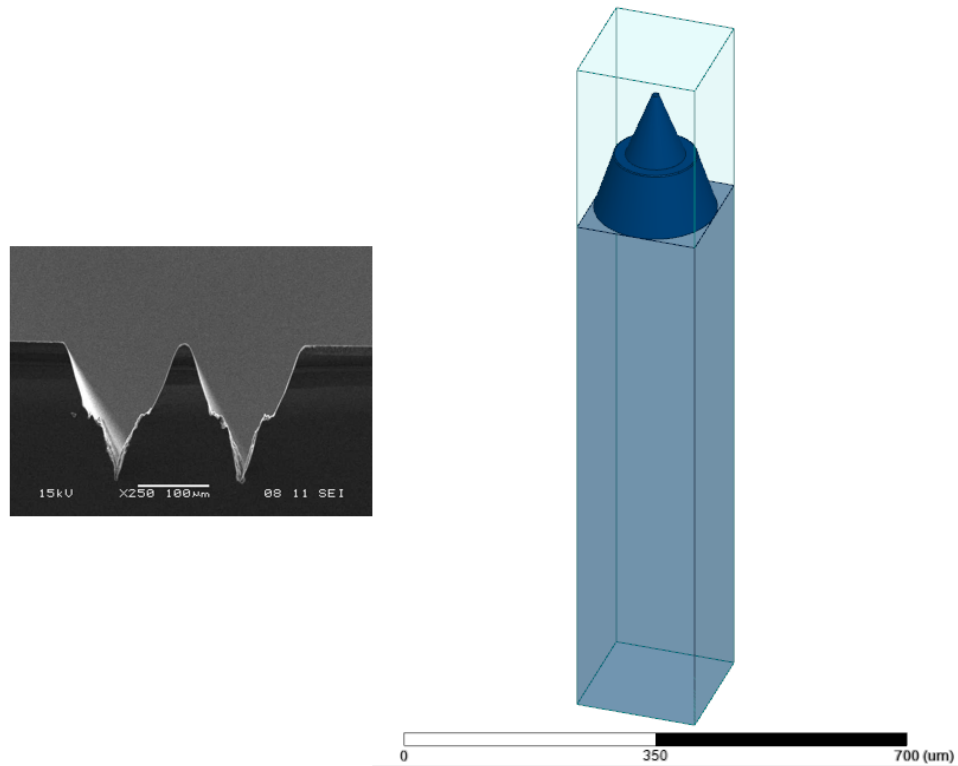


Figure 4.3: (Left) SEM image of the fabricated filter. (Right) HFSS model of the fabricated filter which is a multi-level micro-cone AR surface having a height $H = 188 \mu\text{m}$ and pitch $\Lambda = 175 \mu\text{m}$ on a silicon substrate having a thickness of $800 \mu\text{m}$.

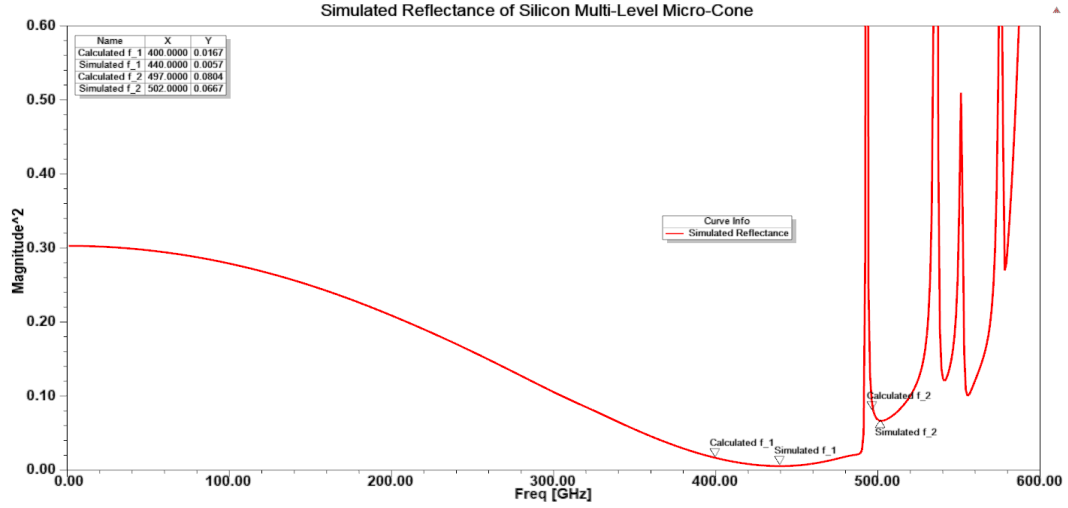


Figure 4.4: The magnitude² reflectance of the scattering parameters S_{11} for the silicon multi-level micro-cone AR surface at perpendicular incidence.

$n = 3.42$ [12]. For high RI materials, the pitch needs to be less than the guideline inequality product to be safely within the bandwidth without including peaks of reflectance. The simulated minimum practically reached zero reflectance even with a material with such a high RI.

4.2 Measured Results for Tapered SWSs

The simulated and measured data for bare silicon sample are displayed in figure 4.5. HFSS is the simulation tool used to model the bare Si substrate and the multi-level tapered structures. The reflectance seems to be accurate when compared to the simulated data. It is known for a silicon substrate, that the reflectance, when including reflection from the bottom surface, is around 45° . The simulated results are close to the measured results except for the multiphonon absorbance. The absorption seen around 18 THz is due to the multiphonon bands. It is known for silicon that this is most likely due to the carbon impurity [50].

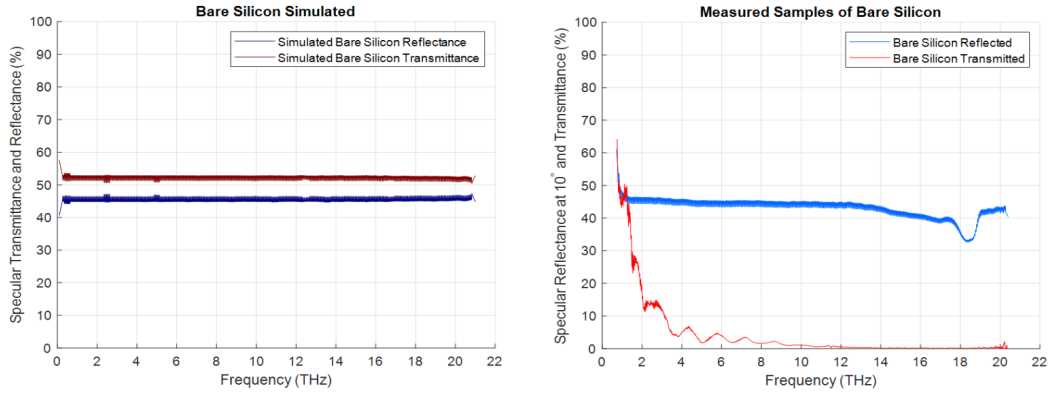


Figure 4.5: (Left) Simulated results from HFSS for the bare SI substrate. (Right) Measured results from the bare Si substrate.

The measured results of the untreated bare Si sample is shown in figure 4.6. MATLAB was used to calculate the effect incoherence has on transmittance by following the process laid out in [51]. A smoothing algorithm was applied to the results so that it may be interpreted more easily. It is clear that the transmittance measurements can not be trusted. An example of incoherence is shown in figure 4.7. With the top and bottom surfaces of the substrate

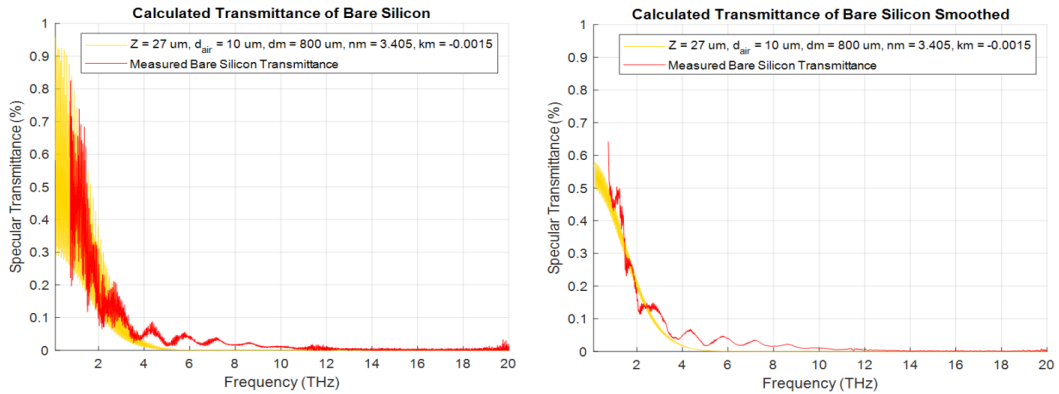


Figure 4.6: (Left) Measured and calculated transmittance of the bare Si substrate. (Right) Smoothing algorithm applied to the data in MATLAB. Z is the surface roughness, d_{air} is the depth of a substrate with the RI of air, d_m is the depth of Si substrate, n_m is the real RI value, and k_m is the imaginary RI value.

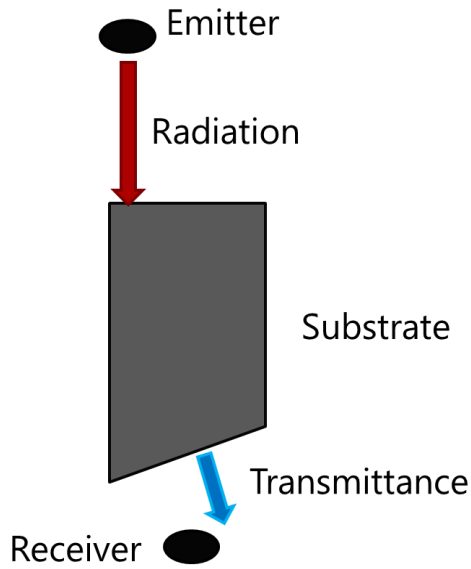


Figure 4.7: A graphic demonstrating incoherence. The substrate is not to scale.

not being parallel, this causes the coherent beam to become incoherent, the radiation scatters from the detector. The magnitude of this effect increases with frequency. It can be seen in figure 4.8 that the SWS has tremendous results for the transmittance, but most likely it is due to the incoherence of the measurement setup.

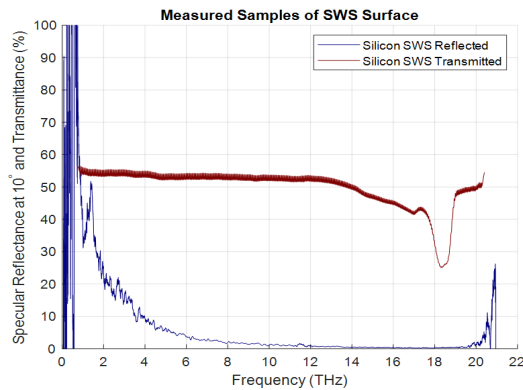


Figure 4.8: Measured results from the multi-level tapered structure surface.

4.3 Simulation Concerns for THz Filters

When designing filters in the THz frequency range, materials no longer have constant parameters, everything becomes frequency-dependent. HFSS has an option to create frequency-dependent materials that may come in useful if the substrate is lossy. If the filter is broadband, HFSS seems to have a wave port height dependency with the frequency range being simulated. For example, this substrate had to be split into 8 different simulations, each simulating a different frequency range up to 21 THz. When simulating the bare substrate, a great amount of simulation time can be saved if the substrate's dimensions is comparable to the solution frequency. Lastly, when simulating tapered structures, multi-modes may occur if the wavelengths being simulated are small compared to the filter. Figure 4.9 shows how many modes start to occur when simulating far beyond the diffraction edge. Modes are basic field patterns that fulfill Maxwell's equations only at certain frequencies, therefore, the probability of propagating higher-order modes increases with frequency [49].

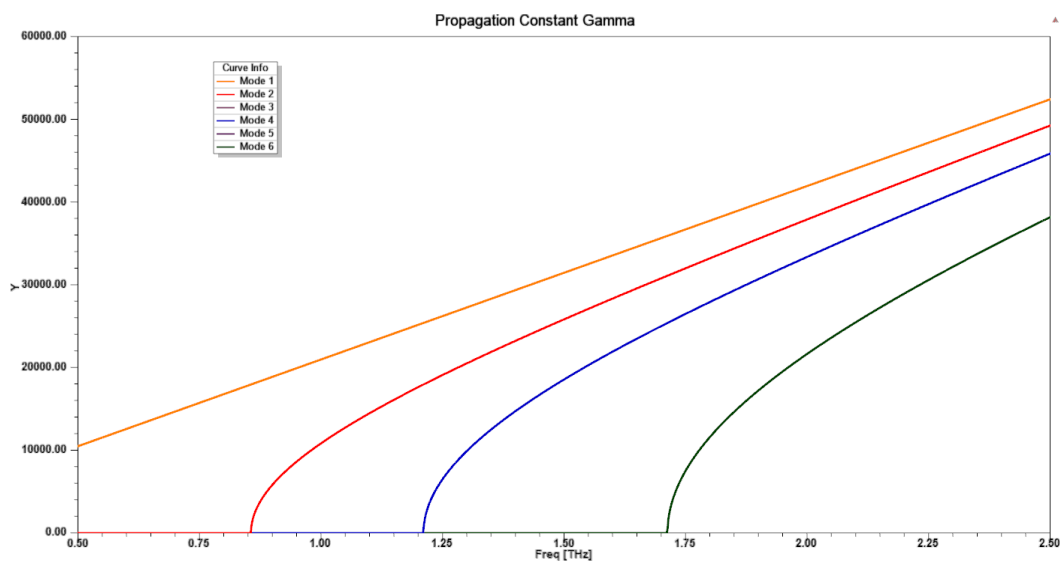


Figure 4.9: Simulated results from HFSS for the bare SI substrate.

4.4 Non-Tapered SWSs for a Bandpass Filter

This filter will not be fabricated, but the filter can be designed to filter the same wavelength spectrum as some of the work presented in the previous chapters to compare the methods. The bandwidth chosen will be from figure **2.7**, giving $f_1 \sim 250 \text{ THz} = 1200 \text{ nm}$ and $f_2 \sim 750 \text{ THz} = 400 \text{ nm}$. The center of this spectrum, from the perspective of a wavelength, is at 800 nm or 375 THz. The center of the spectrum, from the perspective of the frequency, is at 500 THz or 600 nm. Since HFSS plots in frequency, this is the frequency the filter will be designed for. Now that the cutoff frequency f_1 is known, the dimensions of the filter need to be calculated. The wavelength that determines the dimensions is different than the cutoff wavelength λ_1 in the spectrum. Therefore, equation **(3.7a)** will need to be modified to find the wavelength that discovers the sizes of the ARS. The interspace **(3.5b)** will also need to be adjusted for the desired variable λ from **(3.5a)**, to substitute into **(3.7a)**, since the interspace is unknown:

$$\text{Substitute } \Lambda = \frac{1}{10} \cdot \lambda \text{ into } I = \frac{1}{10} \cdot \Lambda \implies I = \frac{1}{10} \cdot \left(\frac{1}{10} \cdot \lambda\right) \implies I = \frac{\lambda}{100}$$

Now substitute the I from above and the effective pitch **(3.5d)** into **(3.7a)**.

$$\text{Substitute } I = \frac{\lambda}{100} \text{ and } \Lambda_{eff} = \frac{\lambda}{n_i + n_s} \text{ into } f_1 \sim \frac{c}{(2 \cdot \Lambda_{eff} + 3 \cdot I) \cdot n_s}$$

The following steps are to solve for λ :

$$\begin{aligned} f_1 \sim \frac{c}{(2 \cdot (\frac{\lambda}{n_i + n_s}) + 3 \cdot (\frac{\lambda}{100})) \cdot n_s} &\implies \frac{f_1 \cdot n_s}{c} \sim \frac{1}{(2 \cdot (\frac{\lambda}{n_i + n_s}) + 3 \cdot (\frac{\lambda}{100}))} \implies \\ \frac{f_1 \cdot n_s}{c} \sim \frac{1}{\frac{2 \cdot \lambda}{n_i + n_s} + \frac{3 \cdot \lambda}{100}} &\implies \frac{f_1 \cdot n_s}{c} \sim \frac{1}{\frac{2 \cdot \lambda \cdot 100}{(n_i + n_s) \cdot 100} + \frac{3 \cdot \lambda \cdot (n_i + n_s)}{100 \cdot (n_i + n_s)}} \implies \\ \frac{f_1 \cdot n_s}{c} \sim \frac{1}{\frac{200 \cdot \lambda + 3 \cdot \lambda \cdot (n_i + n_s)}{(n_i + n_s) \cdot 100}} &\implies \frac{f_1 \cdot n_s}{c} \sim \frac{(n_i + n_s) \cdot 100}{200 \cdot \lambda + 3 \cdot \lambda \cdot (n_i + n_s)} \implies \end{aligned}$$

$$1 \sim \frac{c \cdot (n_i + n_s) \cdot 100}{f_1 \cdot n_s \cdot 200 \cdot \lambda + f_1 \cdot n_s \cdot 3 \cdot \lambda \cdot (n_i + n_s)} \implies$$

$$\lambda \sim \frac{c \cdot (n_i + n_s) \cdot 100}{f_1 \cdot n_s \cdot 200 + f_1 \cdot n_s \cdot 3 \cdot (n_i + n_s)} \quad (4.3)$$

Finally, equation (4.3) may now be used to find the dimensions of the SWG by following the process laid out in section 3.2. The incident medium is air so the refractive index is $n_i \sim 1$ and the substrate is glass, therefore the refractive index is $n_s \sim 1.5$.

$$\lambda \sim \frac{3 \times 10^8 \cdot (1 + 1.5) \cdot 100}{500 \times 10^{12} \cdot 1.5 \cdot 200 + 500 \times 10^{12} \cdot 1.5 \cdot 3 \cdot (1 + 1.5)} \approx 482 \text{ nm}$$

Now the pitch, interspace, and depth may be computed with (3.5a) to (3.5c) respectively.

$$\Lambda = \frac{1}{10} \cdot \lambda = \frac{1}{10} \cdot 482 \times 10^{-9} \implies \Lambda = 48.2 \text{ nm}$$

$$I = \frac{1}{10} \cdot \Lambda = \frac{1}{10} \cdot 48.2 \times 10^{-9} \implies I = 4.82 \text{ nm}$$

$$D = \frac{1}{4} \cdot \lambda = \frac{1}{4} \cdot 482 \times 10^{-9} \implies D = 120.5 \text{ nm}$$

Before the cutoff frequencies are able to be determined with (3.7a) and (3.7d), equation (3.5a) is needed to calculate f_1 .

$$\Lambda_{eff} = \frac{\lambda}{n_i + n_s} = \frac{482 \times 10^{-9}}{1 + 1.5} \implies \Lambda_{eff} = 192.8 \text{ nm}$$

$$f_1 \sim \frac{c}{(2 \cdot \Lambda_{eff} + 3 \cdot I) \cdot n_s} \implies$$

$$f_1 \sim \frac{3 \times 10^8}{(2 \cdot 192.8 \times 10^{-9} + 3 \cdot 4.82 \times 10^{-9}) \cdot 1.5} \implies f_1 \sim 500 \text{ THz}$$

$$f_2 \sim \frac{c}{(\Lambda + 2 \cdot I) \cdot n_s} \implies$$

$$f_2 \sim \frac{3 \times 10^8}{(482 \times 10^{-9} + 2 \cdot 4.82 \times 10^{-9}) \cdot 1.5} \implies f_2 \sim 3,458 \text{ THz}$$

Now that the cutoff frequencies are known, equations **(3.4b)** and **(3.8b)** will discover how broadband the filter is.

$$O = \frac{f_2}{f_1} \implies \frac{3,458}{500} \implies O = 6.916$$

$$B = f_2 - f_1 \implies 3,458 - 500 \implies B = 2958 \text{ THz}$$

Lastly, the minimums and maximums can be computed to locate the bandpass filters within this filter's frequency spectrum bandwidth using **(3.7b)** and **(3.7c)** respectively.

$$f_{min} \sim f_1 \cdot (2 \cdot m + 1) \implies$$

$$f_{min} \sim 500 \text{ THz } (m = 0), 1500 \text{ THz } (m = 1), \text{ and } 2500 \text{ THz } (m = 2)$$

$$f_{max} \sim f_1 \cdot (2 \cdot m) \implies$$

$$f_{max} \sim 1000 \text{ THz } (m = 1), 2000 \text{ THz } (m = 2), \text{ and } 3000 \text{ THz } (m = 3)$$

The parameters containing valuable information and useful for modeling a

Table 4.3:
AR Surface of Non-Tapered SWS Filter Design Parameters for Quartz

Property		Value
Substrate's RI	n_s	1.5
Cutoff frequency	f_1	500 THz
Wavelength	λ	482 nm
Pitch	Λ	48.2 nm
Interspace	I	4.82 nm
Depth	D	120.5 nm
Cutoff frequency	f_2	3,458 THz
Octaves	O	6.916
Bandwidth	B	2958 THz
Bandpass Filters	f_{min}	500 (m = 0), 1500 (m = 1), and 2500 (m = 2) THz
Maximums	f_{max}	1000 (m = 1), 2000 (m = 2), and 3000 (m = 3) THz

non-tapered ARG on quartz are listed in table 4.3. Figure 4.10 displays the AR surface of the designed profile for the MES. The simulated results of this coating are depicted in figure 4.11. It can be seen that the calculations closely match the simulated results for the first bandpass filter within the bandwidth. As the frequencies become larger, the worse the higher-order bandpass filters become, the calculations slowly become less accurate for the larger frequencies. From observing the last bandpass filter in the bandwidth, the likely cause is severe interference from the smaller wavelengths. Notice the reference value is 4%, this is expected since the substrate is glass, also the maximums do not greatly exceed this value. The cutoff frequencies seem to be fairly accurate, even though the calculations suffered at larger frequencies in the bandwidth, f_2 was fairly close to the simulated value.

Now these results can be compared to other design methods starting with figure 2.7(b). The optimal structure is only effective for half the wavelength spectrum. At normal incidence on a glass substrate with a flat surface, 96% of

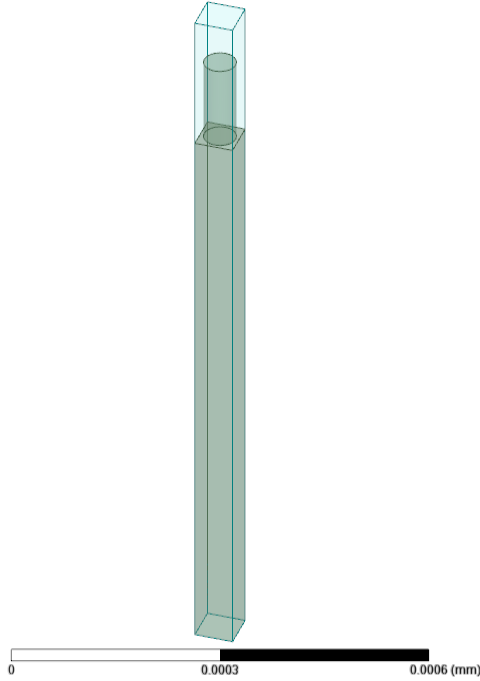


Figure 4.10: HFSS model of a nano-pillar AR surface having a depth $d = 120.5$ nm, pitch $\Lambda = 48.2$ nm, and period $p = 53.02$ nm on a quartz substrate having a thickness of 800 nm.

the wavelengths would be transmitted. For this same wavelength spectrum, it is shown in figure 4.11 that this method is active across the entire frequency range and does not become greater than 2% reflectance. Figure 2.34(c) unfortunately is not sensitive enough to distinguish the difference between the design methods, but this AR surface has a much greater operating bandwidth than both references demonstrated in the figures.

The equations can be further tested by simulating this structure with a much higher RI such as silicon. Since the dimensions are known, the process laid out in section 3.2 can be utilized. If the wavelength is unknown, then the simplest solution would be to use (3.5a) and multiply the pitch by 10. The first step is to start with (3.5d), the refractive index of silicon is $n_s \sim 3.45$.

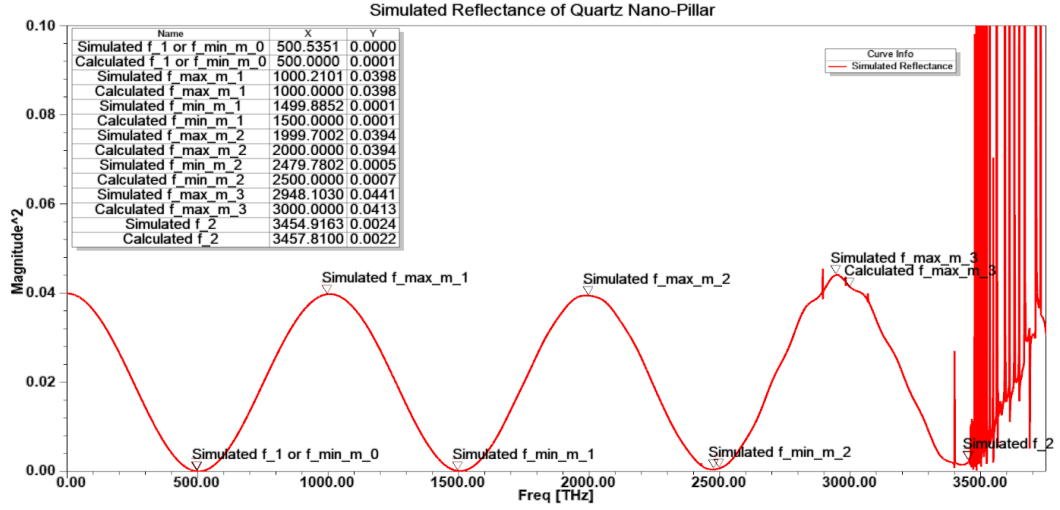


Figure 4.11: The magnitude² reflectance of the scattering parameters S_{11} for the quartz nano-pillar AR surface at perpendicular incidence.

$$\Lambda_{eff} = \frac{\lambda}{n_i + n_s} \implies \frac{482 \times 10^{-9}}{1 + 3.45} \implies \Lambda_{eff} = 108.315 \text{ nm}$$

Now the rest of the process can be computed beginning with (3.7a):

$$f_1 \sim \frac{c}{(2 \cdot \Lambda_{eff} + 3 \cdot I) \cdot n_s} \implies \frac{3 \times 10^8}{(2 \cdot 108.315 \times 10^{-9} + 3 \cdot 4.82 \times 10^{-9}) \cdot 3.45} \implies$$

$$f_1 \sim 376 \text{ THz}$$

$$f_2 \sim \frac{c}{(\Lambda + 2 \cdot I) \cdot n_s} \implies \frac{3 \times 10^8}{(48.2 \times 10^{-9} + 2 \cdot 4.82 \times 10^{-9}) \cdot 3.45} \implies$$

$$f_2 \sim 1,503 \text{ THz}$$

$$B = f_2 - f_1 \implies 1,503 - 376 \implies B = 1,127 \text{ THz}$$

$$O = \frac{f_2}{f_1} \implies \frac{1,127}{376} \implies O \sim 3$$

$$f_{min} \sim f_1 \cdot (2 \cdot m + 1) \implies$$

$$f_{min} \sim 376 \text{ THz } (m = 0) \text{ and } 1129 \text{ THz } (m = 1)$$

$$f_{max} \sim f_1 \cdot (2 \cdot m) \implies$$

$$f_{max} \sim 753 \text{ THz } (m = 1) \text{ and } 1505 \text{ THz } (m = 2)$$

The parameters comprising of beneficial information and helpful for modeling a non-tapered ARS on silicon are listed in table 4.4. Figure 4.12 demonstrates the AR surface of the designed profile for the SWG. The simulated results of this coating are shown in figure 4.13. Just by changing the refractive index, this AR surface is less than half as broadband as the glass filter. There are also fewer calculated bandpass filters within the bandwidth even though the third bandpass filter appears at the end of the frequency spectrum.

Table 4.4:
AR Surface of Non-Tapered SWS Filter Design Parameters for Silicon

Property		Value
Substrate's RI	n_s	3.45
Wavelength	λ	482 nm
Pitch	Λ	48.2 nm
Interspace	I	4.82 nm
Depth	D	120.5 nm
Cutoff frequency	f_1	376 THz
Cutoff frequency	f_2	1,503 THz
Octaves	O	3
Bandwidth	B	1127 THz
Bandpass Filters	f_{min}	376 (m = 0), and 1129 (m = 1) THz
Maximums	f_{max}	753 (m = 1), and 1505 (m = 2) THz

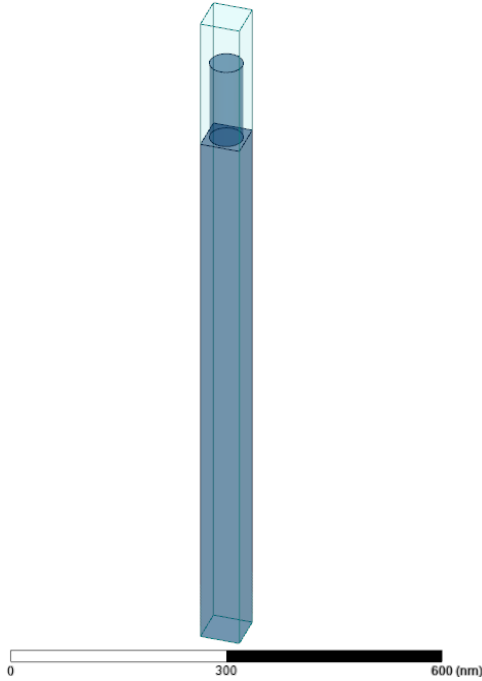


Figure 4.12: HFSS model of a nano-pillar AR surface having a depth $d = 120.5$ nm, pitch $\Lambda = 48.2$ nm, and period $p = 53.02$ nm on a silicon substrate having a thickness of 800 nm.

Inspecting figure 4.13 shows that only the cutoff frequency equations are accurate. As the wavelengths become smaller, the more severe the error becomes in the calculations compared to the simulated data. This may be due to the RI being so great, causing serious interference as mentioned at the end of section 3.2. The equations f_{min} and f_{max} become futile for high RI materials. It is surprising that, if this is due to interference, the maximums do not exceed the reference value of 30% which is the presumed value for silicon. Notice the minimums do not completely reach zero reflectance except for the middle passband filter in the bandwidth. The last bandpass is expected to be more inaccurate from being at the end of the spectrum. The first bandpass filter within the bandwidth is the only filter that can be calculated precisely.

When the profile of the MES is changed to a square instead of a cylinder,

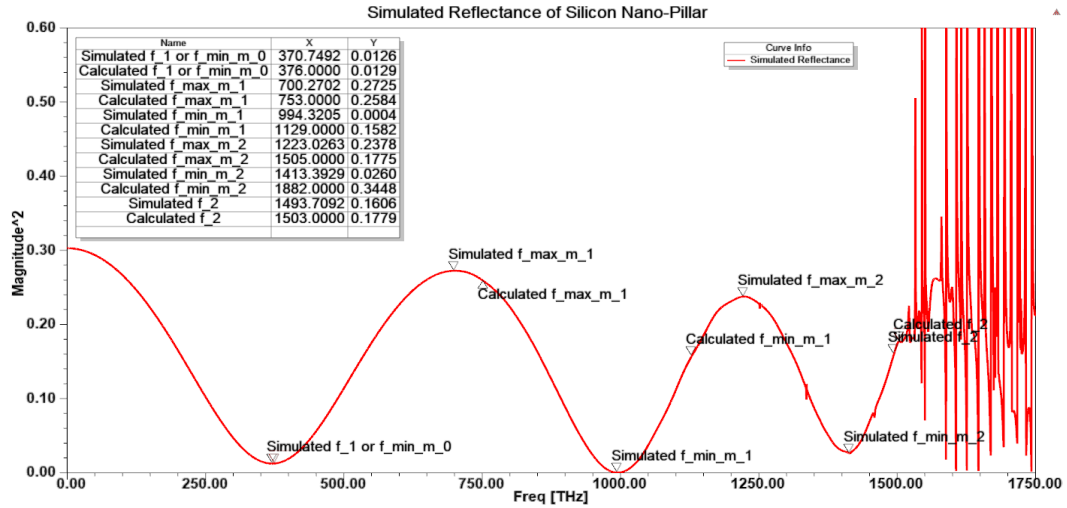


Figure 4.13: The magnitude² reflectance of the scattering parameters S_{11} for the silicon nano-pillar AR surface at perpendicular incidence.

the results seem to suffer slightly, even with a glass substrate. The results progress as if the filter has a higher RI. The calculations become worse as the wavelength becomes smaller. None of the simulated minimums reached zero reflectance. The cutoff frequency equations were accurate. The silicon AR surface calculations deteriorated faster than the nano-pillar AR surface. The cutoff frequency f_2 was still precise but f_1 slightly deviated from the calculation. These unexpected, inferior results might be caused by the larger volume the structure has compared to the cylinder, giving rise to the probability of a higher magnitude of interference that a greater RI would give. These filters are interference-based. Since the square is a rhombus, these planes could assist in increasing the magnitude of interference also producing the effect of a higher RI when the shape of the cylinder might be hindering this reaction.

4.5 Conclusion

Both design guidelines for tapered and non-tapered filters with solved examples for each filter design are demonstrated. Simulations and calculations are compared to evaluate the validity of the formulas. Two different examples for tapered and non-tapered structures are calculated with a RI of silicon and the other glass to compare the accuracy of the equations. The following chapter will examine the fabrication process for manufacturing filters using a femtosecond laser.

Chapter 5

Fabricating SWS Surfaces by Femtosecond Laser

One of the promising procedures for fabricating ARGs in the THz spectral region with varying MES shapes is femtosecond laser processing [5]. The MES's are developed by the ultrashort laser pulses which ablate the surface of the medium. This recent, adaptable technology can operate on curved or planar surfaces [10]. Unlike machining, femtosecond laser processing is a non-contact technique, preferable for processing rigid and fragile materials.

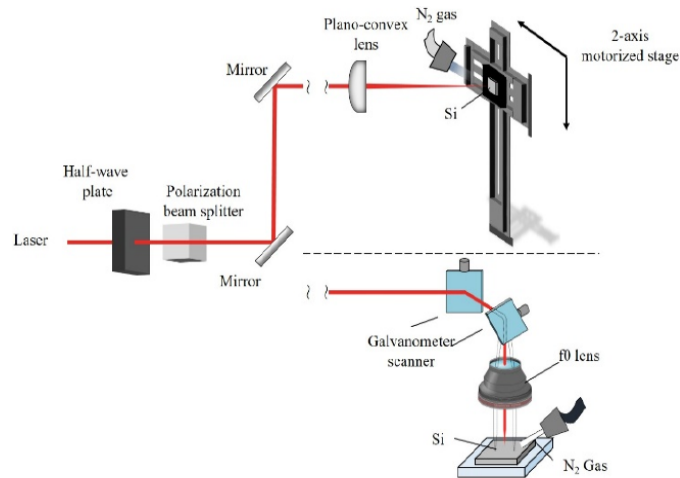


Figure 5.1: Two different processing systems. (Top) A steady pace of 5 mm/s is the speed the 2-axis motorized stage is capable of moving. (Bottom) The laser beam from the $f\theta$ lens is concentrated on the plate even if the incident beam is oblique. A scan speed of 2825 mm/s is achieved by revolving the galvanometer mirrors (from [11]).

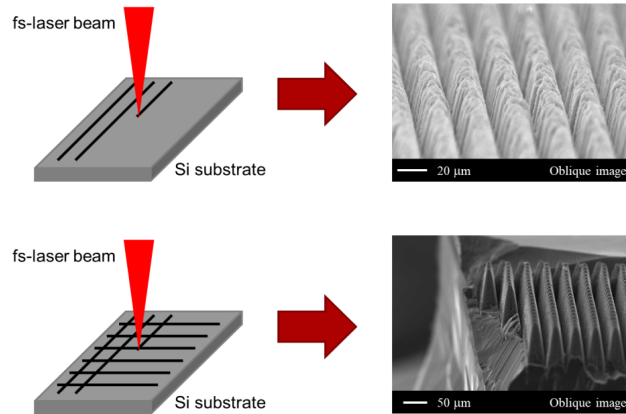


Figure 5.2: The one and two dimensional design process with a femtosecond laser, courtesy of NGIT.

These lasers have exceptionally small pulse widths, which restricts thermal diffusion throughout the ablation period providing reduced molten media, which produces quality micro-fabrication. The femtosecond laser processing technology has been considerably researched and applied due to the benefits mentioned above [6].

The femtosecond processing setup is displayed in figure 5.1. For silicon media, the femtosecond laser is illuminated to the surface of the Si medium with a pulse width of 700 fs, center wavelength of 1045 nm, and repetition frequency of 100 kHz to construct periodic microgrooves. The laser power is set to 800 mW and the scanning time adjusts the aspect ratio [6]. Figure 5.2 shows the 2-D manufacturing process for SWS surfaces. The femtosecond laser is capable of fabricating 2-D SWSs by either employing the 2-axis motor or revolving the galvanometer mirrors.

The scanning speed determines the dimensions of the MES. The gas present while etching the surface is also a determining factor. N_2 was found to be less absorbing than SF_6 in the IR region. Structures with blunt tips were made

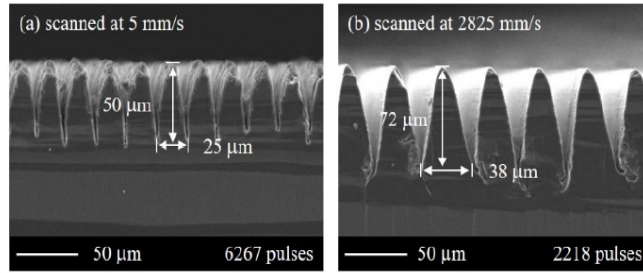


Figure 5.3: (a) Scanned at at 5 mm/s and (b) was scanned at 2825 mm/s. Processed samples comparing differing scanning speeds (from [11]).

with N_2 and sharp peaks with SF_6 [4]. During laser irradiation, the thermal effect is thought to be the cause of molten material [6]. Plasma waves are generated onto surfaces of media when the considerable peak power of the pulses has an intensity close to the ablation threshold. Due to the interference between the plasma waves and laser pulses, the polarization of the incident ray of light is perpendicular to the fabricated structures [9]. The TM mode is when the incident radiation's electric field is perpendicular to the grooves [6].

The reconnecting of debris and melted material on samples from the thermal influence effect is connected to processing at a comparatively slow speed which is demonstrated in figure 5.3. A change in the scanning system to a galvanometer scanner from a 2-axis motorized stage improves the scanning speed to m/s instead of mm/s in order to lessen this effect. Improving the laser beam's scan speed also reduces the effective pulse number. The determination of the structure's profile and aspect ratio are also impeded thermal influence. Theoretically, thermal diffusion should not occur since the radiation of the laser pulse will cease before this effect can begin. This is due to the fact that thermal diffusion begins at 10^{-9} s and the femtosecond laser is appreciably briefer, executing non-thermal manufacturing at 10^{-15} s. A concern is if ablated media, absorbing incident pulses repeatedly, are reconnecting at the initial position if

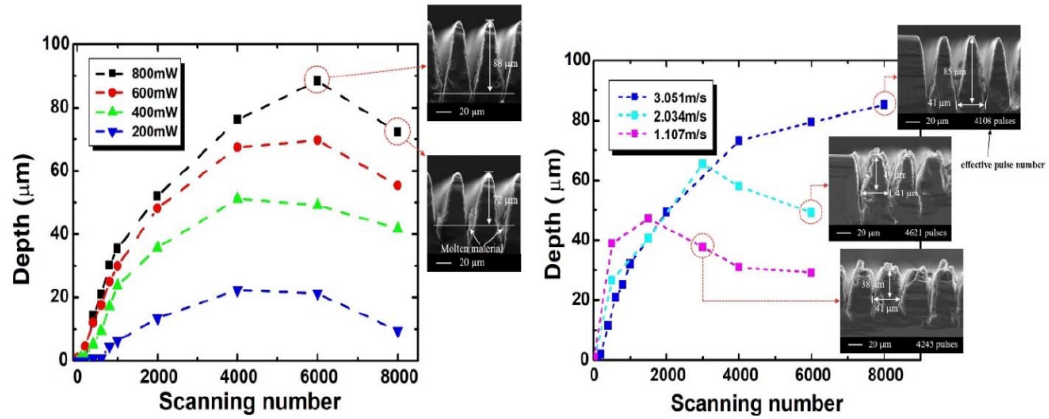


Figure 5.4: (Left) A relation between scanning number and depth as a function of scanning speed set at 2825 mm/s. (Right) A relation between scanning number and scanning speed as a function of Laser power set to 800 mW (from [11]).

the laser pulses are repeatedly illuminated at the same location [11].

The results of the femtosecond laser's scanning number are depicted in figure 5.4. The graphic on the right shows that the taper will be manufactured with a greater height when the scan speed is increased. The number of pulses repeatedly radiated at the same location will be reduced as long as the scan speed is rising, enabling the reconnecting of debris and absorption of repeated incident pulses to be hindered. The graphic on the left shows that there is a limit around the scanning number 6000 aiming for the largest height of the taper. The melted media on the wall of the grooves or at the bottom of the

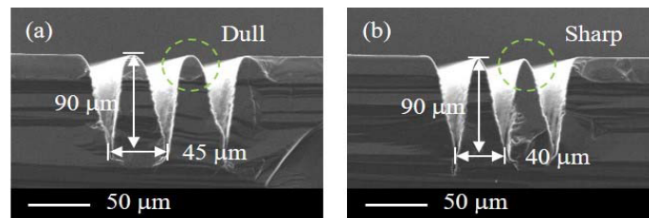


Figure 5.5: (a) Has a pitch = 45 μm and (b) is a pitch = 40 μm . Tapers with different peaks from changing the pitch (from [11]).

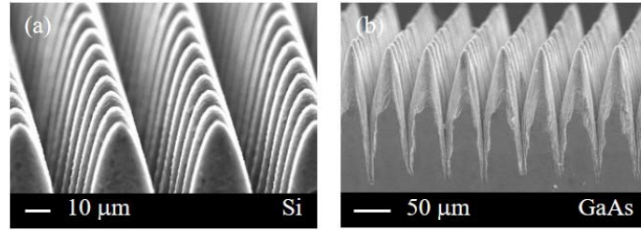


Figure 5.6: (a) The Si and (b) GaAs media showing manufactured 2-dimensional structures (from [11]).

valleys is from the energy of the laser pulses being converted to heat since the intensity of the pulses penetrating to the bottom began to be less than the processing threshold of ablation as the tapers were being lasered [11].

The femtosecond laser can also be precise when adjusting the pitch to obtain dull or sharp peaks which are shown in figure 5.5. The femtosecond laser is a reliable method for fabricating Si AR surfaces. Si and GaAs have little dispersion and good transparency in the THz spectral range and their profiles are illustrated in figure 5.6.

The femtosecond laser can also be used in a liquid environment to manufacture carbide nanoparticles by laser ablation which concentrates the pressure state and high temperature [8]. For a copper substrate, there was no conglomeration when fabricating the laser-induced periodic surface structures (LIPSSs). Even though the exceptionally high peak energy will immediately raise the value of the temperature considerably, but as long as the pulse energy is not greater than the processing threshold, the energy around the illuminated area will be regarded to be interpreted as heat [7].

To conclude, the femtosecond fabrication setup is depicted and explained. The capabilities and limitations are described in depth. 2-D tapered structures can be processed and the precise control of the tapered profile is shown. The femtosecond laser is a non-contact method, preferable for fragile substrates,

that can operate on curved surfaces and can even be operated in a liquid environment. In the following chapter, the Bruker IFS 125HR Spectrometer is the equipment that measured the filter and will be explained.

Chapter 6

Measurement of SWS Surfaces

The Bruker IFS 125HR measures a wide spectral range with modular vacuum optics and is a high-resolution research Fourier transform infrared spectroscopy (FT-IR) spectrometer. The interferometer model establishes minor polarization effects and a great energy throughput. The Bruker spectrometer is depicted in

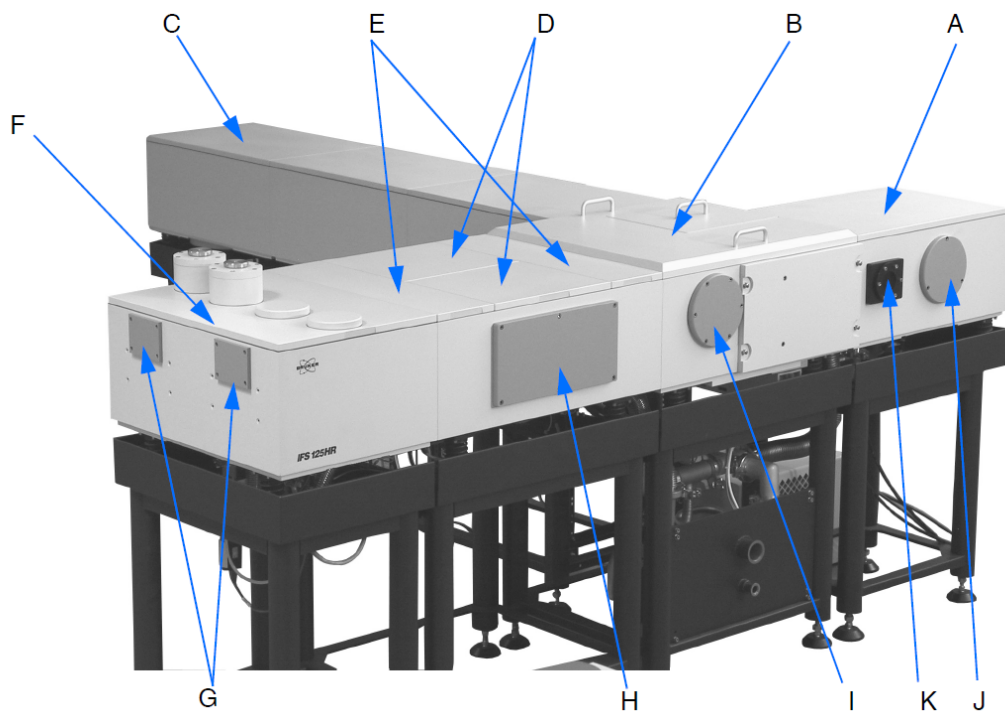


Figure 6.1: The compartments in the Bruker IFS 125HR (from [52]).

Table 6.1:
Definitions for Compartments in the Spectrometer

Location	Definition
A	Source compartment (enlarged version shown)
B	Interferometer compartment
C	Scanner compartment
D	Sample compartments
E	Channel switching sub-chamber
F	Detector compartment
G	Detector outlet ports
H	Cover plate, provides access to large accessory
I	Outlet port for parallel beam
J	Input port for parallel beam
K	Input port for focused beam

figure **6.1**. A table listing each of the compartments in the Bruker IFS 125HR is displayed in table **6.1**. All information for this chapter is from [52].

FT-IR spectrometers have many advantages for measuring in the THz spectrum. The scan time of the broadband spectral range of wavelengths is brief due to the wide bandwidth being simultaneously measured with a high resolution. The interferometer in the spectrometer operates as a Michelson interferometer. Transmittance or reflectance is calculated by comparing the response from the sample being inserted into the path of the detector to the prerecorded initial beam of light the detector received. The spectrometer emits a beam of radiation that is collimated, producing a coherent parallel beam, which is then split into two beams. One beam is focused on the sample and the other is relayed back to the sample by a moving mirror. The resolution is related to the accuracy in the movement of the mirror, which is applying interference. The Fourier transform is then applied to the data which produces

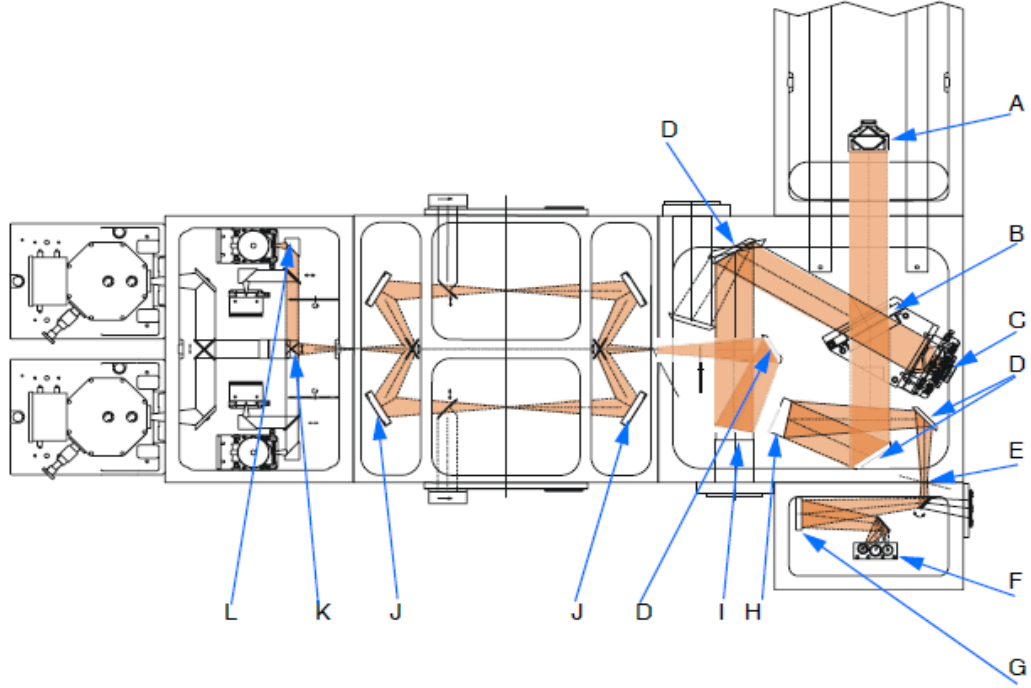


Figure 6.2: The Spectrometer's optical path (from [52]).

the spectral response.

The source compartment can independently choose between 3 housed water-cooled sources. The interferometer compartment receives the concentrated source ray beam. The optical path difference is resolved precisely by a regulated HeNe laser in the interferometer compartment. A beam splitter and retroreflecting mirrors are incorporated with the invariably aligned interferometer. The interferometer has an incidence angle of 30° to more effectively employ the beam splitter and to limit polarization effects. The scanner compartment contains 2 vacuum chambers in the standard configuration. There are 2 drive units, a DC (Direct Current) motor and a linear motor, that drives the scanner. These are known as the outer and inner scanners. The inner scanner may only be utilized for a meager resolution measurement. The outer scanner

Table 6.2:
Definitions for Components in the Spectrometer's Optical Path

Location	Definition
A	Scanner with movable retroreflecting mirror
B	Beam splitter
C	Fixed retroreflecting mirror
D	Folding mirror
E	Input aperture (field stop)
F	Sources
G	Spherical mirror
H	Collimating parabolic mirror
I	Focusing parabolic mirror
J	Torodial mirror
K	Collimating parabolic mirror
L	Focusing parabolic mirror

establishes the sliding movement, the inner scanner's primary function is to rectify the fluctuations from the outer scanner. The sample compartment has 2 big compartments with concentrated ray beams. There are 2 channel switching sub-chambers contained in the Bruker IFS 125HR. Their purpose is to direct the ray beams to the proper sample compartments. The detector compartment can house 2 external and 4 internal detectors. The ray beams can access all of the detectors from both sample chambers. The big liquid-helium cooled detectors, far-infrared (FIR) bolometers as an example, may be equipped to the 2 external locations. 4 of the liquid -nitrogen room temperature or cooled can be inside the compartment. The liquid N_2 -cooled MCT detector system is the standard configuration for great spectral sensitivity and mid-infrared (MIR) spectral range. The optical path of the Bruker IFS 125HR is illustrated in figure 6.2 and its corresponding table of components in table 6.2.

The Spectrometer covers a wide range of frequencies by exchanging sources. For this experiment, the mercury arc lamp was utilized. Once the light is modulated, the light is sent to the sample at the focal beam. A liquid helium bolometer was used in the detector system, since measuring in the far-infrared.

Overall, the measurement system, Bruker IFS 125HR, is illustrated and explained. All of the compartments within the system have been discussed and their functions defined. The optical path is shown and all of its components listed. The following chapter will explore the pathways of future work and conclusions drawn from the results of this thesis.

Chapter 7

Conclusions and Future Work

The desire to eliminate reflections from surfaces has been sought after for many decades. The primary method for designing ARS is EMT. Time was expended to learn the basics of operation for quarter-wave thin films, destructive interference was discovered to be the solution. The angles of reflection and refraction were found to be crucial for this technology. The propagation angle or the angle of refraction is the solution. The basics for AR surfaces using SWGs were discovered to remain the same. The filter still operates around Snell's Law. EMT should no longer be the cornerstone for modern AR surfaces. The dimensions of ARGs corresponds to the wavelength spectrum of interest, provoking multiple internal reflections from neighboring structures to capture the wavelengths of interest.

This thesis presented a new process using formulas that are based on the wavelength spectrum of interest. The equations are optimized for tapered and non-tapered structures. Multi-level tapered SWGs are designed to produce an optimized bandpass filter. Solved examples for tapered and non-tapered structures with varying values of the RI are shown. The measured results for the sample, the setup was found to be incoherent, causing the transmittance to fall exponentially to zero. The MATLAB code proved this assumption to be

true. Design concerns for simulating MESs in the THz spectrum were discussed. The fabrication of SWSs with a femtosecond laser is examined. The Bruker spectrometer for measuring the ARSs is also discussed.

In conclusion, this work presented a method for swiftly designing tapered and non-tapered structures to filter a certain bandwidth in the electromagnetic spectrum without having to do trial and error calculations or optimizations. The proposed method is wavelength dependent, which provides a simple process to filter a section of the wavelength spectrum easily. The recommended filter, anti-reflective surface using sub-wavelength structures, have polarization insensitivity, and is quasi-omnidirectional. This filter is a powerful device for future AR technology.

7.1 Future Work

The performance of the filter can be further improved by changing the substrate material to float-zone silicon. Its resistivity and loss tangent are appropriate for the THz spectral region. Since silicon has a high refractive index, research of materials that are transparent in the infrared spectral region needs to be investigated. If quartz is transparent in this region, then quartz would be the suitable material for the substrate.

A well-known method for improving the transmittance of a medium is a double-sided AR filter. This requires both the top of the medium and bottom to be etched with SWSs. Typical applications for the technology that generally desires AR surfaces with high transmittance includes diodes, solar technology, and any transparent media.

References

- [1] *HIRMES: A New High-resolution Mid-infrared Spectrometer for SOFIA kernel description*, <https://science.nasa.gov/technology/technology-stories/HIRMES-High-resolution-Mid-infrared-Spectrometer-SOFIA>, Accessed: 2019-06-10.
- [2] C. E. Lane, "Filters in action," *Electrical Engineering*, vol. 52, no. 12, pp. 813–816, Dec. 1933, ISSN: 0095-9197. DOI: 10.1109/EE.1933.6430507.
- [3] H. W. Bode, "A general theory of electric wave filters," *The Bell System Technical Journal*, vol. 14, no. 2, pp. 211–214, Apr. 1935, ISSN: 0005-8580. DOI: 10.1002/j.1538-7305.1935.tb00413.x.
- [4] H. Raut, A. G. Venkatesan, S. Nair, and S. Ramakrishna, "Anti-reflective coatings: A critical, in-depth review," *Energy & Environmental Science*, vol. 4, pp. 3779–3804, Aug. 2011. DOI: 10.1039/C1EE01297E.
- [5] N. Horita, X. Yu, M. Takeuchi, S. Ono, and J. Bae, "Anti-reflection characteristics of laser drilling subwavelength tapered structures at terahertz frequencies," in *2018 43rd International Conference on Infrared, Millimeter, and Terahertz Waves (IRMMW-THz)*, Sep. 2018, pp. 1–2. DOI: 10.1109/IRMMW-THz.2018.8510489.
- [6] X. Yu, M. Takeuchi, S. Ono, and J. Bae, "Terahertz antireflective structures fabricated via femtosecond laser ablation," in *2018 Conference on Lasers and Electro-Optics Pacific Rim (CLEO-PR)*, Jul. 2018, pp. 1–2.
- [7] X. Yu, M. Sudo, F. Itoigawa, and S. Ono, "Patterning oxidation via femtosecond laser irradiation on copper substrate," in *2018 Conference on Lasers and Electro-Optics Pacific Rim (CLEO-PR)*, Jul. 2018, pp. 1–2.
- [8] S. Terakawa, X. Yu, T. Asaka, F. Itoigawa, S. Ono, and M. Sudo, "Fabrication of carbide nanoparticles by femtosecond laser ablation of silicon

- and molybdenum in hexane,” in *2018 Conference on Lasers and Electro-Optics Pacific Rim (CLEO-PR)*, Jul. 2018, pp. 1–2.
- [9] M. Hishiki, X. Yu, M. Sudo, F. Itoizawa, and S. Ono, “Fabricating fine structures induced by femtosecond laser on molybdenum surface,” in *2018 Conference on Lasers and Electro-Optics Pacific Rim (CLEO-PR)*, Jul. 2018, pp. 1–2.
- [10] A. Brahm, S. Döring, A. Wilms, G. Notni, S. Nolte, and A. Tünnermann, “Laser-generated broadband antireflection structures for freeform silicon lenses at terahertz frequencies,” in *2014 39th International Conference on Infrared, Millimeter, and Terahertz waves (IRMMW-THz)*, Sep. 2014, pp. 1–2. DOI: 10.1109/IRMMW-THz.2014.6956345.
- [11] X. Yu, N. Horita, M. Takeuchi, M. Sudo, S. Ono, and J. Bae, “Studying of thermal influence for improving anti-reflective characteristics of moth-eye structures fabricated by femtosecond laser processing,” in *2018 43rd International Conference on Infrared, Millimeter, and Terahertz Waves (IRMMW-THz)*, Sep. 2018, pp. 1–2. DOI: 10.1109/IRMMW-THz.2018.8510112.
- [12] C. Brückner, B. Pradarutti, S. Riehemann, O. Stenzel, R Steinkopf, A Gebhardt, G. Notni, and A. Tünnermann, “Moth-eye structures for reduction of fresnel losses at thz components - art. no. 61940n,” *Proceedings of SPIE - The International Society for Optical Engineering*, Apr. 2006. DOI: 10.1117/12.662199.
- [13] C. Brückner, B. Pradarutti, O. Stenzel, R Steinkopf, S. Riehemann, G. Notni, and A. Tünnermann, “Broadband antireflective surface-relief structure for thz optics,” *Optics express*, vol. 15, pp. 779–89, Mar. 2007. DOI: 10.1364/OE.15.000779.
- [14] M. S. Mirotznik, B. L. Good, P. Ransom, D. Wikner, and J. N. Mait, “Broadband antireflective properties of inverse motheye surfaces,” *IEEE Transactions on Antennas and Propagation*, vol. 58, no. 9, pp. 2969–2980, Sep. 2010, ISSN: 0018-926X. DOI: 10.1109/TAP.2010.2052575.
- [15] Y. Li, Bin, and YiMing Zhu, “Broadband terahertz antireflective coating by polymer hot deformation,” in *2015 Opto-Electronics and Communications Conference (OECC)*, Jun. 2015, pp. 1–3. DOI: 10.1109/OECC.2015.7340318.

- [16] X. Dong and L. Chen, "Ultrabroadband plasmonic absorber based on biomimetic compound eye structures," *IEEE Photonics Journal*, vol. 10, no. 1, pp. 1–7, Feb. 2018, ISSN: 1943-0655. DOI: 10.1109/JPHOT.2018.2794201.
- [17] J Q Xi, J. K. Kim, E E Schubert, D. Ye, T M Lu, S. H. Lin, and J. S Juneja, "Very low-refractive-index optical thin films consisting of an array of sio2 nanorods," *Optics letters*, vol. 31, pp. 601–3, Apr. 2006. DOI: 10.1364/OL.31.000601.
- [18] X. Yan, D. Poxson, J. Cho, R. E. Welser, A. Sood, J. K. Kim, and E Fred Schubert, "Enhanced omnidirectional photovoltaic performance of solar cells using multiple-discrete-layer tailored- and low-refractive index anti-reflection coatings," *Advanced Functional Materials*, vol. 23, pp. 583–590, Feb. 2013. DOI: 10.1002/adfm.201201032.
- [19] R. Brunner, A. Deparnay, M. Helgert, M. Burkhardt, T. Lohmüller, and J. P. Spatz, "Product piracy from nature: Biomimetic microstructures and interfaces for high-performance optics," *Proceedings of SPIE - The International Society for Optical Engineering*, vol. 7057, Aug. 2008. DOI: 10.1117/12.795939.
- [20] E. E. Perl, C. Lin, W. E. McMahon, J. E. Bowers, and D. J. Friedman, "Design of ultra-broadband antireflection coatings utilizing integrated moth-eye structures for multi-junction device applications," in *2013 IEEE 39th Photovoltaic Specialists Conference (PVSC)*, Jun. 2013, pp. 1902–1906. DOI: 10.1109/PVSC.2013.6744515.
- [21] C. Jung-Kubiak, J. Sayers, M. I. Hollister, A. Bose, H. Yoshida, L. Liao, J. Wong, S. Radford, G. Chattopadhyay, and S. Golwala, "Antireflective textured silicon optics at millimeter and submillimeter wavelengths," in *2017 11th European Conference on Antennas and Propagation (EuCAP)*, Mar. 2017, pp. 959–961. DOI: 10.23919/EuCAP.2017.7928608.
- [22] C.-H. Sun, P. Jiang, and B. Jiang, "Broadband moth-eye antireflection coatings on silicon," *Applied Physics Letters - APPL PHYS LETT*, vol. 92, Feb. 2008. DOI: 10.1063/1.2870080.
- [23] Y. Kanamori, M. Ishimori, and K. Hane, "High efficient light-emitting diodes with antireflection subwavelength gratings," *IEEE Photonics Technology Letters*, vol. 14, no. 8, pp. 1064–1066, Aug. 2002, ISSN: 1041-1135. DOI: 10.1109/LPT.2002.1021970.

- [24] B. Yuan, B. Thibeault, D. Payne, J. Mutitu, I. Perez-Wurfl, K. Dobson, B. Conrad, A. Barnett, and R. L. Opila, “Broadband ta₂o₅ moth-eye antireflection coatings for tandem solar cells on si,” in *2017 IEEE 44th Photovoltaic Specialist Conference (PVSC)*, Jun. 2017, pp. 315–318. DOI: 10.1109/PVSC.2017.8366026.
- [25] M. Karlsson and F. Nikolajeff, “Diamond micro-optics: Microlenses and antireflection structured surfaces for the infrared spectral region,” *Optics express*, vol. 11, pp. 502–7, Apr. 2003. DOI: 10.1364/OE.11.000502.
- [26] P.-C. Li and E. T. Yu, “Large-area omnidirectional coating on low-index materials,” *Journal of the Optical Society of America B Optical Physics*, vol. 30, pp. 2584–, Oct. 2013. DOI: 10.1364/JOSAB.30.002584.
- [27] J. H. Jung, E. D. Han, B. H. Kim, Y. H. Seo, and Y. M. Park, “Ultra-low light reflection surface using metal-coated high-aspect-ratio nanopillars,” *Micro Nano Letters*, vol. 14, no. 3, pp. 313–316, 2019, ISSN: 1750-0443. DOI: 10.1049/mnl.2018.5239.
- [28] C. M. Hsieh, J. Y. Chyan, W. Hsu, and J. A. Yeh, “Fabrication of wafer-level antireflective structures in optoelectronic applications,” in *2007 IEEE/LEOS International Conference on Optical MEMS and Nanophotonics*, Aug. 2007, pp. 185–186. DOI: 10.1109/OMEMS.2007.4373902.
- [29] Y. Peng, S. Wang, H. Cheng, and M. Chen, “Light extraction efficiency enhancement of deep-ultraviolet light-emitting diodes with nanostructured silica glass,” in *2016 IEEE 66th Electronic Components and Technology Conference (ECTC)*, May 2016, pp. 2455–2460. DOI: 10.1109/ECTC.2016.367.
- [30] M. Minot, “The angular reflectance of single-layer gradient refractive-index films,” *Journal of The Optical Society of America*, vol. 67, Aug. 1977. DOI: 10.1364/JOSA.67.001046.
- [31] J. Dobrowolski, D. Poitras, P. Ma, H. Vakil, and M. Acree, “Toward perfect antireflection coatings: Numerical investigation,” *Applied optics*, vol. 41, pp. 3075–83, Jul. 2002. DOI: 10.1364/AO.41.003075.
- [32] D. Poitras and J. Dobrowolski, “Toward perfect antireflection coatings. 2. theory,” *Applied optics*, vol. 43, pp. 1286–95, Mar. 2004. DOI: 10.1364/AO.43.001286.

- [33] P G Verly, J A Dobrowolski, and R R Willey, “Fourier-transform method for the design of wideband antireflection coatings,” *Applied optics*, vol. 31, pp. 3836–46, Jul. 1992. DOI: 10.1364/AO.31.003836.
- [34] H. Podmore and R. Lee, “Increasing solar cell power production on micro and nano satellites using sub-wavelength gratings,” in *2015 IEEE Aerospace Conference*, Mar. 2015, pp. 1–7. DOI: 10.1109/AERO.2015.7118884.
- [35] M. Chen, H.-c. Chang, A. Chang, S. H. Lin, J.-Q. Xi, and E F Schubert, “Design of optical path for wide-angle graded-index antireflection coatings,” *Applied optics*, vol. 46, pp. 6533–8, Oct. 2007. DOI: 10.1364/AO.46.006533.
- [36] C. S. Thompson and M. Zou, “Investigation of moth-eye antireflection coatings for photovoltaic cover glass using fdtd modeling method,” in *2014 IEEE 40th Photovoltaic Specialist Conference (PVSC)*, Jun. 2014, pp. 2273–2275. DOI: 10.1109/PVSC.2014.6925379.
- [37] Y. M. Song, “Biomimetic optic designs for advanced optoelectronics,” in *2014 16th International Conference on Transparent Optical Networks (ICTON)*, Jul. 2014, pp. 1–4. DOI: 10.1109/ICTON.2014.6876623.
- [38] J. Son, L. K. Verma, A. J. Danner, C. S. Bhatia, and H. Yang, “Omnidirectional optical transmission by optimized nano-structures of solar cells,” in *2010 35th IEEE Photovoltaic Specialists Conference*, Jun. 2010, pp. 001 577–001 580. DOI: 10.1109/PVSC.2010.5617128.
- [39] S. Boden and D. Bagnall, “Bio-mimetic subwavelength surfaces for near-zero reflection sunrise to sunset,” vol. 2, Jun. 2006, pp. 1358 –1361. DOI: 10.1109/WCPEC.2006.279683.
- [40] Z. Khezripour, F. F. Mahani, and A. Mokhtari, “Optimized design of silicon-based moth eye nanostructures for thin film solar cells,” in *2018 3rd Conference on Swarm Intelligence and Evolutionary Computation (CSIEC)*, Mar. 2018, pp. 1–4. DOI: 10.1109/CSIEC.2018.8405420.
- [41] H. Xia, K. Song, R. Wang, and L. Peng, “Study on a new sub-wavelength grating for antireflective structure of solar cell,” in *ISAPE2012*, Oct. 2012, pp. 778–781. DOI: 10.1109/ISAPE.2012.6408887.

- [42] N. Das, K. Charoenpitaks, and S. Islam, “Analysis of incident light angles on nano-grating structure for minimizing reflection losses in gaas solar cells,” in *2013 Australasian Universities Power Engineering Conference (AUPEC)*, Sep. 2013, pp. 1–6. DOI: 10.1109/AUPEC.2013.6725384.
- [43] Y. M. Song and Y. T. Lee, “Simulation of antireflective subwavelength grating structures for optical device applications,” in *2009 9th International Conference on Numerical Simulation of Optoelectronic Devices*, Sep. 2009, pp. 103–104. DOI: 10.1109/NUSOD.2009.5297202.
- [44] A. Sengupta, A Bandyopadhyay, J. Federici, and N. Ravindra, “Far infrared studies of silicon using terahertz spectroscopy,” *Materials Science and Technology*, vol. 4, pp. 39–48, Jan. 2005.
- [45] L. Duvillaret, F. Garet, and J L Coutaz, “Highly precise determination of optical constants and sample thickness in terahertz time-domain spectroscopy,” *Applied optics*, vol. 38, pp. 409–15, Feb. 1999. DOI: 10.1364/AO.38.000409.
- [46] D. M. Pozar, *Microwave Engineering; 4th Edition*. Hoboken, NJ: John Wiley & Sons, 2012, ISBN: 9781118298138. [Online]. Available: <https://www.wiley.com/en-us/Microwave+Engineering+%2C+4th+Edition-p-9781118298138>.
- [47] C. A. Balanis, *Advanced Engineering Electromagnetics; 2nd Edition*. Hoboken, NJ: John Wiley & Sons, 2012, ISBN: 9781118214763. [Online]. Available: <https://www.wiley.com/en-us/Advanced+Engineering+Electromagnetics+%2C+2nd+Edition-p-9781118214763>.
- [48] D. S. Hobbs and B. D. MacLeod, “Design, fabrication, and measured performance of anti-reflecting surface textures in infrared transmitting materials,” in *Window and Dome Technologies and Materials IX*, R. W. Tustison, Ed., International Society for Optics and Photonics, vol. 5786, SPIE, 2005, pp. 349–364. DOI: 10.1117/12.604532. [Online]. Available: <https://doi.org/10.1117/12.604532>.
- [49] *User’s Guide – High Frequency Structure Simulator kernel description*, <http://anlage.umd.edu/HFSSv10UserGuide.pdf>, Accessed: 2020-11-25.
- [50] M. Pradhan, R. Garg, and M. Arora, “Multiphonon infrared absorption in silicon,” *Infrared Physics*, vol. 27, no. 1, pp. 25–30, 1987, ISSN: 0020-0891.

DOI: [https://doi.org/10.1016/0020-0891\(87\)90046-7](https://doi.org/10.1016/0020-0891(87)90046-7). [Online]. Available: <http://www.sciencedirect.com/science/article/pii/S0020089187900467>.

- [51] C. L. Mitsas and D. I. Siapkas, "Generalized matrix method for analysis of coherent and incoherent reflectance and transmittance of multilayer structures with rough surfaces, interfaces, and finite substrates," *Appl. Opt.*, vol. 34, no. 10, pp. 1678–1683, Apr. 1995. DOI: 10.1364/AO.34.001678. [Online]. Available: <http://ao.osa.org/abstract.cfm?URI=ao-34-10-1678>.
- [52] *Bruker IFS 125HR User Manual kernel description*, https://spec.jpl.nasa.gov/ftp/pub/outgoing/IFS125HR_manual.pdf, Accessed: 2020-11-18.